HYBRID PHOTONIC CRYSTAL CAVITY BASED LAYERS

Athanasios-Alexandros Liles

A Thesis Submitted for the Degree of PhD
at the
University of St Andrews

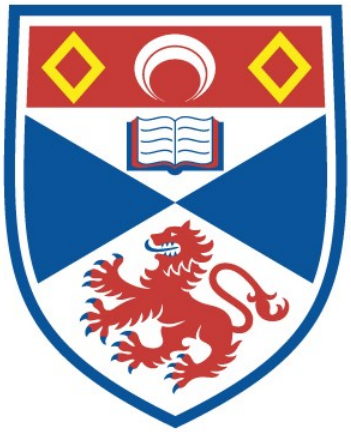

2017

Hybrid Photonic Crystal Cavity Based Lasers

Athanasios – Alexandros Liles

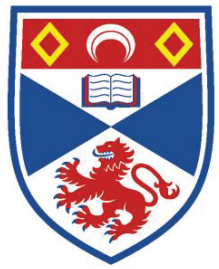

University of
St Andrews

This thesis is submitted in partial fulfilment for the degree of PhD
at the
University of St Andrews

June 2017

Declarations

I, Athanasios – Alexandros Liles, hereby certify that this thesis, which is approximately 40000 words in length, has been written by me, and that it is the record of work carried out by me, or principally by myself in collaboration with others as acknowledged, and that it has not been submitted in any previous application for a higher degree.

I was admitted as a research student in September, 2013 and as a candidate for the degree of Doctor of Philosophy in September, 2013; the higher study for which this is a record was carried out in the University of St Andrews between 2013 and 2017.

Date: ……. Signature of candidate: ……..

I hereby certify that the candidate has fulfilled the conditions of the Resolution and Regulations appropriate for the degree of Doctor of Philosophy in the University of St Andrews and that the candidate is qualified to submit this thesis in application for that degree.

Date: ……. Signature of supervisor: ……..

In submitting this thesis to the University of St Andrews I understand that I am giving permission for it to be made available for use in accordance with the regulations of the University Library for the time being in force, subject to any copyright vested in the work not being affected thereby. I also understand that the title and the abstract will be published, and that a copy of the work may be made and supplied to any bona fide library or research worker, that my thesis will be electronically accessible for personal or research use unless exempt by award of an embargo as requested below, and that the library has the right to migrate my thesis into new electronic forms as required to ensure continued access to the thesis. I have obtained any third-party copyright permissions that may be required in order to allow such access and migration, or have requested the appropriate embargo below.

The following is an agreed request by candidate and supervisor regarding the publication of this thesis:

PRINTED COPY: No embargo on print copy.

ELECTRONIC COPY: No embargo on electronic copy.

ABSTRACT AND TITLE EMBARGOES: I agree to the title and abstract being published.

Date: …….

Signature of candidate: …….. Signature of supervisor: ……..

Acknowledgements

Given the chance, I would like to thank a number of people who were involved in the conduction of my PhD and the completion of this thesis.

To begin with, I would like to express my sincere gratitude to my supervisor, Dr Liam O'Faolain (William Whelan-Curtin), not only for offering me the opportunity to work in his research group and guiding me through this project, but also for always trying to be available for long discussions and willing to share his expertise and inspiring ideas. In addition, I am highly indebted to Dr Kapil Debnath and Dr Alfredo Gonzalez-Fernandez for their technical and scientific assistance and guidance, as well as for their patience and the significant amount of time they spent with me during their presence in St Andrews. Special thanks go to Dr Stephen Hegarty from Cork Institute of Technology (CIT) and Tyndall National Institute for the discussions and suggestions, and to Andrei Bakoz for helping me with the laser measurements and with my staying in Cork.

Moreover, I would like to thank my colleagues and friends in the School of Physics and Astronomy of the University of St Andrews for being most helpful and creating a pleasant working environment. I have to particularly thank everyone in the Nanophotonics and Synthetic Optics groups – especially Dr Andrea DiFalco, Dr G.R. Chinna Devarapu and Changyu Hu – and Dr N. Klaus Metzger. I would like to express my special appreciation to Mr Steve Balfour, Mr Callum Smith, Mr Graeme Beaton, and Mr Chris Watson for keeping the cleanroom and all its equipment in good working order at all times. I would also like to say thanks to Professor Dries Van Thourhout (Ghent University) for his time and effort in reading and improving this thesis.

A big 'thank you' goes to those close to me, and last but not least, I would like to thank my family for so many reasons that would at least double the amount of pages of this thesis if I had to write them down.

List of Publications

Journal Articles

- K. Debnath, R. Moore, **A. Liles**, L. O'Faolain, "Toolkit for Photonic Integrated Circuits Based on Inverted Rib Waveguides", Journal of Lightwave Technology, 33, 19, p. 4145-4150 (2015)
- **A. A. Liles**, K. Debnath, L. O'Faolain, "Lithographic wavelength control of an external cavity laser with a silicon photonic crystal cavity-based resonant reflector", Optics Letters, 41, 5, p. 894-897 (2016)

Conference Proceedings

- **A. Liles**, K. Debnath, L. O'Faolain, "External-Cavity Hybrid Laser with Silicon Photonic Crystal Cavity-based Resonant Reflector", 2015 IEEE 12th International Conference on Group IV Photonics (GFP)
- A. A. Gonzalez-Fernandez, **A. A. Liles**, S. Persheyev, K. Debnath, L. O'Faolain, "Wavelength-controlled external cavity laser with a silicon photonic crystal resonant reflector", Proc. SPIE 9753, Optical Interconnects XVI, 975317 (2016)
- A. P. Bakoz, **A. A. Liles**, E. A. Viktorov, L. O'Faolain, T. Habruseva, G. Huyet, S. P. Hegarty, "Lasing dynamics of photonic crystal reflector laser", Proc. SPIE 9892, Semiconductor Lasers and Laser Dynamics VII, 989204 (2016)
- A. P. Bakoz, **A. A. Liles**, E. A. Viktorov, L. O'Faolain, G. Huyet, S. P. Hegarty, "Photonic crystal reflector laser", 2016 International Conference Laser Optics (LO)
- **A. A. Liles**, A. P. Bakoz, A. A. Gonzalez-Fernandez, T. Habruseva, S. Persheyev, G. Huyet, S. P. Hegarty, L. O'Faolain, "Hybrid Photonic Crystal Lasers", 2016 18th International Conference on Transparent Optical Networks
- **A. A. Liles**, A. A. Gonzalez-Fernandez, L. O'Faolain, "III-V/Silicon External Cavity Laser with Photonic Crystal Cavity Reflector", 12th International Symposium on Photonic and Electromagnetic Crystal Structures PECS XII (2016)
- **A.A. Liles**, A. P. Bakoz, A. A. Gonzalez-Fernandez, T. Habruseva, G. Huyet, S. P. Hegarty, L. O'Faolain, "Compact III-V/Silicon External Cavity Laser Configuration with Photonic Crystal Cavity Reflector for Direct Frequency Modulation", 2016 IEEE 13th International Conference on Group IV Photonics (GFP)

Conferences Attended

- UK Silicon Photonics Conference (Showcase), November 2013, Southampton
- IEEE 12th International Conference on Group IV Photonics (GFP), August 2015, Vancouver
- 12th International Symposium on Photonic and Electromagnetic Crystal Structures (PECS XII), July 2016, York
- IEEE 13th International Conference on Group IV Photonics (GFP), August 2016, Shanghai

Abstract

In recent years, Silicon Photonics has emerged as a promising technology for cost-effective fabrication of photonic components and integrated circuits, the application of which is recently expanding in technological fields beyond tele- and data-communications, such as sensing and biophotonics. Compact, energy-efficient laser sources with precise wavelength control are crucial for the aforementioned applications. However, practical, efficient, electrically-pumped lasers on Silicon or other group IV elements are still absent, owing to the indirect bandgap of those materials. Consequently, the integration of III-V compounds on Silicon currently appears to be the most viable route to the realization of such lasers.

In this thesis, I present and explore the potential of an External Cavity (EC) hybrid III-V/Silicon laser design, comprising a III-V-based Reflective Semiconductor Optical Amplifier (RSOA) and a Silicon reflector chip, based on a two-dimensional Photonic Crystal (PhC) cavity vertically coupled to a low-refractive-index dielectric waveguide. The vertically coupled system functions as a wavelength-selective reflector, determining the lasing wavelength. Based on this architecture mW-level continuous-wave (CW) lasing at room temperature was shown both in a fiber-based long cavity scheme and die-based short cavity scheme, with SMSR of > 25 dB and > 40 dB, respectively.

Furthermore, by electrically modulating the refractive index of the PhC cavity in the reflector chip, tuning of the emitted wavelength was achieved in the die-based short cavity EC laser configuration. In this way, I demonstrated the suitability of the examined EC configuration for direct frequency modulation. The proposed scheme eliminates the need for wavelength matching between the laser source and a resonant modulator, and reveals the potential of employing low-power-consumption resonant modulation in practical Silicon Photonics applications.

Contents

Chapter 1

Light Sources for Optical Interconnects

1.1 Introduction

Access to Information and Communications Technology (ICT) platforms by anyone, anywhere and at any time is becoming of increasingly high importance [1]. This demand reveals a distinct characteristic of our society: its reliance on a perpetual transfer of knowledge and information. An inevitable consequence of this fact, in combination with the advancement of technology, has been the expansion of the Internet and its infrastructure (with more than 3.5 billion estimated Internet users in March 2017 [2]), and the development of distributed computing applications. This inexorable 'hunger' for bandwidth (visualized in **Fig. 1.1**) has recently been reflected upon the establishment of a new generation of network services, known as cloud services. Cloud services are made available to users through cloud computing servers, and therefore are based on the concentration of data storage and computational power in data centers. Data centers are huge facilities housing interconnected computer systems and associated components, which are in turn responsible for the distribution of data to the end-users. In such architectures, fast processing speeds and low latency are crucial: according to Google, for example, an additional latency of 0.5 sec when loading a search result page causes a 20% decrease in search traffic [3]. Given the enormous amounts of data that need to be handled, the above restrictions impose significant challenges on the ICT and data communication infrastructure, especially in terms of power consumption. With current estimates showing that the operation of the Internet amounts to ~5% of the global electricity use [4] (and suggestions that the production and use of ICT might

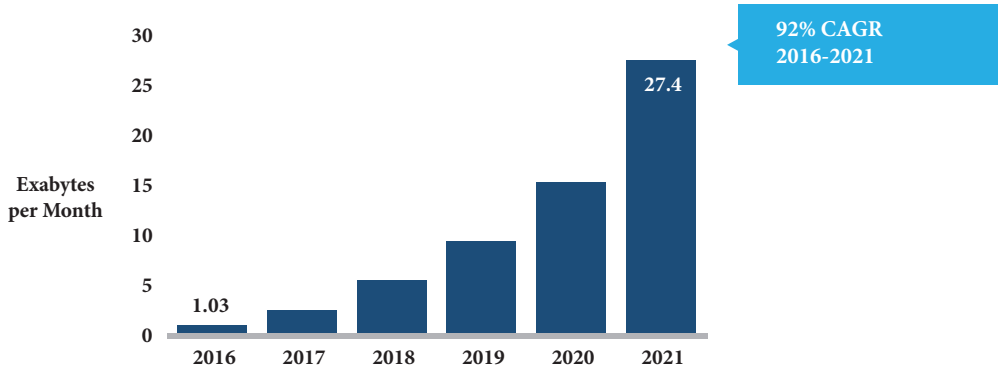

Figure 1.1 Projected IPv6 Mobile Data Traffic Forecast by CISCO (column chart with data from Cisco Visual Networking Index: Global Mobile Data Traffic Forecast Update, 2016-2012 White Paper [5]).

grow to ~20% of the global supply by 2030 [6]) the necessity for faster and more energy efficient computer and communication systems is apparent.

To date, improvement in the performance of Integrated Circuits (ICs) and microprocessors has been achieved by scaling down the size of the transistors that comprise them, following the trend predicted by G. Moore in 1965 that the on-chip transistor density would double approximately every two years [7]. However, as the number of transistors per unit area of circuit board increases, so does the complexity and packaging density of the interconnect systems (i.e. the network of metal wires that transport data and synchronization information on and to the chip). A typical microprocessor chip today contains over 10 km of metal tracks in a three-dimensional interconnect network spread over multiple separate layers [3]. The bandwidth of an electrical wire is proportional to its cross-section and inversely proportional to the square of its length [8]. As more and more transistors are packed into a given area on a chip, the interconnections become progressively longer and more complicated, a situation that leads to the appearance of several problems, such as increased parasitic capacitance (and consequently power consumption [9]), higher cross-talk noise [10], and eventually higher signal propagation delay. The intra-/inter-chip communication delay, known as the 'Interconnect Bottleneck' [10], has become considerably high (comparable to the computation delay), leading electrical interconnects to hit a wall in terms of high-speed, energy efficient performance. The enforced shift towards multicore chips and parallel operation, aiming to maintain the processor power dissipation below a certain ceiling/threshold, further aggravates the problem, as it increases the required link length and imposes additional restraints on the supported bitrate/available bandwidth [11]. Numerous approaches have been suggested to overcome the delay, power and bandwidth limitations of traditional electrical interconnects, mostly related to the alteration of the physical means of the links (e.g. superconducting wires, graphene nanoribbons, optical waveguides etc [12]). The project described in this thesis explores the alternative solution of optical interconnects.

With the initial demonstrations of optical transmission taking place in the early '70s and the first fiber-optics-based system for live telephone traffic established in 1977 in Chicago [13], optical communications nowadays dominate the backbone and backhaul networks of the telecommunication systems. However, the employment of optics as an alternative physical approach for short-range networks (datacommunication and interconnects) was not proposed until 1984, when J. W. Goodman [14], [15] suggested using photons instead of electrons as carriers of information in order to hammer away most – if not all – the issues encountered by electrical interconnects [16]. More specifically, as photons are electrically neutral and massless particles, they can propagate in transparent media (i.e. with no electrical resistance or capacitance – the RC time constant and ohmic losses are not an issue) with low heat and power dissipation, and little cross-talk [10]. Furthermore, the high frequencies of optical carrier waves (10^{14} Hz) enable the transmission of multiple optical signals over the same channel by assigning a different wavelength to each signal, a technology known as Wavelength Division Multiplexing (WDM), which is not possible in electronic systems. As a result, the total information capacity of each optical channel increases beyond the modulation bandwidth of each constituent signal, rendering the Nyquist limit (rather than the RC constant) the bandwidth limit for optical interconnects.

However, substituting electrical interconnects with optical equivalents is an endeavour that involves formidable cost and practical challenges. In this scenario, the factors that need to be primarily considered are the fabrication and packaging cost, the ease of integration with the existing infrastructure and the power consumption of the optical interconnects [11], [17]. Silicon Photonics has emerged as an appealing solution, aiming to tackle the aforementioned challenges by providing a common platform for both electronics and optics [18]. As Silicon is the basic material used by the electronics industry, the use of Silicon for optical interconnects offers the potential for integration with the existing electronic circuitry. Additionally, Silicon Photonics can take advantage of the mature CMOS process technology of materials with well-known properties, to deliver low-cost, high-performance optical components and Photonic Integrated Circuits (PIC's) at high volumes.

The Silicon Photonics research was initiated in the mid-'80s, with the works of Soref, Bennett and Lorenzo [19], [20]. Ever since, many keystone interconnect components that can be employed in real-life applications have been demonstrated on Silicon: extremely low-loss waveguides [21], [22], (de)multiplexers [23], ultra-fast modulators [24] and high-bandwidth photodetectors [25]. One of the major research axes of the field has always been the achievement of as low power consumption as possible, in order to comply with the projected performance requirements (indicatively, the International Technology Roadmap for Semiconductors forecasts the need for an individual device energy consumption of > 20 fJ/bit for intra-chip communication and >10 fJ/bit for on-chip interconnects, by 2022 [12]). As the nodes with the highest power consumption in an optical interconnect are the light source and the modulator [26], serious effort has been put in the implementation of compact, energy-efficient active optical devices on Silicon. A significant boost towards that direction was the demonstration of optical components based on micro-photonic resonators, such as ring resonators or photonic crystal cavities. Owing to their ability to strongly confine light spatially and temporally, optical resonators not only offer reduced footprint that makes them appropriate for chip-scale integration, but also exhibit ultra-low switching energies, proving excellent candidates for low-power consumption (sub-pJ/bit) modulation [27], [28], [29], [30]. Even though matching the emitted wavelength of a laser source to the resonances of an optical modulator of this type requires additional complexity and control electronics that have so far hindered their wide deployment in practical applications, their wavelength-selective and energy-efficient nature renders them particularly suitable for WDM systems, and therefore key to satisfying the requirements of future interconnect systems [31].

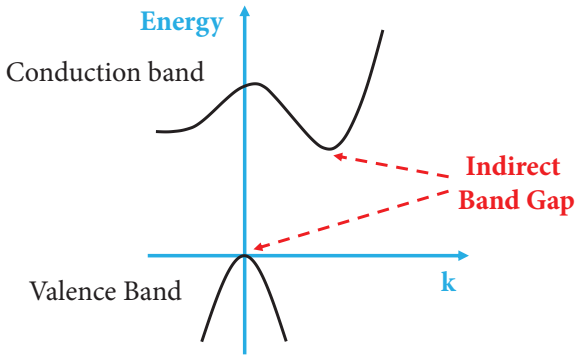

Figure 1.2 Schematic representation of Silicon's indirect band gap (simplified).

However, despite the fact that the Silicon Photonics technology is constantly refined to meet the evolving application requirements, there still exist fundamental constraints that impede its progress in optical interconnect systems. A most prominent example is the inferior light emission – spontaneous or stimulated – from Silicon, stemming from the indirect band gap of Group IV semiconductors (**Fig. 1.2**). As a result, the most essential building block of an optical communication system is still absent from the Silicon Photonics toolkit.

Driven by the above goals, in this thesis, I demonstrate an External Cavity (EC) hybrid III-V/Silicon laser design, utilizing a Photonic Crystal cavity-based resonant reflector, with performance characteristics that align with the requirements of datacommunication networks.

1.2 Laser Sources for Optical Interconnects: The State of the Art

Based on the discussion of Section 1.1, it is apparent that there are three Figures of Merit (FoM) that drive the development of optical transceivers for intra-datacenter transmission links and high performance computational systems [26]:

- Gbps/mm^3 and Gbps/mm^2 (expressing the bandwidth per unit volume and surface of optical circuitry)
- J/bit (quantifying the energy consumption of the links)
- $/Gbps (expressing the transceiver cost per Gbps of transmitted information).

The power consumption (and consequently the cost) in the above scenarios is roughly proportional to the frequency/speed of modulation of an optical carrier. As a result, optical systems that support multiple wavelengths are preferable from an energy point of view. WDM allows sending multiple optical frequencies over the same medium, offering the scalability (in the number of communication channels per physical connection) and the inherent parallelism needed for chip-scale and on-chip interconnections.

The nature of wavelength multiplexing systems [16], [32] along with the operating environment and cost structure of datacentres [26], impose rather strict requirements that the optical source candidates for Silicon optical interconnects should satisfy [33]: emission at around 1.3 or 1.55 μm for direct connectivity with fiber optical networks, electrically pumped lasing for high integration density, high wall-plug efficiency and low energy cost for data transmission, and integratability on Silicon with CMOS-compatible fabrication processes for low-cost, large-scale manufacturing. Additionally, the light sources for Silicon WDM datacommunication networks should exhibit narrow linewidths and precise wavelength registration/stability over a wide temperature range to facilitate tighter channel spacing (and consequently larger aggregate bandwidth at a given frequency band).

Given the above described situation, it is apparent that an electrically pumped laser monolithically fabricated directly on Silicon or any other Group IV element would greatly simplify and accelerate the employment of Silicon Photonics in practical interconnect systems. However, as previously explained, the indirect band gap of Group IV semiconductors

significantly limits their emission efficiency, considerably impeding the development of an on-chip light source on them. Aiming at improving the radiative properties of those materials, a few promising options have been extensively researched in the recent past. More specifically, solutions based on ultra-thin Silicon p-n junctions [34], porous Silicon [35], and extremely pure bulk Silicon [36] have been proposed to achieve electroluminescence from Silicon. Other solutions involve the engineering of the band structure of Silicon [10], strain induced by implantation [37], Raman scattering [38] or rely on quantum confinement effects in Silicon nanocrystals [39], while an alternative solution involves the Erbium (Er) doping of Group IV material systems for optical gain and luminescence [40], [41], [42]. Finally, an approach that has drawn significant attention is the use of strained Germanium (Ge) [43] or Ge alloys (e.g. GeSn) on Silicon for lasing [44], [45]. Be that as it may, all the devices based on the aforementioned solutions are at a preliminary stage and their performance is still far from the standards set by the Silicon Photonics industry. As a result, their employment in real-life interconnect applications in the immediate future appears to be a rather ambitious concept/outlook.

With the demand for higher bandwidth in optical interconnects being ever-growing, the need for an energy-efficient, electrically pumped laser solution that would be integratable with Silicon Photonics PICs appears imperative. III-V compound semiconductors have been traditionally used for highly efficient, electrically injected lasers, owing to their direct bandgap and high material gain. Integrating the III-V functionality on the Silicon Photonics platform therefore, currently appears to be the most viable and practical route to high-efficiency sources for chip-scale applications [33], [46]. This task, however, is particularly challenging due to the significant lattice constant and thermal expansion coefficient mismatch between Silicon and III-V semiconductors. This mismatch is responsible for a high defect density (e.g. threading or misfit dislocation on the interface) and consequently high power losses, hindering in this way the direct growth of III-V materials on Silicon.

In order to tackle this problem, one of the early suggested solutions was the use of III-V-based Vertical Cavity Surface Emitting Lasers (VCSELs) as light sources. VCSELs attracted considerable attention as they exhibit low threshold currents and high output powers (in the order of multiple milliwatts) [47], while their structure allows high coupling efficiency with optical fibers [26]. This is manifested by the fact that most modern transmitters (even commercially available transceivers [48], [49]) for board-to-board links utilize VCSELs. However, VCSELs typically emit at multiple transverse modes [47], and thus can only be employed in Multi-Mode Fiber (MMF) or waveguide systems that do not support WDM. As optical interconnects penetrate the lower layers of datacenters (i.e. on- and intra-chip connections), the projected bandwidth and power consumption requirements dictate the use of WDM. With the current VCSEL-based transceivers suffering from limited performance and cost that exceeds the capacity of investors [26], solutions based on single-mode links (fibers/waveguides) and sources are necessary [50], [51]. To address this situation, a number of approaches of III-V integration on Silicon planar optical circuits for single-mode lasing have been proposed, explored and used depending on the targeted application. These integration strategies are presented and briefly discussed in the section below.

1.2.1 Direct Mounting

One of the easiest and most straightforward ways to achieve (single-mode) laser integration with a Silicon chip is by packaging the chip and a pre-fabricated III-V laser in the same module. This method (referred to as direct mounting) is defined by the direct mounting of individual laser diode dies on a Silicon or Silicon-on-Insulator (SOI) wafer by means of solder bumps [52], and is broadly used in components for long-haul systems today (where III-V lasers are packaged together with e.g. $LiNbO_3$ modulators). This approach allows the testing of the devices prior to integration and the independent development and optimization of the two components for optimal performance and high yield. In this way, it is possible to maintain the superior characteristics of the III-V laser chip (e.g. high wall-plug efficiency of ~20% [33]), as well as good thermal dissipation.

The main issue with this option is the requirement for submicron precision alignment for efficient coupling of light from the III-V component to the on-chip waveguide, which is time consuming, increases the assembly cost, and often results in degraded performance due to coupling losses. Moreover, the optical feedback from the interface between the two components (and in general from any coupling point) is detrimental to the performance of the laser, dictating the need for more complicated packaging approaches (e.g. using micro-optics and optical isolators, as suggested by Luxtera and Tyndall [53, 54]). All the above, in combination with the size of the solder bumps, limit the integration density and the scalability of this approach, and thus make it less attractive for low-cost applications.

1.2.2 Wafer Bonding-Based Heterogeneous Integration

An alternative approach, referred to as wafer bonding-based heterogeneous integration, describes the integration of an unpatterned III-V epi-layer on patterned Silicon circuits (wafers or chips) via a number of different bonding techniques. In this scheme, the light generated in the III-V material is typically evanescently coupled into the Silicon circuits. Upon the completion of the bonding process, the III-V epi-layer is lithographically patterned and the composite system is further processed for the fabrication/definition of the integrated laser. Performing the bonding prior to the laser processing offers a significant advantage in terms of bonding accuracy: the misalignment is determined by the lithographic error between the Silicon and III-V patterning, rather than by the III-V die placement accuracy, rendering this approach superior to direct mounting integration.

According to how the III-V layer stack is bonded on Silicon, the bonding can done on a wafer (wafer-to-wafer) or a die (die-to-wafer) scale. Even though wafer-to-wafer bonding would be thought of as a more appropriate approach for mass production, its sensitivity to wafer bowing and the large wafer size mismatch between III-V wafers (typically 2 inches) and Silicon/SOI wafers (typically 6, 8 or 12 inches) make manufacturing at scale rather difficult. On the other hand, with die-to-wafer bonding, dies of expensive III-V materials can be selectively bonded only where needed, leading to the increased flexibility and reduced cost of the integration process. As

a result, die-to-wafer bonding appears to be favourable for the integration of III-V materials on Silicon. Apart from the above classification, the bonding methods can be further divided to direct and indirect bonding, based on whether a buffer/bonding/insertion/intermediate layer is used between the III-V stack and Silicon.

Direct bonding is defined by bringing polished, flat and ultra-clean wafers (or dies) into direct contact for the formation of strong interfacial Van der Waals bonds. Typical examples include molecular bonding using wet chemistry (for hydrophobic or hydrophilic surface treatment) and oxygen plasma-assisted low temperature molecular bonding (hydrophilic surface treatment) [55, 56]. Another interesting example of direct bonding employs fusion bonding at low temperatures (300 °C) to obtain a conductive hetero-interface that allows for vertical carrier injection [57]. However, achieving good bonding quality with this method requires ultraclean conditions and atom-scale smoothness of the surfaces, resulting in a rather complex fabrication process [58], while it typically exhibits a low potential yield and reproducibility.

Indirect bonding employs metal or polymers like divinylsiloxane-benzocyclobutane (DVS-BCB) as adhesive layers and is therefore referred to as metal-assisted and BCB-assisted bonding, respectively. Metal-assisted bonding typically requires low bonding temperatures and relatively relaxed cleanliness conditions. It allows for effective thermal dissipation and potentially a low resistance Ohmic contact at the interface between Silicon and the bonded layers. The main issue with this approach is that the bonding metal can cause strong light absorption and potential metal contamination. In order to overcome these issues, the removal of the bonding metal from the coupling area (**Fig. 1.3a**) [59] and the use of additional conductive adhesive layers (e.g.

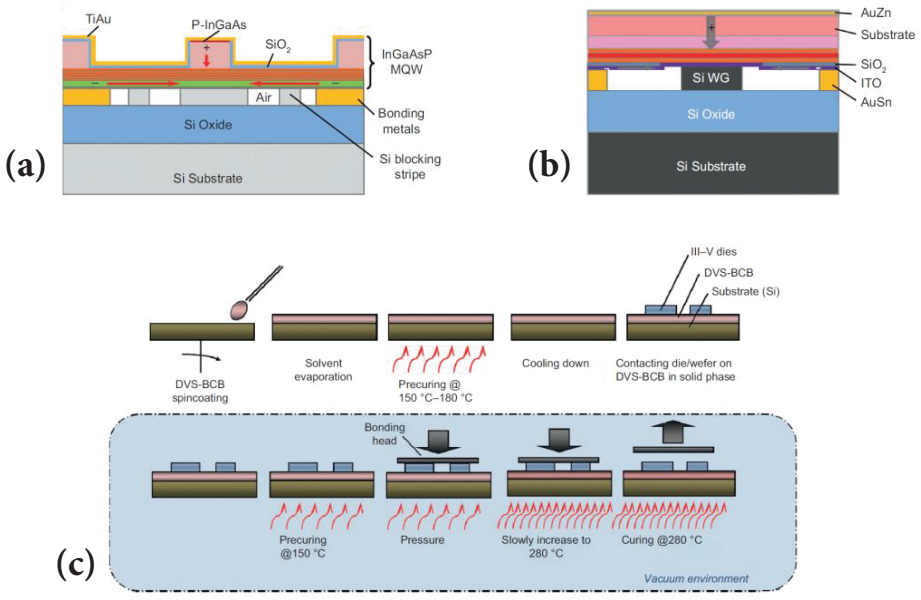

Figure 1.3 (a) Illustration of the cross-section of InGaAsP/Silicon hybrid laser based on metal bonding with excess material removal (image reproduced from [59], © 2011 IEEE). (b) Schematic representation of hybrid InGaAsP/Silicon laser based on metal bonding with ITO conductive adhesive layers (image reproduced from [60], © 2012 IEEE). (c) BCB-assisted bonding process for cold bonding (image reproduced from [61], © 2012 Optical Society of America).

Indium Tin Oxide – ITO, shown in **Fig. 1.3b**) [60] have been proposed. BCB-assisted bonding is defined by the use of a BCB buffer layer between the III-V stack and the Silicon for adhesion purposes. BCB exhibits high bond strength, low refractive index and low curing temperature, and can compensate for the surface roughness between the two materials, relaxing the bonding tolerance compared to molecular bonding [62]. A major issue with this approach is the heat dissipation, as BCB exhibits poor thermal conductivity (much more so than SiO_2) [63, 64] that leads to the self-heating problems and consequently performance degradation of BCB bonded hybrid lasers. Furthermore, apart from affecting the optical confinement in both the III-V and the Silicon waveguides, the thickness of the BCB buffer layer is of critical importance for the coupling between the two parts. Despite the development of techniques for obtaining thin BCB layers with good repeatability (e.g. the process described in [61] and shown in **Fig. 1.3c**), the thickness of the adhesive layer cannot be easily reduced below 50 nm (which even though not ideal, is adequate for reasonably efficient coupling).

In spite of the drawbacks each of the aforementioned approaches might have, wafer-bonding based heterogeneous integration has attracted significant attention for low-cost, high-volume applications due to the high bonding misalignment tolerance that it offers. This fact is reflected upon the large number of laser devices based on this method that have been demonstrated in the past few years and employ various cavity configurations, such as quantum dot (QD) lasers [57], Fabry-Perot lasers [65], distributed feedback (DFB) lasers [59], or lasers with wavelength-selective elements like ring resonators [46], microdisks [63], resonant grating cavities [66], and 1D photonic crystals [67]. Even though the achieved wall-plug efficiencies are lower than those of the prefabricated laser dies used for direct mounting (typically <10%), the laser output in this method is launched directly in the Silicon circuit, compensating in this way in terms of overall power efficiency in the network.

1.2.3 Direct Hetero-Epitaxial Growth

A third approach for fabricating single mode lasers on Silicon is the direct hetero-epitaxial growth of III-V materials on Silicon. Despite of the high fabrication complexity and the fact that the thermal dissipation in a directly grown platform is not optimal, this technique is of notable interest as it could offer the potential for high integration and real wafer scale processing. However, even though the polarity mismatch problem between III-V and Silicon can be solved by e.g. growing III-V materials on an offcut Silicon substrate [68], the large difference in the thermal expansion coefficients of the two (>50% at 20 ^{o}C) [69] can cause threading dislocations and remains a significant issue of this approach. Various methods have been proposed to reduce the threading dislocations obtained with direct hetero-epitaxial growth, including the use of buffer layers (e.g. SiGe or GaSb) between the Silicon and the III-V active layer [33], lateral epitaxial overgrowth (ELOG) techniques [70, 71], and the employment of nano-structures for their improved defect-handling properties (especially QDs [72, 73, 74]). In spite of the substantial efforts, the density of dislocations in the deposited layers is still adequately high to degrade their electro-optical properties and impose a major performance limiting factor for the devices following this approach.

1.2.4 External Cavity Hybrid Integration

A final approach that has attracted considerable attention is the formation of hybrid III-V/Silicon External Cavity (EC) lasers. This method is defined by coupling the output of a Reflective Semiconductor Optical Amplifier (RSOA) die to a waveguide of a Silicon circuit that contains a reflective device (e.g. a Bragg grating). In this way, a laser cavity is formed between the high-reflection (HR) coated facet of the RSOA and the Silicon based reflector. The integration of the RSOA die on the Silicon or SOI wafer is done by means of chip bonding [75], like in the case of direct mounting. This approach allows the independent design, fabrication and optimization of the active and the passive parts, as well as their testing prior to integration, ensuring high yield and performance. Additionally, the spatial separation of the two parts enables good heat dissipation.

Much like for the direct mounting of laser dies, the major problem with this approach is that high precision alignment (typically submicron) is required for efficient coupling between the III-V component and the on-chip waveguide – an issue typically dealt with through the use of spot-size converters (SSC) [75, 76]. The optical feedback from the interface between the RSOA die and the Silicon chip is again important for the performance of the devices, but less so than for directly mounted laser dies, as here this interface is part of the laser cavity and typically anti-reflection (AR) coated. Even though the wall-plug efficiencies achieved with this approach are typically lower than for pre-fabricated lasers (typically ~10-13% [77]), the laser output is launched directly in the waveguide on the Silicon chip, resulting in equivalent amounts of total power guided through the considered network. Finally, the EC approach can offer laser devices with superior performance compared to heterogeneously integrated ones, both in terms of thermal conductivity and in terms of wall-plug efficiency [33]. The reason for the latter is that the optical mode in heterogeneously integrated devices experiences the gain material only evanescently, leading to lower modal gain, while their performance can be further degraded by existence of the bonding layer (through surface roughness, contaminations or losses due to absorption). For the aforementioned reasons, the hybrid EC laser approach currently appears as an appealing/prominent compromise between direct laser mounting and heterogeneous integration. Up to now, hybrid EC devices that use Bragg gratings [75, 78, 79], ring resonators [80, 81], and Sagnac interferometers [82] as Silicon reflectors have been demonstrated based on this technique.

Even though telecommunications and interconnects have until now been the clear drivers for the integration of III-V materials with Silicon in the pursuit of higher bandwidth and low-power operation [11], the demonstration of energy-efficient laser devices through the plethora of integration options presented above has the potential to make an impact on other fields. More specifically, apart from the (data)communication links, fields like sensing, medical diagnostics, compact instrumentation, spectroscopy and biomedical applications, or even high accuracy metrology can benefit from photonic integration technologies [46].

1.3 Aim of the Thesis

This aim of the project described in this thesis is to introduce and explore the potential of an alternative hybrid III-V/Silicon laser design. The examined architecture proposes the formation of an External Cavity (EC) laser that utilizes a III-V RSOA and a Silicon Photonic reflector chip, based on a Photonic Crystal (PhC) cavity vertically coupled to a low-refractive-index bus waveguide [83] (schematic representation given in **Fig. 1.4**). The coupled cavity-waveguide system can act as a reflector at the cavity's resonance, providing therefore wavelength-selective feedback to the laser cavity (resonant feedback). By appropriately designing the waveguide and the PhC cavity, the reflectivity of the coupled system can be controlled and in this way the characteristics of the laser can be defined.

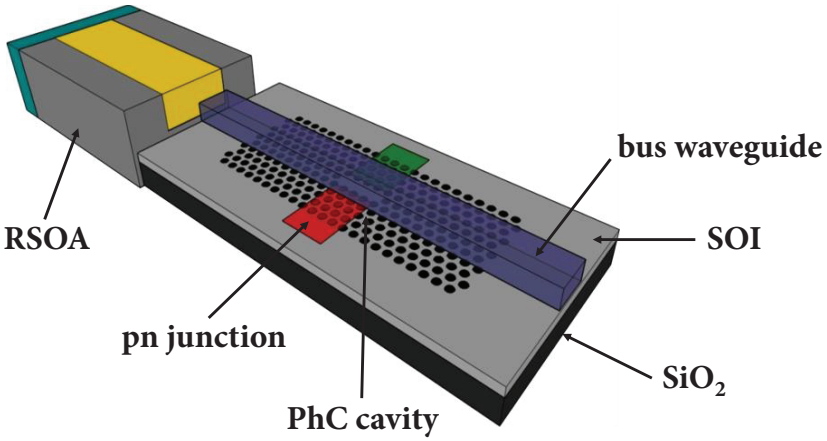

Figure 1.4 Schematic illustration of an External Cavity (EC) laser comprising a III-V RSOA and a Silicon Photonic reflector based on a bus waveguide vertically coupled to a PhC cavity with a pn junction (shown in green and red).

While the hybrid EC configuration was chosen in this project for the reasons and advantages described in Section 1.2.4, Silicon PhC cavities can be equally employable as resonant reflectors in any of the aforementioned integration schemes. The rationale for the choice of a vertically coupled PhC cavity-bus waveguide system as a Silicon-based reflector is manifold. To begin with, the low refractive index of the bus waveguide allows for larger waveguide cross-sections (i.e. larger modal areas), as well as for lower reflectivity at the interface with air, in comparison to the case of Silicon waveguides. As a result, adequately low direct butt-coupling losses can be observed (<3 dB/facet) to both III-V RSOA waveguides and optical fibers, eliminating the need for use of spot-size converters (SSC) or other equivalent structures, and thus simplifying the fabrication process. Furthermore, lower propagation losses can be obtained than for Silicon waveguides, a fact that is of interest given that the laser output is directly launched in the bus waveguide.

The concept of using grating cavity resonant mirrors for III-V/Silicon lasers has been previously introduced in [66]. The use of Photonic Crystal cavities though is particularly relevant, as apart from exhibiting narrow resonance linewidths and highly precise wavelength control, they combine ultra-small size with large Free Spectral Range (FSR), allowing for the higher integration

density and the tighter frequency channel spacing desired in WDM interconnects. Most importantly however, owing to their ultimate *Q*-factor/Volume ratio [84], PhC cavities can exhibit low capacitances (~10^{-18} F) and thus very low switching energies [29, 85]. As the emitted wavelength in the examined laser configuration is determined by the resonant wavelength of the PhC cavity, the modulation of the cavity's resonance by locally modulating its refractive index via free carrier plasma dispersion can result in tuning/direct (frequency) modulation of the lasing wavelength. This method suggests a route to energy-efficient frequency tuning/modulation of the proposed laser device, which interestingly enough simultaneously tackles the wavelength matching problem between the laser and the resonant modulator (since in this case the modulator itself defines the lasing wavelength). Finally, with an outlook at the ultimate goal of integrating hybrid sources with other functional devices on Silicon [33], the demonstration of a hybrid III-V laser solution exploiting the vertical coupling technique can be combined with previous demonstrations of modulators [29] and detectors [86] based on the same concept, to pave the way for the development of a single complete platform towards chip-scale optical interconnects. The study presented in this thesis focuses primarily on low-power-consumption optical WDM datacommunication links. However, an EC laser design with the above described characteristics can be of notable interest for applications in numerous other fields, such as short-range optical links, sensing (e.g. gas sensing, LIDAR) or biomedical instrumentation (e.g. optical coherence tomography (OCT) systems).

1.4 Thesis Content

The content of this thesis is organized in the following way: Chapter 2 presents an overview on the theory of photonic band gap and Photonic Crystal structures. Additionally, it gives a conceptual explanation of the nature and the functionality of the examined EC laser design. Chapter 3 provides a brief description of the different fabrication tools and methods that were used for the realization of this project. Chapter 4 discusses a meter-scale long cavity configuration of the studied hybrid EC design, using a packaged fiber-pigtailed III-V SOA. Chapter 5 demonstrates a compact, μm-scale, short cavity configuration of the studied hybrid EC design, comprising a RSOA die. Further to its functionality, its suitability for integration via chip bonding and its behaviour as a function of temperature are explored. Chapter 6 discusses the potential of the compact EC configuration presented in Chapter 5 for direct frequency modulation and presents some possible future research goals. Finally, Chapter 7 gives an overview of the thesis and concludes by summarizing the most important findings.

References

[1] F. La Rue, "VI. Conclusions and recommendations: Report of the Special Rapporteur on the promotion and protection of the right to freedom of opinion and expression," in *Human Rights Council, Seventeenth Session Agenda Item 3, United Nations General Assembly*, MAY 2011.

[2] "http://www.internetworldstats.com/stats.htm," [Online].

[3] M. Asghari and A. V. Kishnamoorthy, "Silicon Photonics: Energy-efficient communication," *Nature Photonics,* vol. 5, pp. 268-270, MAY 2011.

[4] M. Hazas, J. Morley, O. Bates and A. Friday, "Are there limits to the growth in data traffic?: On time use, data generation and speed," in *Proceedings of the Second Workshop on Computing within Limits (LIMITS '16)*, Irvine, CA, JUN 2016.

[5] "http://www.cisco.com/c/en/us/solutions/collateral/service-provider/visual-networking-index-vni/mobile-white-paper-c11-520862.html," Cisco Systems, Inc.. [Online].

[6] A. S. G. Andrae and T. Edler, "On Global Electricity Usage of Communication Technology: Trends to 2030," *Challenges,* vol. 6, no. 1, pp. 117-157, APR 2015.

[7] G. Moore, "Cramming more components onto integrated circuits," *Electronics,* vol. 38, no. 8, pp. 114-117, APR 1965.

[8] D. A. B. Miller and H. M. Ozaktas, "Limit to the Bit-Rate capacity of electrical interconnects from the aspect ratio of the system architecture," *Journal of Parallel Distributed Computing,* vol. 41, no. 1, pp. 42-52, FEB 1997.

[9] N. Magen, A. Kolodny, U. Weiser and N. Shamir, "Interconnect power dissipation in a microprocessor," in *Proceedings of the 2004 International Workshop on System Level Interconnect Prediction*, Paris, France, FEB 2004.

[10] L. Pavesi and D. J. Lockwood, Silicon Photonics, Berlin, Heidelberg: Springer-Verlag, 2004.

[11] D. A. B. Miller, "Device requirements for optical interconnects to silicon chips," *Proceedings of the IEEE,* vol. 97, no. 7, pp. 1166-1185, JUL 2009.

[12] "International Technology Roadmap for Semiconductors," [Online]. Available: http://www.itrs2.net/.

[13] [Online]. Available: http://www.jeffhecht.com/chron.html.

[14] J. W. Goodman and J. A. Neff, "Optical Interconnections in Microelectronics," in *Optical Computing*, Los Angeles, CA, JAN 1984.

[15] J. W. Goodman, F. I. Leonberger, S.-Y. Kung and A. A. Ravindra, "Optical Interconnections for VLSI Systems," *Proceedings of the IEEE,* vol. 72, no. 7, pp. 850-866, JUL 1984.

[16] D. A. B. Miller, "Rationale and challenges for Optical Interconnects to electronic chips," *Proceedings of the IEEE,* vol. 88, no. 6, pp. 728-749, JUN 2000.

[17] R. G. Beausoleil, P. J. Kuekes, G. S. Snider, S.-Y. Wang and R. S. Williams, "Nanoelectronic and nanophotonic interconnect," *Proceedings of the IEEE,* vol. 96, no. 2, pp. 230-247, JAN 2008.

[18] R. Soref, "The Past, Present, and Future of Silicon Photonics," *IEEE Journal of Selected Topics in Quantum Electronics,* vol. 12, no. 6, pp. 1678-1687, NOV 2006.

[19] R. A. Soref and B. R. Bennett, "Kramers Kronig analysis of electro-optical switching in silicon," in *Proceedings of SPIE, Integrated Optical Circuit Engineering IV, 32*, Cambridge, MA, MAR 1987.

[20] R. A. Soref and J. P. Lorenzo, "Single crystal silicon: a new material for 1.3 and 1.6 μm integrated optical components," *Electronics Letters,* vol. 21, no. 21, pp. 953-954, OCT 1985.

[21] D.-H. Lee, S.-J. Choo, U. Jung, K.-W. Lee, K.-W. Kim and J.-H. Park, "Low-loss silicon waveguides with sidewall roughness reduction using a SiO2 hard mask and fluorine-based dry etching," *Journal of Micromechanics and Microengineering,* vol. 25, no. 1, DEC 2014.

[22] K. Debnath, H. Arimoto, M. K. Husain, A. Prasmusinto, A. Al-Attili, R. Petra, H. M. H. Chong, G. T. Reed and S. Saito, "Low-Loss Silicon Waveguides and Grating Couplers Fabricated Using Anisotropic Wet Etching Technique," *Frontiers in Materials,* vol. 3, FEB 2016.

[23] D. Guo and T. Chu, "Silicon mode (de)multiplexers with parameters optimized using shortcuts to adiabaticity," *Optics Express,* vol. 25, no. 8, pp. 9160-9170, APR 2017.

[24] D. J. Thompson, F. Y. Gardes, J.-M. Fedeli, S. Zlatanovic, Y. Hu, B. P. P. Kuo, E. Myslivets, N. Alic, S. Radic, G. Z. Mashanovich and G. T. Reed, "50 Gb/s silicon optical modulator," *IEEE Photonics Technology Letters,* vol. 24, no. 4, pp. 234-236, FEB 2012.

[25] L. Vivien, J. Osmond, J.-M. Fedeli, D. Marris-Morini, P. Crozat, J.-F. Damlencourt, E. Cassan, Y. Lecunff and S. Laval, "42 GHz p.i.n Germanium photodetector integrated in a silicon-on-insulator waveguide," *Optics Express* , vol. 17, no. 8, pp. 6252-6257, APR 2009.

[26] T. Tekin, N. Pleros, R. Pitwon and A. Hakansson, Optical Interconnects for Data Centers, Woodhead Publishing, NOV 2016.

[27] R. Dubé-Demers, S. LaRochelle and W. Shi, "Ultrafast pulse-amplitude modulation with a femptojoule silicon photonic modulator," *Optica,* vol. 3, no. 6, pp. 622-627, JUN 2016.

[28] E. Timurdogan, C. M. Sorace-Agaskar, J. Sun, E. Shah Hosseini, A. Biberman and M. R. Watts, "An ultralow power athermal silicon modulator," *Nature Communications,* vol. 5, pp. 4008:1-11, JUN 2014.

[29] K. Debnath, L. O'Faolain, F. Y. Gardes, A. Steffan, G. T. Reed and T. F. Krauss, "Cascaded modulator architecture for WDM applications," *Optics Express,* vol. 20, no. 25, pp. 27420-27428, DEC 2012.

[30] Y. Ooka, T. Tetsumoto, A. Fushimi, W. Yoshiki and T. Tanabe, "High speed silicon photonic crystal waveguide," *Scientific Reports,* vol. 5, pp. 11312:1-9, JUN 2015.

[31] C. Sun, M. T. Wade, Y. Lee, J. S. Orcutt, L. Alloatti, M. S. Georgas, A. S. Waterman, J. M. Shainline, R. R. Avizienis, S. Lin, B. R. Moss, R. Kumar, F. Pavanello, A. H. Atabaki, M. Cook, A. J. Ou, J. C. Leu, Y.-H. Chen, K. Asanović, R. J. Ram, M. A. Popović and V. M. Stojanović, "Single-chip microprocessor that communicates directly using light," *Nature,* vol. 528, pp. 534-538, DEC 2015.

[32] H. Liu, C. F. Lam and C. Johnson, "Scaling Optical Interconnects in Datacenter Networks Opportunities and Challenges for WDM," in *2010 IEEE 18th Annual Symposium on High Performance Interconnects (HOTI)*, Mountain View, CA, AUG 2010.

[33] Z. Zhou, B. Yin and J. Michel, "On-chip light sources for silicon photonics," *Light: Science & Applications* , vol. 4, pp. e358:1-13, NOV 2015.

[34] M. J. Chen, J. L. Yen, J. Y. Li, J. F. Chang, S. C. Tsai and C. S. Tsai, "Stimulated emission in a nanostructured silicon pn junction diode using current injection," *Applied Physics Letters,* vol. 84, no. 12, pp. 2163-2165, MAR 2004.

[35] N. Koshida and H. Koyama, "Visible electroluminescence from porous silicon," *Apllied Physics Letters,* vol. 60, no. 3, pp. 347-349, JUL 1991.

[36] M. A. Green, J. Zhao, A. Wang, P. J. Reece and M. Gal, "Efficient silicon light-emitting diodes," *Nature,* vol. 412, pp. 805-808, AUG 2001.

[37] W. L. Ng, M. A. Lourenço, R. M. Gwilliam, S. Ledain, G. Shao and K. P. Homewood, "An efficient room-temperature silicon-based light-emitting diode," *Nature,* vol. 410, pp. 192-194, MAR 2001.

[38] H. Rong, A. Liu, R. Jones, O. Cohen, D. Hak, R. Nicolaescu, A. Fang and M. Paniccia, "An all-silicon Raman laser," *Nature,* vol. 433, p. JAN 2005, 292-294.

[39] L. Pavesi and R. Turan, Silicon Nanocrystals: Fundamentals, Synthesis and Applications, Berlin: Wiley-VCH Verlag GmbH, 2010.

[40] A. Pitanti, D. Navarro-Urrios, R. Guider, N. Daldosso, F. Gourbilleau, L. Khomenkova, R. Rizk and L. Pavesi, "Further improvements in Er3+ coupled to Si nanoclusters rib

waveguides," in *Proc. SPIE 6996, Silicon Photonics and Photonic Integrated Circuits*, Strasbourg,FR, MAY 2008.

[41] S. Yerci, R. Li and L. Dal Negro, "Electroluminescence from Er-doped Si-rich silicon nitride light emitting diodes," *Applied Physics Letters,* vol. 97, pp. 081109:1-4, AUG 2010.

[42] M. Miritello, R. Lo Savio, F. Iacona, G. Franzo, A. Irrera, A. M. Piro, C. Bongiorno and F. Priolo, "Efficient Luminescence and Energy Transfer in Erbium Silicate Thin Films," *Advanced Materials,* vol. 19, pp. 1582-1588, MAY 2007.

[43] J. Liu, X. Sun, D. Pan, X. Wang, L. C. Kimerling, T. L. Koch and J. Michel, "Tensile-strained, n-type Ge as a gain medium for monolithic laser integration on Si," *Optics Express,* vol. 15, no. 18, pp. 11272-11277, AUG 2007.

[44] R. E. Camacho-Aguilera, Y. Cai, N. Patel, J. T. Bessette, M. Romagnoli, L. C. Kimerling and J. Michel, "An electrically pumped germanium laser," *Optics Express,* vol. 20, no. 10, pp. 11316-11320, MAY 2012.

[45] S. Wirths, R. Geiger, N. von den Driesch, G. Mussler, T. Stoica, S. Mantl, Z. Ikonic, M. Luysberg, S. Chiussi, J. M. Hartmann, H. Sigg, J. Faist, D. Buca and D. Grützmacher, "Lasing in direct-bandgap GeSn alloy grown on Si," *Nature Photonics,* vol. 9, pp. 88-92, JAN 2015.

[46] M. J. R. Heck, J. F. Bauters, M. L. Davenport, J. K. Doylend, S. Jain, G. Kurczveil, S. Srinivasan, Y. Tang and J. E. Bowers, "Hybrid Silicon Photonic Integrated Technology," *IEEE Journal of Selected Topics in Quantum Electronics,* vol. 19, no. 4, p. 610017, JUL/AUG 2013.

[47] H. E. Li and K. Iga, Vertical-Cavity Surface-Emitting Laser Devices, Berlin: Springer Berlin Heidelberg, 2003.

[48] D. Vaughan, R. Hannah and M. Fields, "Applications for Embedded Optic Modules in Data Communications," *White Paper, Avago,* FEB 2013.

[49] "Optical Engines 25G BOA (Board-Mount Optical Assembly)," Finisar, [Online]. Available: https://www.finisar.com/optical-engines/fbotd25fl2c00.

[50] A. Ghiasi, "Large data centers interconnect bottlenecks," *Optics Express,* vol. 23, no. 3, pp. 2085-2090, JAN 2015.

[51] J. Cunningham and A. V. Krishnamoorthy, "Overview of short-reach optical interconnects: from VCSELs to silicon nanophotonics," in *Hot Chips: A Symposium on High Performance Chips*, Stanford, CA, AUG 2010.

[52] A. V. Krishnamoorthy, L. M. F. Chirovsky, W. S. Hobson, R. E. Leibenguth, S. P. Hui, G. J. Zydzik, K. W. Goosen, J. D. Wynn, B. J. Tseng, J. Lopata, J. A. Walker, J. E. Cunningham and L. A. D'Asaro, "Vertical-Cavity Surface-Emitting Lasers Flip-Chip Bonded to Gigabit-

per-Second CMOS Circuits," *IEEE Photonics Technology Letters,* vol. 11, no. 1, pp. 128-130, JAN 1999.

[53] M. Mack, M. Peterson, S. Gloenckner, A. Narasinmha, R. Koumans and P. De Dobbelaere, "Method and System for a Light Source Assbembly Supporting Direct Coupling to an Integrated Circuit". US Patent 8,168,939 B2, 1 MAY 2012.

[54] B. Snyder, B. Corbett and P. O'Brien, "Hybrid integration of the wavelength-tunable laser with a silicon photonic integrated circuit," *Journal of Lightwave Technology,* vol. 31, no. 24, pp. 3934-3942, AUG 2013.

[55] H. Park, A. W. Fang, S. Kodama and J. E. Bowers, "Hybrid silicon evanescent laser fabricated with a silicon waveguide and III-V offset quantum wells," *Optics Express,* vol. 23, no. 23, pp. 9460-9464, NOV 2005.

[56] R. H. Esser, K. D. Hobart and F. J. Kub, "Improved Low-Temperature Si-Si Hydrophilic Wafer Bonding," *Journal of the Electrochemical Society,* vol. 150, no. 3, pp. G228-G231, FEB 2003.

[57] K. Tanabe, K. Watanabe and Y. Arakawa, "III-V/Si hybrid photonic devices by direct fusion bonding," *Scientific Reports,* vol. 2, pp. 349:1-6, APR 2012.

[58] G. Roelkens, J. Van Campenhout, J. Brouckaert, D. Van Thourhout, R. Baets, P. Rojo Romeo, P. Regreny, A. Kazmierczak, C. Seassal, X. Letartre, G. Hollinger, J.-M. Fedeli, L. Di Cioccio and C. Lagahe-Blanchard, "III-V/Si photonics by die-to-wafer bonding," *Materials Today,* vol. 10, no. 7-8, pp. 36-43, JUN 2007.

[59] T. Hong, G.-Z. Ran, T. Chen, J.-Q. Pan, W.-X. Chen, Y. Wang, Y.-B. Cheng, S. Liang, L.-J. Zhao, L.-Q. Yin, J.-H. Zhang, W. Wang and G.-G. Qin, "A Selective-Area Metal Bonding InGaAsP-Si Laser," *IEEE Photonics Technology Letters,* vol. 22, no. 15, pp. 1141-1143, AUG 2010.

[60] T. Hong, Y.-P. Li, W.-X. Chen, G.-Z. Ran, G.-G. Qin, H.-L. Zhu, S. Liang, Y. Wang, J.-Q. Pan and W. Wang, "Bonding InGaAsP/ITO/Si Hybrid Laser With ITO as Cathode and Light-Coupling Material," *IEEE Photonics Technology Letters,* vol. 24, no. 8, pp. 712-714, APR 2012.

[61] S. Keyvaninia, M. Muneeb, S. Stanković, P. J. Van Veldhoven, D. Van Thourhout and G. Roelkens, "Ultra-thin DVS-BCB adhesive bonding of III-V wafers, dies and multiple dies to a patterned silicon-on-insulator substrate," *Optical Materials Express,* vol. 3, no. 1, pp. 35-46, DEC 2012.

[62] F. Niklaus, P. Enoksson, E. Kälvesten and G. Stemme, "Low-temperature full wafer adhesive bonding," *Journal of Michromechanics and Microengineering,* vol. 11, no. 2, pp. 100-107, 2001.

[63] J. Van Campenhout, P. Rojo-Romeo, D. Van Thourhout, C. Seassal, P. Regreny, J.-M. Fedeli and R. Baets, "Thermal Characterization of Electrically Injected Thin-Film InGaAsP Microdisk Lasers on Si," *Journal of LIghtwave Technology,* vol. 25, no. 6, pp. 1543-1548, JUN 2007.

[64] G. Roelkens, D. Van Thourhout and R. Baets, "Ultra-thin benzocyclobutene bonding of III–V dies onto SOI substrate," *Electronics Letters,* vol. 41, no. 9, pp. 561-562, APR 2005.

[65] A. W. Fang, H. Park, O. Cohen, R. Jones, M. J. Paniccia and J. E. Bowers, "Electrically pumped hybrid AlGaInAs-silicon evanescent laser," *Optics Express,* vol. 14, no. 20, pp. 9203-9210, SEP 2006.

[66] Y. De Koninck, F. Raineri, A. Bazin, R. Raj, G. Roelkens and R. Baets, "Experimental demonstration of a hybrid III–V-on-silicon microlaser based on resonant grating cavity mirrors," *Optics Letters,* vol. 38, no. 14, pp. 2496-2498, JUL 2013.

[67] G. Crosnier, D. Sanchez, S. Bouchoule, P. Monnier, G. Beaudoin, I. Sagnes, R. Raj and F. Raineri, "Hybrid indium phosphide-on-silicon nanolaser diode," *Nature Photonics,* vol. 11, pp. 297-300, APR 2017.

[68] R. Fischer, D. Neuman, H. Zabel, H. Morkoç, C. Choi and N. Otsuka, "Dislocation reduction in epitaxial GaAs on Si(100)," *Applied Physics Letters,* vol. 48, no. 18, pp. 1223-1225, MAY 1986.

[69] P. W. Sparks and C. A. Swenson, "Thermal Expansions from 2 to 40°K of Ge, Si, and Four III-V Compounds," *Physical Review,* vol. 163, no. 3, pp. 779-790, NOV 1967.

[70] T. A. Landgo, C. W. Leitz, M. T. Currie, E. A. Fitzgerald, A. Lochtefeld and D. A. Antoniadis, "High quality Ge on Si by epitaxial necking," *Applied Physics Letters,* vol. 76, no. 25, pp. 3700-3702, JUN 2000.

[71] Z. Wang, C. Junesand, W. Metaferia, C. Hu, L. Wosinksi and S. Lourdudoss, "III-Vs on Si for photonic applications - A monolithic approach," *Materials Science and Engineering: B,* vol. 117, no. 17, pp. 1551-1557, OCT 2012.

[72] M. Tang, S. Chen, J. Wu, Q. Jian, V. G. Dorogan, M. Benamara, Y. I. Mazur, G. J. Salamo, A. Seeds and H. Liu, "1.3-μm InAs/GaAs quantum-dot lasers monolithically grown on Si substrates using InAlAs/GaAs dislocation filter layers," *Optics Express,* vol. 22, no. 10, pp. 11528-11535, MAY 2014.

[73] S. M. Chen, M. C. Tang, J. Wu, Q. Jiang, V. G. Dorogan, M. Benamara, Y. I. Mazur, G. J. Salamo, A. J. Seeds and H. Liu, "1.3 μm InAs/GaAs quantum-dot laser monolithically grown on Si substrates operating over 100°C," *Electronics Letters,* vol. 50, no. 20, pp. 1467-1468, SEP 2014.

[74] A. Y. Liu, C. Zhang, J. Norman, A. Snyder, D. Lubyshev, J. M. Fastenau, A. W. K. Liu, A. C. Gossard and J. E. Bowers, "High performance continuous wave 1.3 μm quantum dot lasers on silicon," *Applied Physics Letters,* vol. 104, pp. 041104:1-4, JAN 2014.

[75] S. Tanaka, S.-H. Jeong, S. Sekiguchi, T. Kurahashi, Y. Tanaka and K. Morito, "High-output power, single-wavelength silicon hybrid laser using precise flip-chip bonding technology," *Optics Express,* vol. 20, no. 27, pp. 28057-28069, DEC 2012.

[76] Y. Urino, T. Usuki, J. Fujikata, M. Ishizaka, K. Yamada, T. Horikawa, T. Nakamura and Y. Arakawa, "High-density and wide-bandwidth optical interconnects with silicon optical interposers," *Photonics Research,* vol. 2, no. 3, pp. A1-A7, JUN 2014.

[77] J.-H. Lee, J. Bovington, I. Shubin, Y. Luo, J. Yao, S. Lin, J. E. Cunningham, K. Raj, A. V. Krishnamoorthy and X. Zheng, "Demonstration of 12.2% wall plug efficiency in uncooled single mode external-cavity tunable Si/III-V hybrid laser," *Optics Express,* vol. 23, no. 9, pp. 12079-12088, APR 2015.

[78] A. Zilkie, P. Seddighian, B. J. Bijlani, W. Qian, D. C. Lee, S. Fatholoumi, J. Fong, R. Shafiiha, D. Feng, B. J. Luff, X. Zheng, J. E. Cunningham, A. V. Krishnamoorthy and M. Asghari, "Power-Efficient III-V/Silicon external cavity DBR lasers," *Optics Express,* vol. 20, no. 21, pp. 23456-23462, OCT 2012.

[79] T. Creazzo, E. Marchena, S. B. Krasulick, P. K. L. Yu, D. Van Orden, J. Y. Spann, C. C. Bliving, L. He, H. Cai, J. M. Dallesasse, R. J. Stone and M. Amit, "Integrated tunable CMOS laser," *Optics Express,* vol. 21, no. 23, p. 28048, NOV 2013.

[80] T. Chu, N. Fujioka and M. Ishizaka, "Compact, lower-power-consumption wavelength tunable laser fabricated with silicon photonic-wire waveguide micro-ring resonators," *Optics Express,* vol. 17, no. 16, pp. 14063-14068, AUG 2009.

[81] S. Lin, S. S. Djordjevic, J. E. Cunningham, I. Shubin, Y. Luo, J. Yao, G. Li, H. Thacker, J.-H. Lee, K. Raj, X. Zheng and A. V. Krishnamoorthy, "Vertical-coupled high-efficiency tunable III-V-CMOS SOI hybrid external-cavity laser," *Optics Express,* vol. 21, no. 26, pp. 32425-32431, DEC 2013.

[82] Y. Zhang, S. Yang, H. Guan, A. E.-J. Lim, G.-Q. Lo, P. Magill, T. Baehr-Jones and M. Hochberg, "Sagnac loop mirror and micro-ring based laser cavity for silicon-on-insulator," *Optics Express,* vol. 22, no. 15, pp. 17872-17879, JUL 2014.

[83] K. Debnath, K. Welna, M. Ferrera, K. Deasy, D. G. Lidzey and L. O'Faolain, "Highly efficient optical filter based on vertically coupled photonic crystal cavity and bus waveguide," *Optics Letters,* vol. 38, no. 2, pp. 154-156, 2013.

[84] M. Notomi, K. Nozaki, A. Shinya, M. Shinji and K. Eiichi, "Toward fJ/bit optical communication in a chip," *Optics Communications,* vol. 314, pp. 3-17, MAR 2014.

[85] T. Tanabe, K. Nishiguchi, E. Kuramochi and M. Notomi, "Low power and fast electro-optic silicon modulator with lateral pin embedded photonic crystal nanocavity," *Optics Express,* vol. 17, no. 25, pp. 22505-22513, DEC 2009.

[86] K. Debnath, F. Y. Gardes, A. P. Knights, G. T. Reed, T. F. Krauss and L. O'Faolain, "Dielectric waveguide vertically coupled to all-silicon photodiodes operating at telecommunication wavelengths," *Applied Physics Letters,* vol. 102, p. 171106, APR 2013.

Chapter 2

Background

2.1 Introduction

With Silicon Wavelength Division Multiplexing (WDM) systems recognized as a prominent solution for next generation intra- and inter-chip optical interconnects, increasing attention is being paid to studying the architecture and design considerations for on-chip WDM transceivers. As high integration density, low energy consumption and low cost are key features of such systems and scale with device size, the miniaturization of optical components has attracted considerable scientific interest. As a result, growing interest can be observed in resonant devices (e.g. optical filters [1, 2] , modulators [3, 4, 5] , detectors [6, 7] , routers [8]), for which the size reduction is achieved by increasing the light matter interaction through resonances.

One of the main energy consuming blocks on a WDM transmitter is the laser source. From the large variety of laser solutions for WDM applications, significant attention has been attracted by External Cavity (EC) lasers, formed by using a Reflective Semiconductor Optical Amplifier (RSOA) and an external Si-based reflector (on the Si WDM transmitter). Up to now, devices that use Bragg gratings [9, 10, 11] , ring resonators [12, 13] , and Sagnac interferometers [14] as Si reflectors have been demonstrated in this platform. This chapter introduces an External Cavity (EC) laser design that employs a low refractive index waveguide vertically coupled to a Silicon Photonic Crystal (PhC) cavity as an external reflector. In this chapter, I will initially give an overview on some fundamental concepts regarding Photonic Crystals and Photonic Crystals cavities. I will then introduce the vertically coupled waveguide-PhC cavity system and explain how it can be used as a resonant reflector. Finally, I will briefly present the fundamentals of external cavity lasers, and describe the formation and rate equations of the EC laser configuration comprising the aforementioned PhC cavity-based reflector.

2.2 Photonic Crystals

Photonic Crystals (PhC) are artificial periodic structures of dielectric materials that have on photons effects akin to the ones that the periodic energy potential of crystalline semiconductor materials has on electrons (i.e. the formation of allowed and forbidden energy bands). Although the propagation of light in periodic multilayer structures has long been a topic of scientific study [15], the field of photonic crystals was not founded until 1987, when E. Yablonovitch [16]

and J. Sajeev [17] used solid-state physics vocabulary to suggest the inhibition of photon propagation in periodic dielectric lattices, establishing the existence in 'photonic crystals' of a 'photonic band gap' [18] analogous to the electronic band gap in semiconductors. Based on the number of dimensions that the periodicity of the dielectric constant extents to – 2D or 3D – the photonic band gap can be in plane [19] or in volume [20]. Photonic band gaps arise from the fact that the wave-vectors for particular wavelengths can be complex in a photonic crystal, inhibiting the propagation of light at those wavelengths in the PhC lattice.

2.2.1 Photonic Band gap in a 1D Photonic Crystal

The origin of the photonic band gap can be qualitatively understood by considering the simple case of a medium with one-dimensional periodicity. A 1D periodic medium can be thought of as a homogenous in the *xy* plane multilayer film, in which the dielectric function varies in the *z*-axis according to $\varepsilon(z) = \varepsilon(z+\kappa\alpha)$ – with α the period and κ =…,*-1, 0, 1, 2,...* an integer – as shown in **Fig. 2.1a**. For this analysis[1] we shall consider an electromagnetic (EM) wave that propagates in the direction of the periodicity of the medium (i.e. in the *z*-axis). In this case, the only non-zero wave vector component is $\vec{k}_z$, which will be abbreviated as $\vec{k}$ for simplicity.

As in every periodic medium, the modes in a multilayer film can be described according to the Bloch theorem [22] in the form of Bloch waves

$$E_k(z) = e^{-ikz}u_k(z). \tag{2.1}$$

$u_k(z)$ is a periodic (envelope) function with the same periodicity as the considered periodic medium, which can be written in Fourier series as

$$u_k(z) = \sum_{n=-\infty}^{+\infty} E_n e^{inGz}. \tag{2.2}$$

In our case, $u\,(z) = u\,(z + \kappa\alpha)$ with κ an integer as above, which suggests that the lattice vector is $G = 2\pi/\alpha$. If we then substitute k with $k+2\pi/\alpha$ in Eq. 2.1, the latter becomes

$$E_{k+2\pi/\alpha}(z) = e^{-ikz}\left(e^{-i2\pi z/\alpha}u_{k+2\pi/\alpha}\,(z)\right) \tag{2.3}$$

It is apparent that the term in the parenthesis is periodic, a fact that shows that k is also a periodic function with period $2\pi/\alpha$, for which $k' = k+2m\pi/\alpha$ (m =…,*-1, 0, 1, 2,...* an integer).

For a homogeneous dielectric medium with constant ε, to which an arbitrary artificial periodicity with period α is assigned, the dispersion relation is simply $\omega(k) = ck/\sqrt{\varepsilon}$, as depicted in **Fig. 2.1b**. The assumed periodicity implies that the dispersion relation will repeat itself at $k' = k+2m\pi/\alpha$, as shown by the dashed lines, leading to the crossing of the dispersion curves at $k = \pm m\pi/\alpha$. The aforementioned fact is simply the graphic representation of the existence in the periodic medium of two modes with frequency $\omega = c\pi/\alpha$, that can be expressed as $e^{\pm i\pi z/\alpha}$ or alternatively in the linear combinations $f(z) = cos(\pi z/\alpha)$ and $g(z) = sin(\pi z/\alpha)$ (**Fig. 2.1a**). Due to

[1] The analysis presented here is based on [21] .

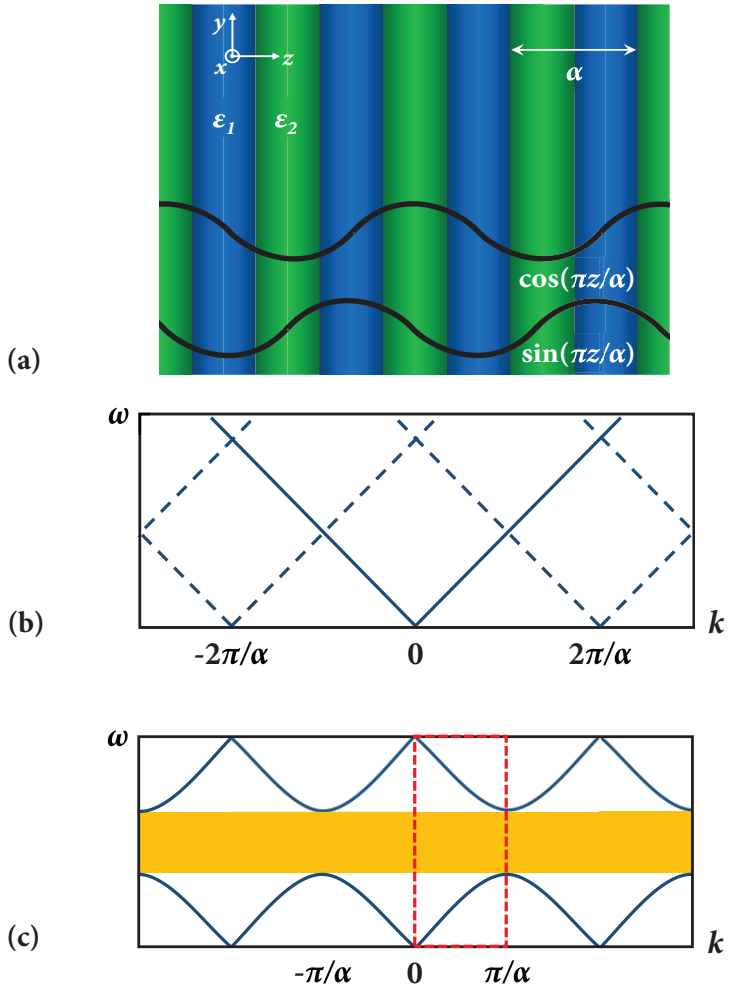

Figure 2.1 (a) Medium with one-dimensional periodicity in the z-direction. The high dielectric constant regions (ε_1) are shown in blue and the low ones (ε_2) are shown in green. The distribution of the two possible modes at $k = \pm\pi/\alpha$ is depicted by the black curves. The mode with lower frequency ω_{low} tends to concentrate its energy in the high ε regions, while the one with higher frequency ω_{high} concentrates its energy in the low ε regions. (b) Dispersion relation (ω-k) for propagation in the z-direction of a homogenous medium (solid lines). The assumed arbitrary periodicity leads to the periodic repetition of the dispersion curves at $k' = k+2m\pi/\alpha$ (dashed lines). (c) Band diagram (dispersion relation) for propagation in the z-direction of a z-periodic medium. A photonic band gap (frequency region marked in yellow) arises due to the appearance of two modes with different frequencies (ω_{high} and ω_{low}) at the same $k = \pm m\pi/\alpha$. The dashed red lines indicate the irreducible Brillouin zone.

the homogeneity of the medium (in terms of dielectric constant ε), the two modes have the exact same frequency (being 'equivalent' in that sense).

In a multilayer medium with periodicity a, in which the dielectric constant is actually perturbed according to $\varepsilon(z) = 1+\Delta\cos(2\pi z/a)$, the two modes described above are not 'equivalent' anymore. More specifically, the same structure can in this case accommodate light of two different frequencies at the same k-vector, which simply means that there are two frequencies – ω_{high} and ω_{low}, with $\omega_{high} > \omega_{low}$ – that correspond to the two modes. However, there are only two

possible ways that the modes can be placed in the medium, due to the translational symmetry that is imposed by the periodicity: as **Fig. 2.1a** shows, the extrema of the modes can be located in either the low-ε or in the high-ε regions. In other words, one of the two types of modes (typically the one with low frequency ω_{low}) tends to concentrate its energy in the high index material, while the other (with frequency ω_{lhigh}) concentrates its energy in the low index material. As a result, there is a finite frequency range for which there is no allowed energy distribution (i.e. k_z has a non-zero imaginary part – there are no supported propagating modes) in the multilayer medium (**Fig. 2.1c**). The described behaviour is mathematically related to the solution of Schrödinger's equation in a periodic potential[2], thus the forbidden-frequency zone is known as the photonic band gap[3]. Effectively, 1D periodic media function as reflectors for the frequencies inside the banb gap (and are also known as Bragg reflectors, due to the dependence of their reflective properties to the Bragg effect). The 'width' of the photonic band gap increases with the dielectric constant/refractive index contrast $\Delta\varepsilon$ between the (two) materials of the multilayer medium.

The dispersion relation of photonic crystal structures is commonly referred to as the band diagram or the band structure and is the most important tool for their description. The band structure describes crystals in k-space (which is the spatial Fourier transform of the considered real space crystalline topology), as that makes the classification of the properties of crystals easier. In a band diagram the region $k = \pm\pi/\alpha$ – also known as the first Brillouin zone – can be identified to be replicated periodically with period $k = 2\pi/\alpha$. As k repeats itself outside the Brillouin zone, the higher order replications of the dispersion curve (observed at $k = \pm m\pi/\alpha$) can be thought of as the curve of the first zone being folded back into the zone when it reaches the zone's edge[4]. Additionally, as the curves have mirror symmetry about $k = 0$, the first Brillouin zone can be further reduced to the region $0 < k < \pi/\alpha$, known as the irreducible Brillouin zone (indicated in **Fig. 2.1c**). It is apparent therefore, that for the study of any reciprocal periodic medium it is sufficient to consider only the irreducible Brillouin zone.

2.2.2 Two-Dimensional Photonic Crystals

Further to 1D Photonic Crystals (PhC), another type of periodic structure that can be commonly found in planar integrated photonic circuits are two-dimensional Photonic Crystals lattices. The term 'two-dimensional' denotes that such a medium is periodic along two of its axes (here periodicity in the xy-plane is assumed) and homogeneous along its third axis (here, the z-axis). The response of a 2D photonic crystal to an optical field varies depending on how the field is located with respect to the crystal's periodicity, i.e. the polarization of the field. Fields in a 2D PhC, can be identified as: Transverse Magnetic (TM), for which the electric field is normal to the plane of periodicity, and Transverse Electric (TE), for which the electric field lies on the plane of periodicity.

[2] Which leads to the existence of the band gaps in crystalline semiconductors.
[3] Due to this analogy, such periodic structures are also called photonic crystals.
[4] Typically referred to as 'band folding'.

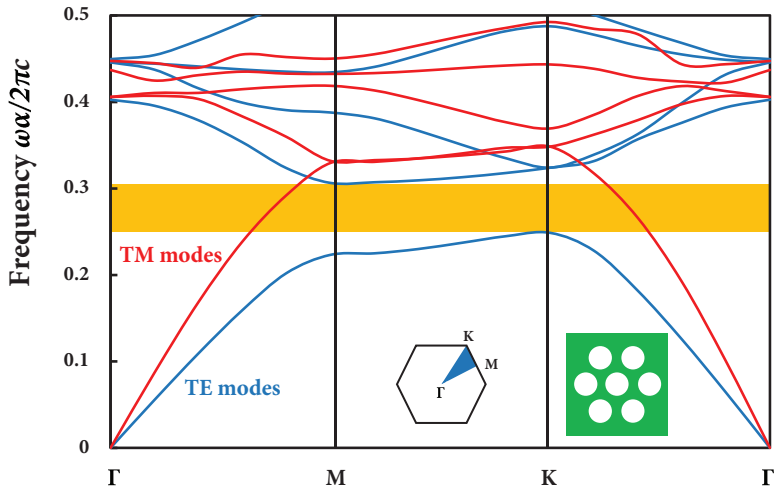

Figure 2.2 Band structure of a two-dimensional triangular lattice of air holes (ε = 1) of radius $r = 0.28\alpha$ on a membrane Silicon slab (ε = 12.11) of thickness $0.5a$. TE modes are shown in blue and TM modes are shown in red. The inset shows the unit cell of the photonic crystal lattice (white corresponds to the air holes and green to Silicon), along with its reciprocal space unit cell (a hexagon rotated by 30° with respect to the photonic crystal unit cell). The band structure was calculated for the wave-vectors within the irreducible Brillouin zone, formed by the central point Γ of the Brillouin zone, and the two high-symmetry points M and K (marked in blue). A photonic band gap exists only for the TE modes and is marked in yellow.

It becomes thus apparent that, as each polarization group 'sees' the periodicity of the lattice differently, the response of the system will be different in each case. In order to better understand that, the band diagram of a triangular lattice for both TE and TM polarizations is shown in **Fig. 2.2**. The structure under consideration is a 2D triangular lattice of air holes of radius $r = 0.28\alpha$, in a Silicon (n = 3.48) membrane slab with thickness 0.5α, with α the period of the lattice. It can be seen that a complete photonic band gap is achieved only for the TE polarization (blue curves) in the frequency range $0.255 < \alpha/\lambda < 0.301$, while there is no band gap for the TM polarization. That is due to the fact that the oscillating optical field in each polarization case experiences the perturbation of the dielectric constant of the medium differently.

As the band diagram describes the crystal in *k*-space, the Brillouin zone is the spatial Fourier transform of the unit cell of the considered lattice. In this case, due to the six-fold symmetry for the triangular lattice, the (hexagonal) Brillouin zone is also six-fold symmetric, with two high-symmetry points that repeat six times. These two points, typically referred to as K and M, together with the centre of the Brillouin zone Γ-point, define the irreducible Brillouin zone (marked with blue in **Fig. 2.2**). Here the band structure has been calculated only for the wave-vectors that lie inside the irreducible Brillouin zone, i.e. in the Γ-K-M-Γ region, as it has been explained that that is sufficient for the study of the band diagram of a photonic crystal.

It can be noticed that the lattice vector *G*, which – as seen in Section 2.2.1 – is given by $G = 2\pi/\alpha$, has a different length in different directions (Γ-K, Γ-M and the directions in between).

For the case of the triangular lattice considered as an example here, $G = 2\pi/\sqrt{3}\alpha$ in the Γ-M direction and $G = 4\pi/3\alpha$ in the Γ-K direction. That simply means that a 2D lattice has different periodicity in different directions. It is therefore important to consider the vectorial nature of k, as the angle of incidence and propagation of light in a 2D photonic crystal affects the periodicity that it experiences. Analogously, a 2D photonic crystal can be thought of as an omnidirectional superposition of 1D photonic crystals (i.e. Bragg reflectors) with a given periodicity. Under that consideration, it is understandable that crystal lattice configurations with as many symmetry axes as possible are desirable for homogeneous omnidirectional reflectivity (i.e. homogenous response for every k). As an indicative example, it can be mentioned that the triangular lattice configuration is considered superior to and is preferred over the square lattice one for two-dimensional photonic crystals, as its hexagonal reciprocal unit cell has a higher rotation symmetry than the square reciprocal unit cell of the square lattice.

2.3 Photonic Crystal Cavities

The understanding of the analogy between photonic crystals and crystalline materials led to the study and observation of many interesting phenomena. One of the most significant observations was the possibility of the existence of localized modes inside the band gap of a photonic crystal lattice [23], [24]: a defect in the lattice structure of a crystalline material can lead to the exhibition of new energy states inside the electronic band gap. Analogously, a perturbation of one or more sites of the lattice of a photonic crystal can result in the appearance of a single localized mode or a set of closely spaced modes with frequency inside the photonic band gap. These modes are spatially 'trapped' in the region where the perturbation lies physically.

The above described system can be conceptually thought of as a resonator: the propagation of light in the rest of the photonic crystal is forbidden as the boundaries of the defect act as Bragg reflectors in the direction of propagation[5]. Therefore, light at the considered (resonant) frequency oscillates inside the defect and only decays exponentially out of it (in the photonic crystal lattice) – it is apparent that the defect acts effectively as an optical cavity. **Fig. 2.3a** shows a photonic crystal cavity formed by removing the central rod of an ideal 2D square lattice of Silicon rods in air. The appearance of a localized mode (represented by the green line) with frequency inside the photonic band gap for the TM polarization[6] can be seen in the band diagram of **Fig. 2.3b**. This is a convenient way of visually depicting the fact that the optical mode is confined in a photonic crystal cavity as a result of the omnidirectional photonic band gap (i.e. Bragg reflection) that it experiences about the perturbed sites.

[5] Since it was assumed that the frequency of the considered mode lies inside the band gap of the photonic crystal.

[6] The structure under consideration exhibits a complete photonic bandgap for the TM polarization as the lattice sites are formed by high-index material on low-index 'background', contrary to the example examined in Section 2.2.2.

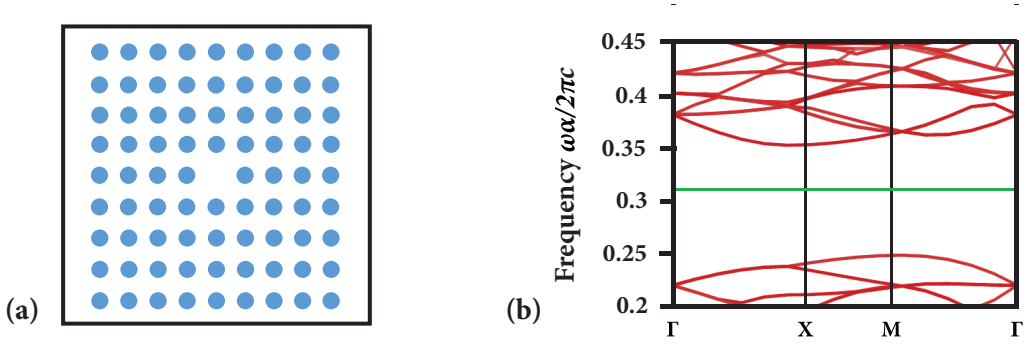

Figure 2.3 (a) Point defect photonic crystal cavity formed by removing the central site of an ideal square lattice of Silicon rods ($\varepsilon = 12.11$) in air ($\varepsilon = 1$). (b) Localized mode (green line) with frequency in the TM photonic band gap due to the perturbation of the photonic crystal lattice.

As for any optical cavity, there are two fundamental features that are necessary for the characterization of photonic crystal cavities: the volume of the mode V and the quality factor. The modal volume describes the spatial extent and the energy density of an optical mode inside a cavity. The quality factor (typically referred to as the Q-factor) is defined as the ratio of the energy stored in the cavity to the energy lost per optical cycle[7] and expresses quantitatively how strongly a mode is confined inside a cavity. Optical cavities with high Q-factor and small modal volume are a typical tool for achieving enhanced light-matter interaction. Owing to the exhibition of the photonic band gap – that is equivalent to very high frequency-dependent reflectivity – photonic crystal cavities can exhibit extremely small mode volumes (on the order of a cubic wavelength) with very high quality factors. For example, by removing a single site of an ideal photonic crystal lattice (corresponding to a band gap-wavelength sized modal volume), a cavity is formed with theoretically infinite quality factor.

For two-dimensional photonic crystal cavities in reality, where the lattice does not extend infinitely out of the plane (of periodicity), vertical confinement is achieved via total internal reflection. For example, in the case of a PhC cavity on a 2D slab (xy-plane) that is suspended in a medium with refractive index n_{sus}, the confinement of the cavity mode is only possible if the vertical component of its wave-vector ($\vec{k}_z$) is imaginary (lossy) out of the slab. According to Snell's law, the vertical confinement condition in the structure can be formulated as

$$k_{confined} > k_{radiating} \Leftrightarrow \sqrt{k_x^2 + k_y^2} > \frac{n_{sus}\omega}{c} \qquad \textbf{(2.4)}$$

Similar to the 'light-line'[8] (**Fig. 2.4a**) that represents schematically the total internal reflection condition for simple waveguides, the schematic representation of the condition of Eq. 2.4 in two

[7] Typically the quality factor of a cavity Q is related to the energy decay rate of the cavity Γ through $Q = \omega_0/2\Gamma$, where ω_0 is the frequency of the cavity mode (i.e. a resonance frequency of the cavity).

[8] The 'ligth-line' is defined as the dispersion relation ($\omega/k = c_0/n_{mat}$) in a material with refractive index n_{mat}. It is a useful tool to distinguish between guided and non-guided modes in dielectric slab waveguides, where the light-lines of the core and the cladding materials can divide the dispersion diagram into a region of discrete guided modes, a region of a non-guided mode continuum, and a forbidden region with no propagating modes.

dimensions can be thought of as a 'light-cone' (defined by $\omega/k = c_0/n_{sus}$), which for a given frequency ω_0 becomes a circle (**Fig. 2.4b** and **c**). Any optical mode 'inside' the light-cone (i.e. $k < n_{sus}\omega/c_0$) will radiate in the surrounding material. As there is a finite number of wave-vectors that can be confined by total internal reflection, energy dissipation out of the cavity due to vertical radiation is unavoidable, even if the cavity modes are perfectly confined in the plane of periodicity (via the photonic band gap). Consequently, in practical 2D photonic crystal cavity cases, the vertical energy decay should be taken into account for the calculation of the total quality factor Q_0 of the cavity, which will be given by

$$\frac{1}{Q_0} = \frac{1}{Q_\parallel} + \frac{1}{Q_\perp} \tag{2.5}$$

with $Q_\parallel$ and $Q_\perp$ being the quality factors related to the in- and out-of-plane energy decay of the cavity, respectively.

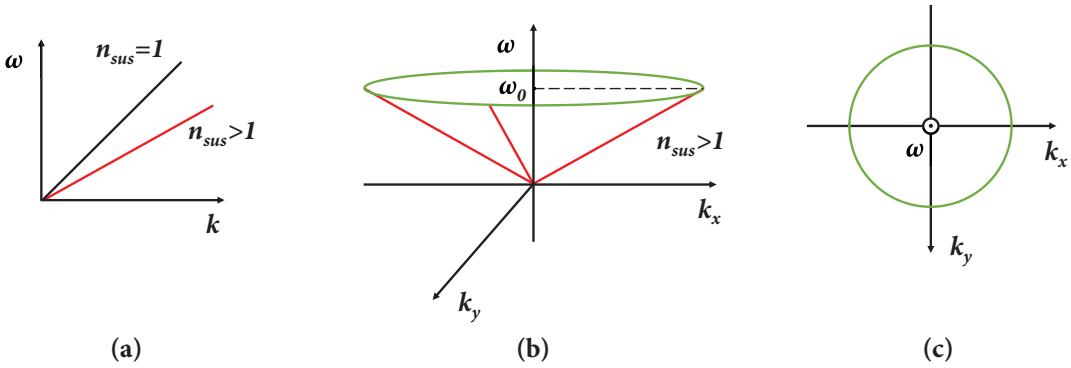

Figure 2.4 (a) Light-line for $n_{sus} = 1$ (black) and $n_{sus} > 1$ (red). (b) and (c) Light-cone for $n_{sus} > 1$ that for a given frequency ω_0 becomes a circle (shown in green).

The high spatial confinement in photonic crystal cavities is equivalent to broad spatial frequency distribution in the Fourier/*k*-space (as a property of the spatial Fourier transform through which the two are related). That means that the PhC cavity modes consist of a large number of plane-wave components. According to the above discussion, this translates to high out-of-plane losses in simple 2D photonic crystal cavities, which in turn lead to a decrease of the *Q*-factor of the system. It is therefore apparent that in order to achieve high quality factors in photonic crystal cavities, a reduction of the number of vertically-decaying plane wave components, while maintaining high in-plane confinement, is desired.

In order to understand how this trade-off can be achieved, the simple case of an ideal (Fabry-Pérot) dielectric cavity suspended in material with index n_{sus} can be considered. In this cavity, light is confined by two perfect mirrors in the *x*-axis and by index guiding in the *y*-axis, as shown in **Fig. 2.5**. To study the strength of the confinement in the *y*-axis, it is adequate to consider the spatial Fourier transform of the electric field in the cavity (i.e. its decomposition into plane-wave components). Following Eq. 2.4, if the $\vec{k}_x$ component of a plane wave lies inside the light-cone (i.e. $< n_{sus}\omega/c_0$), the wave can leak into the surrounding material ('weak' confinement).

In general, the Fourier transform of an infinitely long in real space harmonic oscillation (sinusoidal) is two impulses at $\pm\hat{f}$ (the spatial frequency of the oscillation). If the harmonic oscillation is of finite extent, its Fourier transform is a convolution of the two individual Fourier transforms at $\pm\hat{f}$. Inside a cavity, the electric field distribution can be described as a product of the sinusoidal with frequency equal to the resonant frequency of the cavity, and of an envelope function $G(x)$ that is determined by the structure of the cavity. In the above considered cavity, the envelope function $G(x)$ is a rectangular function (**Fig. 2.5a**) and hence the Fourier transform $F(E)$ of its electric field distribution is the convolution (schematically a superposition) of two cardinal sine (sinc) functions centred at $\pm\, n_{mode}2\pi/\lambda_0$ (as shown in **Fig. 2.5b** – n_{mode} is the refractive index of the mode in the cavity). It can be seen that even though the peak intensity of $F(E)$ in k-space is outside the light-cone (marked in with yellow in **Fig. 2.5**), there still are some components with non-negligible intensity that lie inside the leaky region (**Fig. 2.5b**). That is due to the abrupt change in the envelope function $G(x)$ that occurs at the edges of the cavity.

Based on the above discussion, it is understandable that an envelope function $G(x)$ with a less-abrupt profile at the edges of the cavity can lead to a reduction of the intensity inside the light-cone (i.e. to limit vertical radiation). If e.g. a Gaussian $G(x)$ is assumed for the considered cavity (**Fig. 2.5c**), the spatial Fourier transform $F(E)$ of the electric field distribution in the cavity will be given by the convolution of two Gaussian functions centred at $\pm\, n_{mode}2\pi/\lambda_0$ (**Fig. 2.5d**). It is obvious that this alteration has a drastic effect on the intensity distribution in the light-cone, which suggests an increase of the quality factor of the cavity without changes in its modal volume.

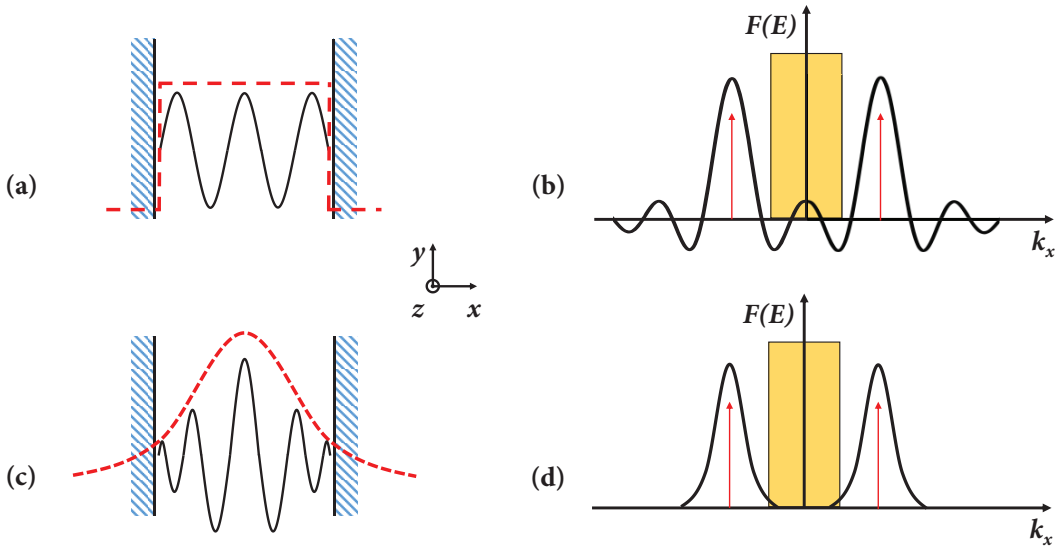

Figure 2.5 (a) Electric field distribution in a cavity with rectangular envelope function $G(x)$ (red dashed line). The refractive index of the cavity mode and of the cladding of the cavity are n_{mode} and n_{sus}, respectively. (b) Spatial Fourier transform of the field shown in (a). $F(E)$ is given by the convolution of the two sinc functions centred at $\pm\, n_{mode}2\pi/\lambda_0$ (marked by the red arrows). (c) Electric field distribution in a cavity with Gaussian envelope function $G(x)$ (red dashed line). The refractive index of the cavity mode and of the cladding of the cavity are the same as in (a). (d) Spatial Fourier transform of the field shown in (c). $F(E)$ is given by the convolution of the two Gaussian functions centred at $\pm\, n_{mode}2\pi/\lambda_0$ (marked by the red arrows). The yellow area in (b) and (d) indicates the light-cone/leaky regime ($-n_{sus}2\pi/\lambda_0 < k_x < n_{sus}2\pi/\lambda_0$).

In real 2D PhC cavities, a more subtle mode profile can be realized by *k*-space engineering, which simply means a modification of the physical distribution of the perturbation of the periodicity (i.e. a change in the position and/or size of the photonic crystal sites – holes or rods – adjacent to or at the boundaries of the cavity). This concept, known as 'gentle confinement', was first proposed by Akahane et al [25], who showed that it is possible to obtain a more Gaussian-like field envelope in an L3 PhC cavity by tuning the first two holes on each side of it. In this way, a decrease in the out-of-plane energy decay was obtained that corresponded to an improvement of the quality factor of the cavity by an order of magnitude in this demonstration. Since then, several 2D photonic crystal cavity designs have been proposed that push towards the same direction. Some prominent examples are the double heterostructure cavity [26], the modulated line defect cavity [27] and the dispersion adapted cavity [28]. The advantage of the latter configuration in comparison to the rest is that it follows more systematic design rules and is thus less prone to fabrication errors, while still maintaining a high Q-factor. However, dispersion adapted cavities have a larger defect size that leads to smaller free spectral range (FSR) and non-single mode response. **Fig. 2.6** shows schematic representations of the different types of high-Q 2D photonic crystal cavities.

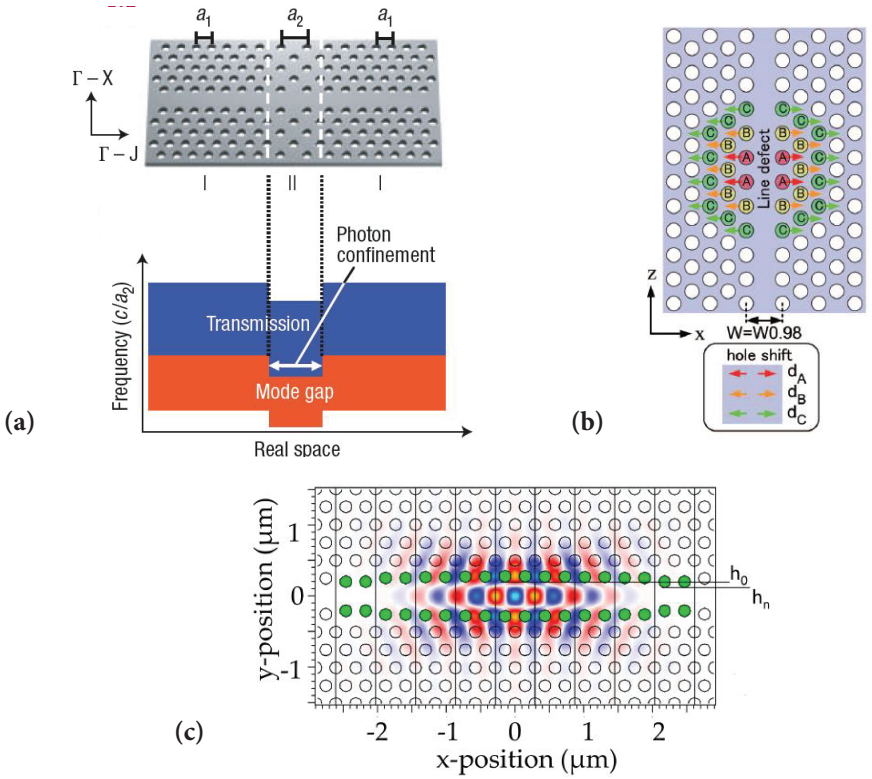

Figure 2.6 (a) Double heterostructure cavity formed by merging the basic PhC structures with different lattice constant I and II, and a schematic of the band diagram along the waveguide direction (reproduced by permission from Macmillan Publishers Ltd: Nature Materials [26], © 2005). (b) Example design of a line defect modulated cavity implemented by shifting holes outwards in a W0.98 line defect waveguide. Shift $d_A = x$, $d_B = 2x/3$ and $d_C = x/3$ (reproduced from [27], with the permission of AIP Publishing, © 2006). (c) Dispersion adapted (DA) cavity with confined first order mode (Ey). The green circles represent the shifted holes. Shift of holes varies from h_0 in the first section to h_n in the last section (5 sections depicted). The waveguide after the last section is a W1 (reproduced from [28], © 2012 IEEE).

2.4 Vertically Coupled Waveguide-Photonic Crystal Cavity as a Resonant Reflector

2.4.1 The Concept

With the situation being as described in Chapter 1, significant scientific and commercial interest has lately been oriented towards Silicon Photonics compatible, compact laser architectures for chip-scale and on-chip datacommunication applications [29, 30]. Particular attention has been attracted by hybrid III-V/Silicon External Cavity (EC) laser configurations [9, 11], by wavelength-tunable lasers [31] and even more so by devices that feature both properties [10, 12], as that allows for independent fabrication and optimization of the gain and the reflective parts, while offering the potential for employment in WDM applications.

The main points that optical interconnects need to address are low cost and low power consumption. Resonant enhancement, therefore, appears to be an attractive way to achieve energy-efficient WDM switching, a fact that is revealed by the increasing interest in resonant modulators [5, 32]. However, the complexity and control electronics required to match the emitted wavelength of a laser source to the resonances of an optical modulator of this nature has so far hindered their deployment in practical datacommunication applications.

Inspired by the devices in [9] and [33], in this work I explore the possibility of using the photonic crystal cavity-based component of [34] as a silicon photonic reflector in external cavity laser architectures. The selected silicon-based component, shown in **Fig. 2.**7, is an optical filter comprising a dielectric bus waveguide vertically coupled to a 2D silicon photonic crystal cavity. The coupled cavity-waveguide system can provide a narrow-band reflection at the resonant frequency of the PhC cavity [1] (the mechanism is described in the section below), thus acting as a wavelength-selective (resonant) mirror. The gain medium of the proposed EC laser schemes is

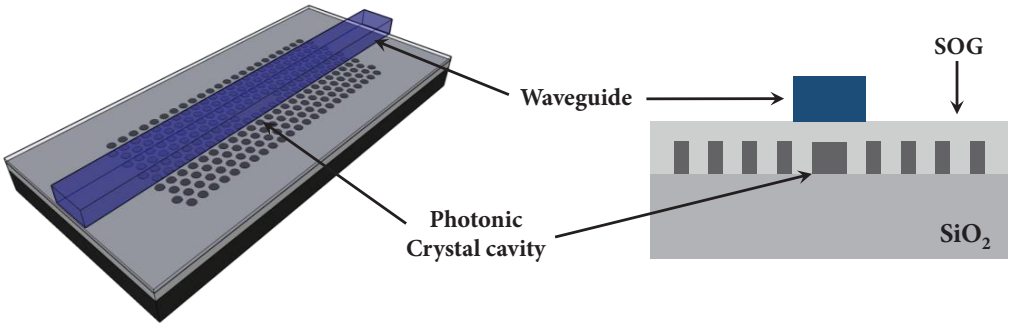

Figure 2.7 Schematic representation and cross-sectional view of the selected resonant reflector. A bus waveguide is vertically coupled to an oxide-clad photonic crystal cavity on SOI. The top cladding layer (spin-on glass – SOG) of the cavity supports the waveguide and acts as a buffer/separating layer between it and the cavity.

a III-V based Semiconductor Optical Amplifier (SOA) with a highly-reflective end that plays the role of the second mirror of the laser cavity.

As optical feedback by resonant reflectors is wavelength-selective, it is apparent that in laser cavities utilizing such mirrors, the emitted wavelength is defined by the resonance of the mirrors. The choice of a silicon photonic crystal cavity-based resonant reflector is therefore particularly technologically relevant, as photonic crystal cavities on Silicon can provide very precisely controlled, narrow-linewidth resonances at very small footprints, features highly desirable in WDM applications. Furthermore, exhibiting the ultimate Q-factor/V ratio [35], photonic crystal cavities can inherently be modulated at a low power-budget, proven by the sub-fJ/bit switching energies previously demonstrated [5]. Thus, the confirmation of the potential of photonic crystal cavities to be employed as external cavity laser mirrors paves the way for the development of an EC laser design with a modulatable reflector, which, combined with a resonant photodetector, can eliminate the aforementioned need for wavelength matching. A physical insight on the reasons leading to the choice of the vertical coupling architecture suggested in [34] is given in the following section.

2.4.2 Oxide Cladding and Vertical Coupling

Following the discussion in Section 2.3, it is easily understandable that high Q-factor silicon photonic crystal cavity designs require an air-clad configuration, as the material index contrast enhances total internal reflection and thus minimizes out-of-plane losses. However, silicon membranes are thermally and mechanically unstable, as well as susceptible to oxidation and contamination. The design presented in [34] suggests the oxide cladding of a photonic crystal cavity by maintaining the SiO_2 layer of the SOI platform and covering the top part of the structure with a layer of spin-on glass (SOG). Even though air-clad cavities are typically easier to design, it has been demonstrated that Q-factors > 10^6, high enough for practical applications, can be obtained by oxide-clad photonic crystal cavities too [36]. The oxide cladding offers improved mechanical and thermal stability compared to silicon membranes [37, 38], and ease of fabrication as no removal of buried oxide (BOx) is required.

The component of [34] also comprises a dielectric waveguide located on top of the photonic crystal cavity (as shown in **Fig. 2.7**). The two parts are separated by the top oxide cladding of the cavity that acts as an accommodating platform for the bus waveguide and as a buffer layer simultaneously. At the resonant frequency of the PhC cavity, light from the waveguide mode couples evanescently through the oxide layer to the cavity mode. As a result, a decrease in the transmission of light propagating in the bus waveguide occurs at (the cavity's) resonance, accounting for the function of the component as a resonant optical filter. The light that is stored in the cavity, couples back to the bus waveguide both to a forward[9] and to a backward propagating mode. The backward propagating component is essentially a narrow-band

[9] The forward propagating light component that is coupled back to the bus waveguide from the cavity has a π phase difference with the light propagating (forward) in the waveguide (as a $\pi/2$ phase-shift is 'picked-up' upon every coupling) and interferes destructively with it.

wavelength-selective reflection (as it is only composed of frequencies that were stored in the PhC cavity), indicating that the vertically coupled waveguide-photonic crystal cavity system of [34] can also be used as a resonant reflector. A conceptual representation of the system's function is given in **Fig. 2.8a**.

The power transmission and reflection coefficients (in the waveguide) of the above described device under weak coupling approximation are given by [34], [39]

$$T = \frac{\Delta\omega^2 + \Gamma_0^2}{\Delta\omega^2 + (\Gamma_0 + \Gamma_C)^2} \tag{2.6}$$

$$R = \frac{\Gamma_C^2}{\Delta\omega^2 + (\Gamma_0 + \Gamma_C)^2} \tag{2.7}$$

where Γ_0 is the intrinsic energy decay rate of the cavity, Γ_C is the total energy decay rate from the photonic crystal cavity to the bus waveguide and $\Delta\omega = \omega - \omega_0$, with ω the frequency of the incident light and ω_0 the (resonant) frequency of the cavity mode. For completeness, it should be mentioned that according to [39], $\Gamma_C/2 = \Gamma_{C-} = \Gamma_{C+}$, with Γ_{C-} and Γ_{C+} expressing the energy decay rates into backward and forward propagating waves/modes of the waveguide, respectively. The power transmission and reflection coefficients at resonance ($\omega = \omega_0 \Leftrightarrow \Delta\omega = 0$) as a function of Q-factors are therefore given by [34]

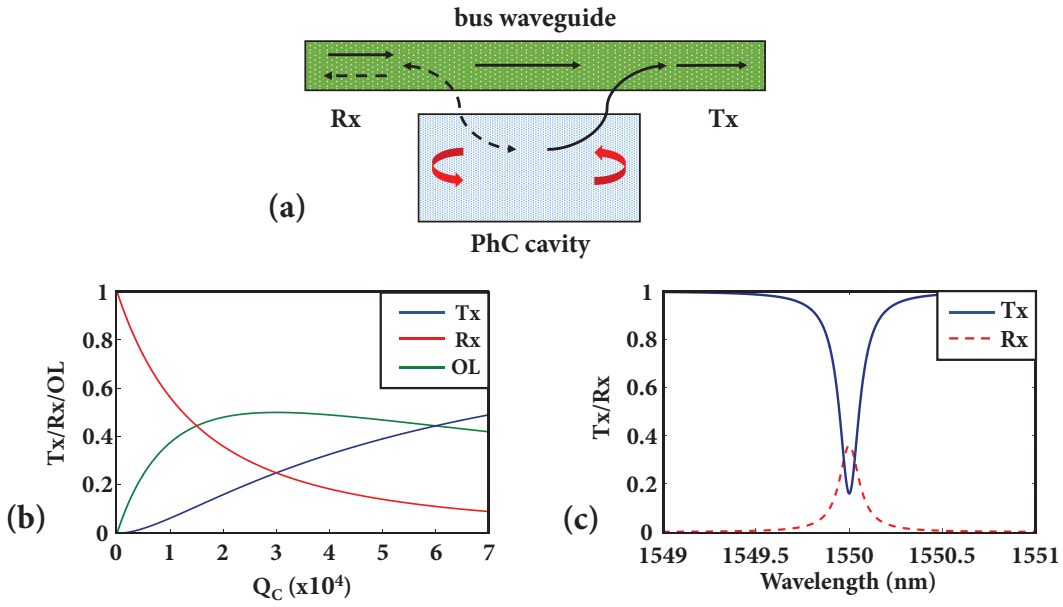

Figure 2.8 (a) Abstract schematic representation of a coupled PhC cavity-bus waveguide system at resonance. The dashed arrows depict the backward propagating (reflected) light component and the solid arrows depict the forward propagating (transmitted) component. (b) Power reflection (red) and transmission (blue) coefficients, and optical losses (green) for vertically coupled waveguide-photonic crystal cavity system at resonance as a function of the coupling rate. The intrinsic quality factor of the cavity was considered to be $Q_0 = 30000$. (c) Reflection Rx (dashed red) and transmission Tx (blue) spectra of a bus waveguide coupled to a PhC cavity with $Q_0 = 30000$ and $Q_C = 20000$.

$$T = \frac{1/Q_0^2}{(1/Q_0+1/Q_C)^2} = \frac{Q_T^2}{Q_0^2} \quad \textbf{(2.8)}$$

$$R = \frac{1/Q_C^2}{(1/Q_0+1/Q_C)^2} = \frac{Q_T^2}{Q_C^2} \quad \textbf{(2.9)}$$

where Q_0 is the intrinsic quality factor of the photonic crystal cavity and Q_C is the quality factor associated with the coupling between the cavity and the waveguide. Q_T expresses the total quality factor of the coupled waveguide-resonator system and is given by

$$\frac{1}{Q_T} = \frac{1}{Q_0} + \frac{1}{Q_C}. \quad \textbf{(2.10)}$$

Eq. 2.9 and 2.10 show the dependence of the reflectivity of such a reflector on only Q_C[10], suggesting that R is only defined by the energy exchange flow between the waveguide and the cavity. This is visually depicted in **Fig. 2.8b** that shows the power reflection (red) and transmission (blue) coefficients in a waveguide vertically coupled to a photonic crystal cavity with (constant) $Q_0 = 30000$, as a function of Q_C (values ranging between 1 and 70000). **Fig. 2.8c** shows the theoretically calculated transmission (Tx) and reflection (Rx) spectra of a coupled PhC cavity-bus waveguide system with resonance at $\lambda = 1550$ nm, $Q_0 = 30000$ and $Q_C = 20000$. The narrow-band reflection can be observed at the resonance frequency of the PhC cavity (the linewidth of the reflection is the same as the linewidth of the resonance of the cavity). It can be seen that $T+R \neq 1$, which indicates that the examined system is not lossless[11]. The optical losses (OL) can be calculated by $OL = 1 - T - R$ and are shown in green in **Fig. 2.8b**.

It is worth noticing that the coupling in the selected vertically coupled photonic crystal cavity-waveguide system is based on the matching and overlap of the k-vector of the waveguide with the rich k-space distribution of the photonic crystal cavity [1, 34]. As a result, efficient coupling between high Q-factor 2D photonic crystal cavity designs and low refractive index ($n < 2.1$) waveguides can be achieved [34], allowing for larger waveguide modal areas and lower –coupling and transmission – losses than those occurring in the high-index waveguides of the in-plane coupling configurations. This last characteristic is particularly relevant for external resonant reflectors as in those cases high coupling efficiencies (both at the output of the laser and at the interface with the gain medium) are greatly desired.

An additional attractive feature of the vertical coupling scheme [1, 34] is that, even though it is simply a topological variation of side coupling, it can eliminate problems associated with the traditional in-plane coupling of light in 2D photonic crystal cavities [40]. More specifically, increasing the proximity of the input waveguide to the 2D photonic crystal cavity (necessary for the increase/change of the coupling efficiency) in an in-plane configuration results in a disturbance of the planar symmetry of the photonic crystal lattice around the cavity, which simply translates to a decrease of the quality factor of the cavity. Furthermore, the physical

[10] The intrinsic quality factor Q_0 is considered constant as an inherent characteristic of the employed photonic crystal cavity design.

[11] The optical losses in the system are a result of primarily the energy escaping the PhC cavity without being coupled back to the bus waveguide, and of the transmission losses in the waveguide.

distance between the waveguide and the 2D cavity – and any modification of it – in an in-plane scheme can only be discrete, and is defined by the periodicity of the 2D photonic crystal lattice (imposed by the design of the device). In the considered vertical coupling architecture, the bus waveguide is separated from the photonic crystal cavity by the top cladding layer of the cavity, the thickness of which can be precisely controlled. In this way, the control of the separation distance – and therefore of the coupling rate – between the waveguide and the cavity (not necessarily in discrete steps) provides a means for tuning the reflectivity of the system, the latter being an appealing resonant reflector feature. Finally, as the bus waveguide is located above the photonic crystal cavity, decreasing the interval between them has much less detrimental impact on the *Q*-factor of the cavity as, in this scheme, the planar symmetry of the 2D lattice is not strongly perturbed.

2.4.3 The Device

As discussed above, the function of the aforementioned vertically coupled photonic crystal cavity-waveguide component [1, 34] as a resonant reflector is of interest for this work. It can therefore be easily understood according to Section 2.4.2, that the control of the coupling rate between the two parts (Q_C) is of particular importance here. As previously mentioned, the coupling efficiency in the vertical coupling scheme is dependent on the spatial overlap and the *k*-space distribution overlap between the bus waveguide and the PhC cavity modes (which have a dissimilar effective refractive index). It is thus clear that Q_C can be controlled by changing the physical properties of the bus waveguide (e.g. dimensions, material), the PhC cavity parameters (e.g. lattice constant, lattice structure), or the thickness of the buffer oxide layer between them. Additionally, a PhC cavity design with relatively high intrinsic *Q*-factor (Q_0) in an oxide-clad configuration needs to be employed to ensure a narrow-linewidth reflection.

Based on these considerations and taking into account the effect of oxide cladding on different cavity designs [36, 38], the line defect modulated [27] and the dispersion adapted (DA) [28] PhC cavity designs were considered for this project. Intrinsic *Q*-factors (Q_0) in the order of 10^5 have been demonstrated with both designs when oxide-clad [34, 36] – a sufficiently high performance level for the requirements of the project. The DA PhC cavity design was selected to be predominantly employed in the experiments presented in this thesis. Although it does not offer the highest possible FSR (which results in the appearance of more than one localized energy states inside the band gap), the DA configuration was chosen for technological reasons: it offers a good mode overlap with the low-index bus waveguides used, and it exhibits high disorder stability (i.e. fabrication tolerance). Additionally, small fabrication variations affect its *k*-space distribution negligibly, inducing only insignificant changes in the overlap intensity with the bus waveguide mode, and hence resulting in a more stable performance of the entire system.

Accordingly, SU8 polymer and silicon nitride (Si_3N_4) were considered for the waveguide material in this project. SU8 was selected for the experiments presented here; this choice simplifies the fabrication process as there are no deposition steps required (as would be the case for Si_3N_4). Moreover, the lower refractive index of SU8 ($n \approx 1.58$) allows for larger modal areas

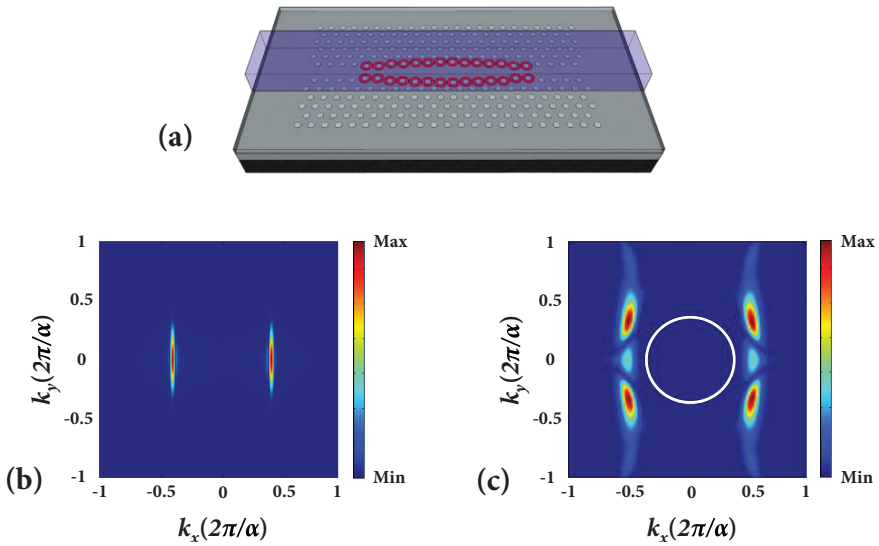

Figure 2.9 (a) Conceptual representation of the resonant reflector device. A low refractive index SU8 polymer waveguide is vertically coupled to a Dispersion Adapted (DA) photonic crystal cavity (defined by the PhC holes marked in red). The two parts are separated by a layer of Spin-on-Glass (SOG) that also acts as a top oxide cladding for the cavity. *K*-space distribution of the dominant electric field (b) of a single-mode bus waveguide, and (c) of the first-order mode of a DA PhC cavity. The white circle indicates the light-cone, assuming oxide cladding.

and lower insertion losses. In this way high coupling to optical fibers and to the mode of Semiconductor Optical Amplifiers (SOAs) can be achieved. This property is in general desirable as the component is employed as an output mirror in an External Cavity (EC) laser architecture. The height and width of the bus waveguide were chosen to be ~2.1 μm and ~3 μm, respectively, aiming at achieving as large cross-sections (and consequently coupling efficiency) as possible, under single (TE) mode operation[12].

A conceptual representation of the resonant reflector component used for this thesis, as well as indicative *k*-space distributions of the dominant electric field of a single-mode SU8 waveguide and of a DA PhC cavity[13], are shown in **Fig. 2.9**. Details on the fabrication of the utilized here reflector devices can be found in Chapter 3. Even though a combination of DA PhC cavities and SU8 bus waveguides was chosen for this project for the reasons explained above, the vertical coupling scheme allows coupling between different types of PhC cavities and bus waveguides, offering flexibility in the choice of parameters (e.g. FSR, *Q*-factor, waveguide cross-section). Indicatively, the use of other low-index materials (e.g. Si_3N_4) for the bus waveguides, along with the potential of employing different PhC cavity designs (e.g. line defect modulated cavity design), have been previously demonstrated [34, 41]. In general, a given PhC cavity design can be engineering to exhibit a *k*-space distribution suitable for matching that of a specific bus waveguide, depending on the properties desired by the application in focus.

---

[12] Even though the higher order mode that occurs at larger waveguide cross-sections would account for very little energy (compared to the fundamental mode) and would not have a *k*-space overlap with the PhC cavity modes, single-mode functionality was selected to minimize the instabilities in the laser cavity.

[13] The *k*-space distribution of the 1st order mode of a DA cavity is shown.

2.5 Laser Cavity with Resonant Reflector Based on Waveguide Vertically Coupled to a Photonic Crystal Cavity

Having seen the reflective properties of the vertically coupled waveguide-photonic crystal cavity system of [34], a qualitative description of an External Cavity laser configuration that utilizes it as a resonant reflector is presented in this paragraph. For a better understanding, the examined External Cavity (EC) laser configuration (with a vertically coupled waveguide-cavity reflector) is described in terms of generic EC and semiconductor laser cavities (**Fig. 2.10** shows a schematic representation of the three configurations and the association of the respective parts).

For a generic two-mirror semiconductor laser configuration (as shown in **Fig. 2.10a**), it holds that [42]

$$\gamma_{xy} g_{th} L_a = \alpha_{ia} L_a + \alpha_{ip} L_p + ln\left(\frac{1}{R_m}\right) \quad \textbf{(2.11)}$$

where γ_{xy} is the transverse confinement factor, g_{th} is the threshold material gain, and α_{ia} and α_{ip} are the internal losses in the active and the passive sections of the cavity, respectively. R_m is the mean mirror intensity reflection, defined as $R_m = r_1 r_2$, with r_1 and r_2 being the amplitude reflectivities of the two laser cavity mirrors. In laser cavities with an active section much larger than the emitted wavelength (i.e. $L_a >> \lambda$) – as the ones considered in this project[14], the longitudinal confinement factor of the cavity can be approximated by $L_a/L = \gamma_z$, with $L = L_a + L_p$ the total laser cavity length. By dividing by L, and considering $\gamma_{xy} L_a/L \approx \gamma_{xy} \gamma_z = \gamma$ to be the 3D confinement factor of the electric field mode in the gain material[15], Eq. 2.11 becomes [42]

$$\gamma g_{th} = \langle \alpha_i \rangle + \left(\frac{1}{L}\right) ln\left(\frac{1}{R_m}\right) \quad \textbf{(2.12)}$$

where $<\alpha_i>$ is the average internal loss, defined by

$$\langle \alpha_i \rangle = \frac{(\alpha_{ia} L_a + \alpha_{ip} L_p)}{L}. \quad \textbf{(2.13)}$$

Similarly, it is common to define a mirror loss term [42]

$$\alpha_m = \frac{1}{L} ln\left(\frac{1}{R_m}\right) \quad \textbf{(2.14)}$$

so Eq. 2.12 turns to

$$\gamma g_{th} = \langle \alpha_i \rangle + \alpha_m. \quad \textbf{(2.15)}$$

An external cavity laser can be seen as a laser cavity with three mirrors with intensity reflection coefficients r_1, r_2 and r_3, with r_2 corresponding to the reflectivity at the interface between the active and the passive regions and r_3 to the reflectivity of the external reflector (as shown in

[14] λ is the emitted wavelength, which in this project is considered to be ~ 1550nm.

[15] More precisely, the confinement factor $\gamma = \gamma_x \gamma_y \gamma_z$ expresses the electron-photon overlap factor V/V_P, with V being the active region volume occupied by electrons and V_P the laser cavity volume occupied by photons ($V_P > V$).

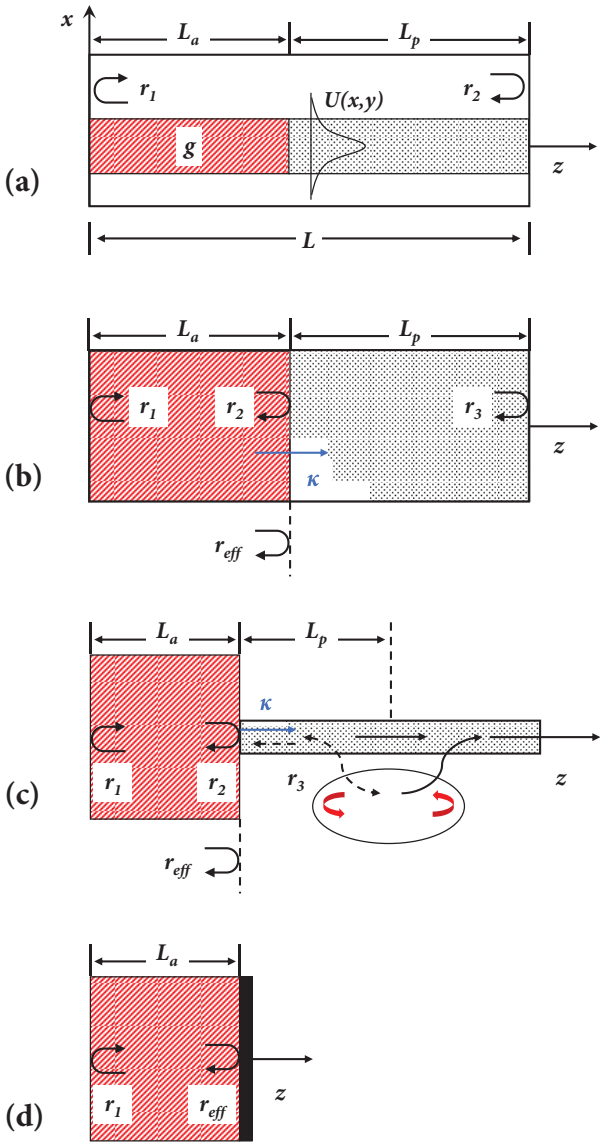

Figure 2.10 Schematic representation of (a) a generic two-mirror semiconductor laser cavity, (b) an external cavity laser, and (c) of an external cavity laser using a resonant external reflector – here a vertically coupled waveguide-photonic crystal cavity (represented as an oval for simplicity) system; the backwards propagating component coupled to the bus waveguide from the photonic crystal cavity provides resonant optical feedback. In all cases, the oscillation in the laser cavity is considered to happen along the z-axis, with $U(x,y)$ being the TE field profile. L_a is the length of the active section (shadowed in red) that provides the laser cavity with gain (g) and L_p is the length of the passive section (shadowed in grey). $L = L_p + L_a$ is the total length of the laser cavity. r_1, r_2 and r_3 are the coefficients denoting the intensity reflection at different interfaces of the laser cavity. κ is the coefficient that describes the intensity coupling between the active and the passive parts. In external cavity laser configurations ((b) and (c)), the influence of the passive section and of the external mirror can be substituted for steady-state analyses by an effective mirror with intensity reflection r_{eff} that plays the role of the second (output) mirror in an equivalent two-mirror model, as shown in (d).

Fig. 2.10b and **2.10c**). The laser output is considered to be received at the end of the external mirror. In such a configuration, it is assumed that $r_2 << r_3$ [43] for the laser to operate on an external cavity mode. For the external cavity lasers of this project, comprising a SOA with a reflective end (RSOA) and a vertically coupled waveguide-photonic crystal cavity chip (**Fig. 2.10c**), the minimization of r_2 is achieved by using AR coatings on all facets of the RSOA-reflector chip interface (i.e. on the output facet of the RSOA and on both facets of the bus waveguide of the reflector chip). Respectively, r_1 is obtained by a reflector (HR coating or a fibre reflector) at the other end of the RSOA, while r_3 is provided by the external photonic crystal cavity-based reflector, as described in Section 2.4. In this scheme, the optical feedback is narrow-band and occurs at the resonance of the photonic crystal cavity, with the reflectivity being $r_3 = Q_T/Q_C$ according to Eq. 2.9.

In an external cavity laser, assuming a steady-state analysis like the one here, the influence of the external mirror can be accounted for by replacing the passive section (represented by L_p in **Fig. 2.10b** and **2.10c**) with an effective mirror of reflectivity r_{eff}. Assuming all reflectivities to be positive and real and $r_2 \to 0$ (as previously discussed), the effective mirror reflectivity of an external cavity laser with a coupled PhC cavity-waveguide reflector can be defined as

$$r_{eff} = \kappa^2 r_3. \tag{2.16}$$

where κ is the coefficient describing the intensity coupling between the active and passive parts. In the considered configuration, κ expresses the coupling between the RSOA and the bus waveguide of the external reflector (which depends on the matching of two modes with different profiles and on the alignment between the two parts), and thus $\kappa \neq 1$ as and cannot be ignored. Under the above assumptions, the examined external cavity laser configuration of **Fig. 2.10c** can be modelled as an equivalent two-mirror cavity with intensity reflectivities r_1 and r_{eff}, and output received at the end of the mirror with reflectivity r_{eff} (as shown in **Fig. 2.10d**). By substituting r_2 with r_{eff} in Eq. 2.11 and 2.12, its threshold gain can be written as

$$\gamma g_{th} = \langle \alpha_i \rangle + \left(\frac{1}{L}\right) ln\left(\frac{1}{r_1 r_{eff}}\right) = \langle \alpha_i \rangle + \left(\frac{1}{L}\right) ln\left(\frac{1}{r_1 \kappa^2 r_3}\right) \tag{2.17}$$

and the mirror loss term of Eq. 2.14 as

$$\alpha_m = \frac{1}{L} ln\left(\frac{1}{r_1 \kappa^2 r_3}\right) \tag{2.18}$$

Attention must be paid to the fact that the total laser cavity length L in Eq. 2.17 and 2.18 should be $L = L_a + L_{eff}(\lambda)$, an aggregate of the length of the active section L_a and of an effective passive length $L_{eff}(\lambda)$. The effective length $L_{eff}(\lambda)$ accounts for the phase contribution of the passive section (L_p) and the wavelength-dependent phase contribution by the photonic crystal cavity in

the external reflector[16]. Under this consideration, the wavelength spacing between two adjacent longitudinal modes m and $m+1$ in the studied EC laser can be calculated, as for a two-mirror semiconductor laser, using the formula for the Free Spectral Range (FSR) of a Fabry-Pérot (FP) cavity

$$\delta\lambda = \frac{\lambda^2}{2(\bar{n}_{ga}L_a + \bar{n}_{gp}L_{eff}(\lambda))} \tag{2.19}$$

where $\bar{n}_{ga}$ and $\bar{n}_{gp}$ are the group effective indices[17] for the active and the passive regions, respectively [42].

Following on the above discussion, the output power P_o received at the external mirror end of the laser (or the effective mirror end in the equivalent two-mirror configuration), is given by

$$P_o = \eta_d \frac{h\nu}{q}(I - I_{th}) \tag{2.20}$$

where h is Planck's constant, q is the elementary charge, ν is the frequency of the lasing wavelength (and therefore also the resonance frequency of the photonic crystal cavity), I is the driving current, I_{th} is the threshold current and η_d is the differential quantum efficiency of the laser. As a laser cavity with a lossy external mirror is considered here (see Section 2.4.2), the differential quantum efficiency is given by [42]

$$\eta_d = F_1 \eta_i \frac{\alpha_m}{\langle\alpha_i\rangle + \alpha_m} \tag{2.21}$$

with $\langle\alpha_i\rangle$ being the average internal loss given by Eq. 2.12[18], α_m being the mirror loss given by Eq. 2.18 and η_i the internal quantum efficiency, i.e. the fraction of terminal current that generates carriers in the active region (which, given the quality of current state-of-the-art SOAs, can be assumed to be unity). Finally, F_1 expresses the fraction of power delivered from the output facet, relative to the total power coupled out of the cavity by the mirrors. In this way, F_1 accounts for the fact that not all the mirror loss of the output mirror is delivered outside the laser cavity as output power (since the output mirror in this case is the PhC-based reflector of Section2.4, for which it was shown that $T+R \neq 1$). In the considered laser cavity, the fraction F_1 of light obtained at the output end of the bus waveguide on the resonant reflector chip is given by

$$F_1 = \frac{t_c^2}{\left(1-r_{eff}^2\right) + \frac{r_1}{r_{eff}}\left(1-r_1^2\right)} \tag{2.22}$$

---

[16] The effective passive length can be defined as $L_{eff} = -\,\mathrm{d}\varphi_{eff}/2\,\mathrm{d}\beta_p$, with $\mathrm{d}\varphi_{eff}$ and $\mathrm{d}\beta_p$ derivatives dependent on frequency of φ_{eff} and β_p [42]. φ_{eff} represents the effective round-trip phase, i.e. twice the sum of all the phase-changing contributions in the passive section of the laser cavity (in the considered case, the phase change due to the propagation in the bus waveguide and the wavelength-dependent phase contribution of the PhC cavity). β_p is the real propagation constant in the axial direction (z-axis) of the passive part of laser cavity (including the external mirror) given by $\beta_p = 2\pi\bar{n}/\lambda$ ($\bar{n}$ is the effective index of refraction for the mode in the passive part).

[17] The group effective index of the j-th region is defined as $\bar{n}_{gj} = \bar{n}_j + (\partial\bar{n}/\partial\omega)$, according to [42].

[18] Again $L_{eff}(\lambda)$ should be used instead of L_a and the total cavity length should be $L = L_a + L_{eff}(\lambda)$.

with t_c the intensity transmission of the external reflector given by $t_c = Q_T/Q_0$, according to Eq. 2.8 (as lasing only occurs at resonance of the photonic crystal cavity). In this way, the slope efficiency of the laser η_s, following the traditional definition, can be written as

$$\eta_s = \frac{dP_o}{dI} = \left[\frac{h\nu}{q}\right]\eta_d = \left[\frac{h\nu}{q}\right]F_1\frac{\alpha_m}{\langle\alpha_i\rangle+\alpha_m} = \left[\frac{h\nu}{q}\right]\frac{t_c^2}{\left(1-r_{eff}^2\right)+\frac{r_1}{r_{eff}}\left(1-r_1^2\right)}\frac{\alpha_m}{\langle\alpha_i\rangle+\alpha_m} \quad \textbf{(2.23)}$$

In general, the longitudinal mode selectivity in a laser cavity is determined by the combination of the mirror loss α_m with the net propagation gain (i.e. $\gamma_{xy}g - \alpha_i$) that results in a single net gain maximum, to which the closest mode will be selected. In the EC architecture presented here, single longitudinal mode operation (i.e. good Side Mode Suppression Ratio – SMSR) is achieved by the fact that the vertically coupled waveguide-photonic crystal system acts as an optical filter. The wavelength-selective external reflection ensures that a mirror loss minimum occurs only for wavelengths within the (narrow) linewidth of the photonic crystal cavity resonance, providing an inherent mechanism towards the selection of a single mode. A graphic illustration of the situation is given in **Fig. 2.11**. An additional attractive feature of the chosen photonic crystal cavity-based external reflector is that, as shown in Section 2.4, the magnitude and linewidth of its reflectivity R can be tuned by controlling its design and fabrication parameters (i.e. the intrinsic quality factor Q_0 of the selected photonic crystal cavity design and the coupling between the cavity and the bus waveguide through Q_C), resulting in better mode selectivity.

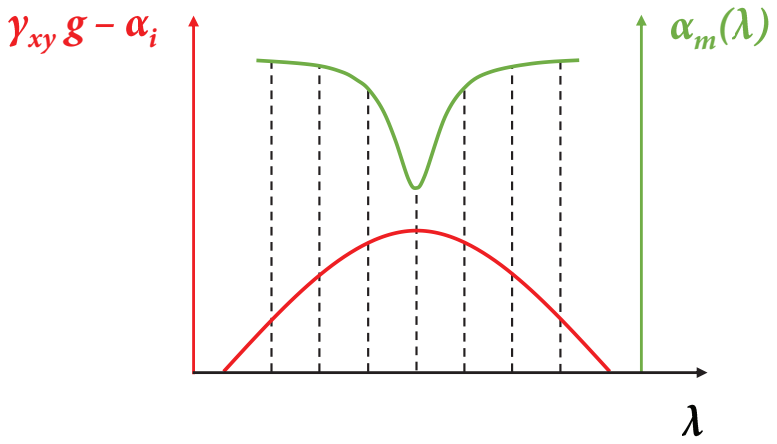

Figure 2.11 Schematic illustration of net propagation gain $\gamma_{xy}g - \alpha_i$, (red) and the net resonant mirror loss α_m (green), as a function of wavelength, for an EC laser with a vertically coupled bus wavguide-PhC cavity external reflector. The dashed lines represent the modes of the total EC laser cavity, the spacing of which is given by $\boldsymbol{\delta\lambda = \lambda^2 / [2\,(\bar{n}_{ga}L_a + \bar{n}_{gp}L_{eff}(\lambda))]}$.

Based on the above observation, it is easily apparent that one of the major features of external cavity lasers, wavelength tuning, can be straightforwardly achieved in the presented EC laser scheme, by simply tuning the resonance wavelength of the photonic crystal cavity in the reflector. Given the previously demonstrated low switching energies for photonic crystal cavities [5], it is understandable that upon proof of its function, the examined EC laser configuration can be a potentially attractive candidate for energy-efficient wavelength tunability or modulation.

2.6 Discussion

In this chapter I have provided a short overview on the fundamentals of photonic band gap theory, 2D photonic crystals and photonic crystal cavities. Photonic crystal cavities are particularly relevant to Silicon photonic circuits for chip-scale WDM networks as they exhibit small footprint, precise wavelength control and very high Q/V ratios that translate to strong light-matter interaction and consequently low switching energies. Further, I explained how an optical filter with a low-index dielectric waveguide vertically coupled to an oxide-clad Silicon photonic crystal cavity can act as a wavelength-selective reflector, the reflectivity of which can be tuned by controlling the fabrication parameters of the filter (more specifically the intrinsic quality factor of the photonic crystal cavity, and the coupling rate between the cavity and the bus waveguide).

Based on the above, I presented the main scope of this project, which is the examination of the possibility to employ the aforementioned reflective component as an external resonant mirror in External Cavity (EC) laser configurations that also comprise a III-V-based Reflective SOA (RSOA). External Cavity lasers are in general attractive as they allow the independent design, fabrication and optimization of the passive and the active parts, and make cost-effective use of the III-V materials. The proposed EC laser architecture is especially appealing for Silicon photonic optical interconnects as it features a Silicon photonic crystal cavity-based reflector, which implies high integration density, and precise and well-controlled lasing wavelength registration. Additionally, the lasing wavelength dependence on the resonance of the photonic crystal cavity of the reflective chip, combined with the low switching energies demonstrated in photonic crystal cavities, indicate its potential for energy efficient wavelength tuning/modulation. I complete the chapter by providing a conceptual description of an abstract external cavity laser utilizing a vertically coupled waveguide-photonic crystal cavity component as an external resonant reflector.

In Chapters 4 and 5, I will demonstrate the functionality of different EC laser configurations employing a vertically coupled waveguide-photonic crystal cavity-based reflector, while in Chapter 6 the possibility of achieving direct wavelength modulation in the proposed EC laser configuration is discussed and some directions for potential future work are given.

References

[1] M. Qiu, "Vertically coupled photonic crystal optical filters," *Optics Letters,* vol. 30, no. 12, pp. 1476-1478, JUN 2005.

[2] J. E. Cunningham, I. Shubin, X. Zheng, T. Pinguet, A. Mekis, Y. Luo, H. Thacker, G. Li, J. Yao, K. Raj and A. V. Krishnamoorthy, "Highly-efficient thermally-tuned resonant optical filters," *Optics Express,* vol. 18, no. 18, pp. 19055-19063, AUG 2010.

[3] Q. Xu, B. Schmidt, S. Pradhan and M. Lipson, "Micrometre scale silicon electro optic modulator," *Nature,* vol. 435, pp. 325-327, MAY 2005.

[4] T. Tanabe, K. Nishiguchi, E. Kuramochi and M. Notomi, "Low power and fast electro-optic silicon modulator with lateral pin embedded photonic crystal nanocavity," *Optics Express,* vol. 17, no. 25, pp. 22505-22513, DEC 2009.

[5] K. Debnath, L. O'Faolain, F. Y. Gardes, A. Steffan, G. T. Reed and T. F. Krauss, "Cascaded modulator architecture for WDM applications," *Optics Express,* vol. 20, no. 25, pp. 27420-27428, DEC 2012.

[6] J. K. Doylend, P. E. Jessop and A. P. Knights, "Silicon photonic resonator enhanced defect mediated photodiode for sub-bandgap detection," *Optics Express* , vol. 18, no. 14, pp. 14671-14678, JUL 2010.

[7] K. Debnath, F. Y. Gardes, A. P. Knights, G. T. Reed, T. F. Krauss and L. O'Faolain, "Dielectric waveguide vertically coupled to all-silicon photodiodes operating at telecommunication wavelengths," *Applied Physics Letters,* vol. 102, p. 171106, APR 2013.

[8] N. Sherwood-Droz, H. Wang, L. Chen, B. G. Lee, A. Biberman, K. Bergman and M. Lipson, "Optical 4x4 hitless silicon router for optical networks on chip," *Optics Express* , vol. 16, no. 29, pp. 15915-15922, SEP 2008.

[9] A. Zilkie, P. Seddighian, B. J. Bijlani, W. Qian, D. C. Lee, S. Fatholoumi, J. Fong, R. Shafiiha, D. Feng, B. J. Luff, X. Zheng, J. E. Cunningham, A. V. Krishnamoorthy and M. Asghari, "Power-Efficient III-V/Silicon external cavity DBR lasers," *Optics Express,* vol. 20, no. 21, pp. 23456-23462, OCT 2012.

[10] T. Creazzo, E. Marchena, S. B. Krasulick, P. K. L. Yu, D. Van Orden, J. Y. Spann, C. C. Bliving, L. He, H. Cai, J. M. Dallesasse, R. J. Stone and M. Amit, "Integrated tunable CMOS laser," *Optics Express,* vol. 21, no. 23, p. 28048, NOV 2013.

[11] S. Tanaka, S.-H. Jeong, S. Sekiguchi, T. Kurahashi, Y. Tanaka and K. Morito, "High-output power, single-wavelength silicon hybrid laser using precise flip-chip bonding technology," *Optics Express,* vol. 20, no. 27, pp. 28057-28069, DEC 2012.

[12] T. Chu, N. Fujioka and M. Ishizaka, "Compact, lower-power-consumption wavelength tunable laser fabricated with silicon photonic-wire waveguide micro-ring resonators," *Optics Express,* vol. 17, no. 16, pp. 14063-14068, AUG 2009.

[13] S. Lin, S. S. Djordjevic, J. E. Cunningham, I. Shubin, Y. Luo, J. Yao, G. Li, H. Thacker, J.-H. Lee, K. Raj, X. Zheng and A. V. Krishnamoorthy, "Vertical-coupled high-efficiency tunable III-V-CMOS SOI hybrid external-cavity laser," *Optics Express,* vol. 21, no. 26, pp. 32425-32431, DEC 2013.

[14] Y. Zhang, S. Yang, H. Guan, A. E.-J. Lim, G.-Q. Lo, P. Magill, T. Baehr-Jones and M. Hochberg, "Sagnac loop mirror and micro-ring based laser cavity for silicon-on-insulator," *Optics Express,* vol. 22, no. 15, pp. 17872-17879, JUL 2014.

[15] Lord Rayleigh Sec. R. S., "XVII. On the maintenance of vibrations by forces of double frequency, and on the propagation of waves through a medium endowed with a periodic structure," *Philosophical Magazine Series 5,* vol. 24, no. 147, 1887.

[16] E. Yablonovich, "Inhibited spontaneous emission in solid-state physics and electronics," *Physical Review Letters,* vol. 58, no. 20, pp. 2059-2062, May 1987.

[17] J. Sajeev, "Strong Localization of Photons in Certain Disordered Dielectric Superlattices," *Physical Review Letters,* vol. 58, no. 23, pp. 2486-2489, JUN 1987.

[18] E. Yablonovich, T. J. Gmitter and K. M. Leung, "Photonic band structure: The Face-Centered-Cubic case employing nonspherical atoms," *Physical Review Letters,* vol. 67, no. 17, pp. 2095-2098, OCT 1991.

[19] T. F. Krauss, R. M. DeLaRue and S. Brand, "Two-dimensional photonic-bandgap structures operating at near-infrared wavelengths," *Nature,* vol. 383, pp. 699-702, OCT 1996.

[20] R. Biswas, M. M. Sigalas, K.-M. Ho and S.-Y. Lin, "Three-dimensional photonic band gaps in modified simple cubic lattices," *Physical Review B,* vol. 65, p. 205121, MAY 2002.

[21] J. D. Joannopoulos, S. G. Johnson, J. N. Winn and R. D. Meade, Photonic Crystals: Molding the Flow of Light, Second edition, Princeton University Press, 2008.

[22] F. Bloch, "Über die Quantenmechanik der Elektronen in Kristallgittern," *Zeitschrift für Physik,* vol. 52, no. 7, p. 555–600, JUL 1929.

[23] S. John, "Strong Localization of Photons in Certain Disordered Dielectric Superlaticces," *Physical Review Letters,* vol. 58, no. 23, pp. 2486-2489, JUN 1987.

[24] S. Fan, J. N. Winn, A. Devenyi, J. C. Chen, R. D. Meade and J. D. Joannopoulos, "Guided and Defect Modes in Periodic Dielectric Waveguides," *Journal of the Optical Society of America B,* vol. 12, no. 7, pp. 1267-1272, JUL 1995.

[25] Y. Akahane, T. Asano, B.-S. Song and S. Noda, "High-Q Photonic Nanocavity in a Two-Dimensional Photonic Crystal," *Nature,* vol. 425, pp. 944-947, OCT 2003.

[26] B.-S. Song, S. Noda, T. Asano and Y. Akahane, "Ultra-high-Q Photonic Double-Heterostructure Nanocavity," *Nature Materials,* vol. 4, pp. 207-210, 2005.

[27] E. Kuramochi, M. Notomi, S. Mitsugi, A. Shinya, T. Tanabe and T. Watanabe, "Ultrahigh Q Photonic Crystal Nanocavities Realized by the Local Width Modulation of a Line Defect," *Applied Physics Letters,* vol. 88, p. 041112, 2006.

[28] K. Welna, S. L. Portalupi, M. Galli, L. O'Faolain and T. F. Krauss, "Novel Dispersion Adapted Photonic Crystal Cavity with Improved Disorder Stability," *IEEE Journal of Quantum Electronics,* vol. 48, no. 9, pp. 1177-1183, SEP 2012.

[29] G.-H. Duan, C. Jany, A. Le Liepvre, M. Lamponi, A. Accard, D. Make, F. Lelarge, S. Messaoudene, D. Bordel, J.-M. Fedeli, S. Keyvaninia, G. Roelkens, D. Van Thourhout, D. J. Thomson, F. Y. Gardes and G. T. Reed, "III-V on Silicon Transmitters," in *Optical Fiber Communication Conference (OFC)*, Anaheim, CA, US, 2013.

[30] Z. Zhou, B. Yin and J. Michel, "On-chip light sources for silicon photonics," *Light: Science & Applications,* vol. 4, pp. 1-13, NOV 2015.

[31] S. Keyvaninia, S. Verstuyft, S. Pathak, F. Lelarge, G.-H. Duan, D. Bordel, J.-M. Fedeli, T. De Vries, B. Smalbrugge, E. J. Geluk, J. Bolk, M. Smit, G. Roelkens and D. Van Thourhout, "III-V-on-Silicon multi-frequency lasers," *Optics Express,* vol. 21, no. 11, pp. 13675-13683, MAY 2013.

[32] T. Baba, S. Akiyama, M. Imai, N. Hirayama, H. Takahashi, Y. Noguchi, T. Horikawa and T. Usuki, "50-Gb/s ring-resonator-based silicon modulator," *Optics Express,* vol. 21, no. 10, pp. 11869-11876, MAY 2013.

[33] J. O'Brien, O. Painter, R. Lee, C. C. Cheng, A. Yariv and A. Scherer, "Lasers incorporating 2D photonic bandgap mirrors," *Electronics Letters,* vol. 32, no. 24, pp. 2243-2244, NOV 1996.

[34] K. Debnath, K. Welna, M. Ferrera, K. Deasy, D. G. Lidzey and L. O'Faolain, "Highly efficient optical filter based on vertically coupled photonic crystal cavity and bus waveguide," *Optics Letters,* vol. 38, no. 2, pp. 154-156, 2013.

[35] M. Notomi, K. Nozaki, A. Shinya, M. Shinji and K. Eiichi, "Toward fJ/bit optical communication in a chip," *Optics Communications,* vol. 314, pp. 3-17, MAR 2014.

[36] B.-S. Song, S.-W. Jeon and S. Noda, "Symetrically glass-clad photonic crystal nanocavities with ultrahigh quality factors," *Optics Letters,* vol. 36, no. 1, pp. 91-93, JAN 2011.

[37] T. P. White, L. O'Faolain, J. Li, L. C. Andreani and T. F. Krauss, "Silica-embedded silicon photonic crystal waveguides," *Optics Express,* vol. 16, no. 21, pp. 17076-17081, OCT 2008.

[38] S.-W. Jeon, J.-K. Han, B.-S. Song and S. Noda, "Glass-embedded two-dimensional silicon photonic crystal devices with a broad bandwidth waveguide and a high quality nanocavity," *Optics Express,* vol. 18, no. 18, pp. 19361-19366, AUG 2010.

[39] Y. Xu, R. Li, R. K. Lee and A. Yariv, "Scattering-theory analysis of waveguide-resonator," *Physical Review E,* vol. 65, no. 5, pp. 7389-7404, NOV 2000.

[40] P. S. Kilders, "PhD Thesis: Coupling techniques between dielectric waveguides and planar photonic crystals," Unversidad Politécnica de Valencia - Departament de Comunicaciones, Valencia, FEB 2005.

[41] K. Debnath , "PhD Thesis: Photonic Crystal Cavity Based Architecture for Optical Interconnects," School of Physics and Astronomy, University of St Adrews, St Andrews, APR 2013.

[42] L. A. Coldren and S. W. Corzine , Diode Lasers and Photonic Integrated Circuits, New York, NY: J. Wiley & Sons, 1995.

[43] V. Annovazzi-Lodi, S. Merlo and S. Moroni, "Power efficiency of a semiconductor laser with an external cavity," *Optical and Quantum Electronics,* vol. 32, no. 12, pp. 1343-1350, 2000.

Chapter 3

Fabrication Tools and Processes

3.1 Introduction

The following chapter is an overview of the fabrication processes and tools that were used for the completion of the work in this thesis. I will begin this chapter by initially describing the steps that were followed for the fabrication of the samples used in the experiments presented here. I will then introduce photolithography and electron-beam lithography, the two lithographic methods that were used for the formation of doped regions and patterns on the aforementioned. I will then demonstrate the Reactive Ion Etching process, which was used for pattern definition and etch-back purposes. Finally, I will present the electron-beam evaporation process used for the formation of metal contacts and Anti-Reflection (AR) coatings.

3.2 Sample Fabrication

A significant fraction of my work-time on this project was dedicated to the fabrication of the resonant reflector components presented in Section 2.4. In this section I describe the main steps of the process flow (shown in **Fig. 3.1**) that was followed to fabricate the devices/samples used for the measurements and experiments presented in this thesis. Technical details for each step will be given in the following sections.

The reflector devices are fabricated on the 220nm Silicon-on-Insulator (SOI) platform that features a 220 nm thick crystalline Silicon layer on top of a 2-μm layer of SiO_2 (commonly known as Buried Oxide – BOx). An appropriately sized piece (will be referred to as sample for convenience) is cleaved off an 8-inch SOITEC SOI wafer and undergoes ultrasonic cleaning in Acetone and Isopropanol (IPA – **Fig. 3.1a**). Upon cleaning, the sample is spin-coated with a 440-nm layer of the positive electron beam resist ZEP 520A and annealed at 180 ^{0}C for 10 minutes (**Fig. 3.1b**). The desired pattern (including alignment marks and isolation trenches) is defined on the resist using electron-beam lithography (**Fig. 3.1c**). As discussed in Section 2.4.3, the photonic crystal cavity design that was mainly used in this project was the Dispersion Adapted (DA) cavity [1]. **Fig. 3.2** shows the DA photonic crystal cavity design. The resonant response of each device can be tuned either by changing the lattice period a of the photonic crystal or by changing the distance d between the two innermost pairs of holes in the cavity (**Fig. 3.2a**). The patterned sample is developed in Xylene for 45 seconds and ZEP 520A is removed from the exposed

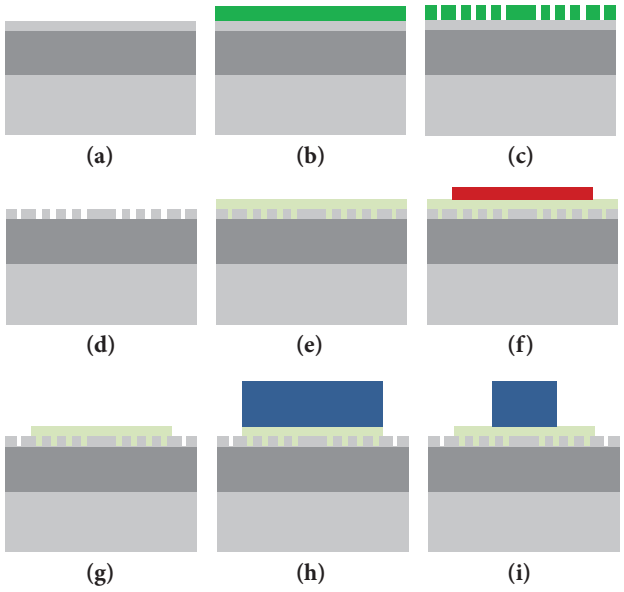

Figure 3.1 Fabrication process flow: (a) A sample of SOI is cleaved and cleaned in Acetone and IPA. (b) The sample is spun with positive e-beam resist – ZEP 520A. (c) The desired pattern (including alignment marks and isolation trenches) is exposed on the resist by e-beam lithography. After the exposure, the sample is developed in Xylene for 45 seconds and ZEP 520A is removed from the exposed regions. (d) Silicon is etched away from the uncovered parts by Reactive Ion Etching (RIE) and the desired pattern is transferred on the Silicon. The patterned sample is then stripped from the remaining resist. (e) The sample is clad with SOG and the thickness of the SOG layer is reduced by RIE. (f) The alignment mark regions are covered and the sample is spun with S1818 photoresist. (g) SOG is selectively removed from the uncovered parts of the sample by RIE, and S1818 is removed by Acetone. (h) The stripped-from-SOG Silicon parts are covered, and the sample is spun with SU8 polymer. (i) Utilizing a 3-point alignment method, SU8 polymer waveguides are formed by electron-beam lithography and development in EC-solvent.

regions (**Fig. 3.1c**). Silicon is etched away from the 'unmasked' parts by Reactive Ion Etching (RIE) with equal parts of CHF_3 and SF_6 and the desired pattern along with the separation trenches and alignment marks are transferred on the Silicon layer of the sample. The etched sample is stripped from the remaining ZEP 520A in 1165 resist remover (**Fig. 3.1d**).

As a following step, the sample is cleaned in Piranha solution (H_2SO_4:H_2O_2 in 3:1 ratio) and spin-coated with a layer of Spin-on Glass (SOG)[1] that fills the holes of the photonic crystal (**Fig. 3.1e**). After spinning, the sample is initially baked at 100 ^{0}C and then annealed at a progressively increasing temperature up to 400 ^{0}C. In this way, a glass layer with properties similar to the ones of SiO2 is formed on top of the silicon photonic crystal cavity, acting as a top oxide cladding (the bottom cladding is provided by the BOx) that improves the symmetry and mechanical stability of the device. The acquired thickness of SOG after annealing is >300nm. A top cladding of ~140nm is required for achieving a good *k*-space distribution overlap between the cavity and the bus waveguide, and for a high cavity *Q*-factor[2], so a further reduction of the thickness of the SOG layer is achieved by RIE with CHF_3. Once the desired thickness of the top

[1] For the devices of this project Flowable Oxide (FOx) by Dow Corning and Accuglass by Honeywell were used. Both products are based on hydrogen silsesquioxane (HSQ).

[2] A SOG layer thickness much larger than the desired is spun for better planarization.

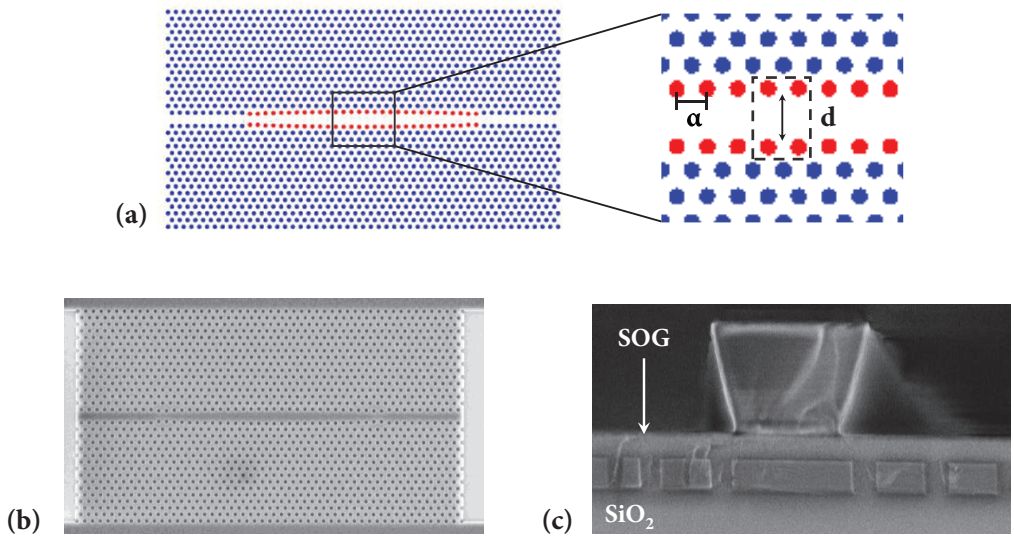

Figure 3.2 (a) Dispersion Adapted (DA) cavity design. The holes marked with red are shifted in order to form the cavity. The resonant response of the DA cavity can be tuned by changing either the photonic crystal lattice period α or the distance d between the two innermost pairs of holes in the cavity (as shown in the close-up). (b) SEM image of a DA photonic crystal cavity. 10 lattice periods are added on each side of the cavity to prevent light leakage in Silicon or air. (c) Cross-sectional SEM image of the device. A low index dielectric (SU8 polymer) waveguide is vertically coupled to a DA photonic crystal cavity. The two parts are separated by a layer of Spin-on Glass (SOG) that also acts as the top cladding of the cavity. The bottom cladding is provided by the SiO_2 layer of the SOI platform (BOx).

cladding is obtained, the regions where the alignment marks lie are covered with Ultraclean Super-Tack, zero-residue tape and the sample is spin-coated with a > 550nm layer of positive photoresist S1818 and annealed at 100 ^{0}C for 2 minutes (**Fig. 3.1f** – the tape is removed prior to the annealing). SOG is etched away from the 'unmasked' parts by RIE with CHF3, uncovering the alignment marks on the Silicon layer (**Fig. 3.1g**). The sample is stripped from S1818 with Acetone and is then rinsed with IPA.

In the final part of the process flow, the bus waveguides are fabricated on top of the oxide-clad photonic crystal cavities. For the work presented in this thesis SU8 polymer (n ≈1.58) was selected for the formation of the waveguides over other alternatives (e.g. Si3N4). As explained in Section 2.4.3, this choice simplifies the fabrication process as, unlike in the case of Si_3N_4, there are no deposition steps required. For the implementation of the waveguides, the sample is cleaned in Piranha solution, spin-coated with a ~2.1-μm layer of SU8 and soft-baked at 100 ^{0}C for 3 minutes. The areas with the alignment marks are yet again covered with zero-residue tape (which is removed prior to soft-baking) in order to maintain the marks 'open'. The waveguide design is transferred on the SU8 layer via electron-beam lithography. A 'three-point alignment' is employed (using the alignment marks on the Silicon layer as reference points) to ensure that that the waveguides are located in the desired position above the cavity. The width of the waveguides is ~3.1 μm; the dimensions of the waveguides are chosen such that high coupling efficiency to the cavity mode is achieved under single mode operation. After a 3-minute post-exposure baking at 100 ^{0}C, the patterned sample is developed in EC-solvent for 20 seconds and SU8 is removed from the un-exposed regions. Upon development, the sample is hard-baked at 180 ^{0}C for 15 minutes.

Once the above steps are completed, the sample is cleaved (typically along a plane perpendicular to the direction of propagation of light in the waveguide) to form a chip with waveguide facets of good optical quality. In order to further reduce facet back-reflections, a ~280nm[3] layer of MgF_2 ($n \approx 1.37$) is deposited by Electron-Beam Physical Vapour Deposition (EBPVD) on both ends of the bus waveguide as an Anti-Reflection (AR) coating. A more detailed description of the fabrication tools and methods used in the above described steps is given in the sections below.

3.3 Photolithography

Photolithography or UV lithography is a process used for patterning a polymer layer on a substrate. It utilizes UV light to transfer a desired pattern to a light-sensitive material called 'photoresist' or simply 'resist', on the substrate. The patterning process is based on the photochemical reaction of the resist to UV photons. More specifically, for positive photoresists the exposed areas become soluble in a developer solvent, while for negative photoresists the exposed areas become resistant to the developer that dissolves only the un-exposed areas. Photolithography can be used for the simultaneous patterning of large substrates (up to an entire wafer), and thus is faster than electron-beam lithography, but its resolution is limited by the wavelength of the light that is used. For this reason, photolithography is typically employed for larger structures, such as trenches, alignment marks, ion implantation windows, and contact vias, where the requirement for high resolution is more relaxed.

Photolithography systems typically define patterns on photoresist using photomasks. A photomask is a quartz plate, one side of which is coated with a UV light blocking film (e.g. Fe_2O_3 or Cr) that carries the desired pattern. The mask allows the selective exposure of only some areas of the photoresists for the formation of the pattern. In the case of a process with multiple lithographic cycles, the substrate can be aligned to a feature on the photomask using the alignment tool of the system. Based on how the pattern is transferred from the photomask to the photoresist on the substrate, photolithography can be divided into three main categories (shown in **Fig. 3.3**): contact lithography, proximity lithography and projection lithography. In contact lithography, a photomask is put in direct contact with the photoresist layer on the substrate, which is then exposed to uniform UV light (**Fig. 3.3a**). Proximity lithography follows the same working principle, but in this case a small gap is left between the photomask and the resist layer on the substrate prior to the exposure (**Fig. 3.3b**). In both contact and proximity lithography, the photomask covers the entire substrate and the exposure of all areas is simultaneous. Unlike contact and proximity masks, projection lithography masks (also known as 'reticules') contain only one die or an array of dies (also known as 'field') and are projected on the wafer multiple times for the creation of the complete pattern. In order for that to be done, an imaging optics system (projection lens) is used between the reticule and the resist layer on the

[3] The thickness d of the AR coating layer is given by $d = \lambda cos\theta/4n$, where λ is the wavelength at which the reduction of back-reflections is desired, θ is the input angle in the waveguide and n is the refractive index of the AR coating material. In most cases, λ = 1550nm and $\theta = 0^o$ are considered.

substrate (**Fig. 3.3c**). During my work, an EVG620 mask aligner, with lamp power of 500 W at a wavelength of 365 nm, was used for contact lithography. The flow of the process is shown in **Fig. 3.4**.

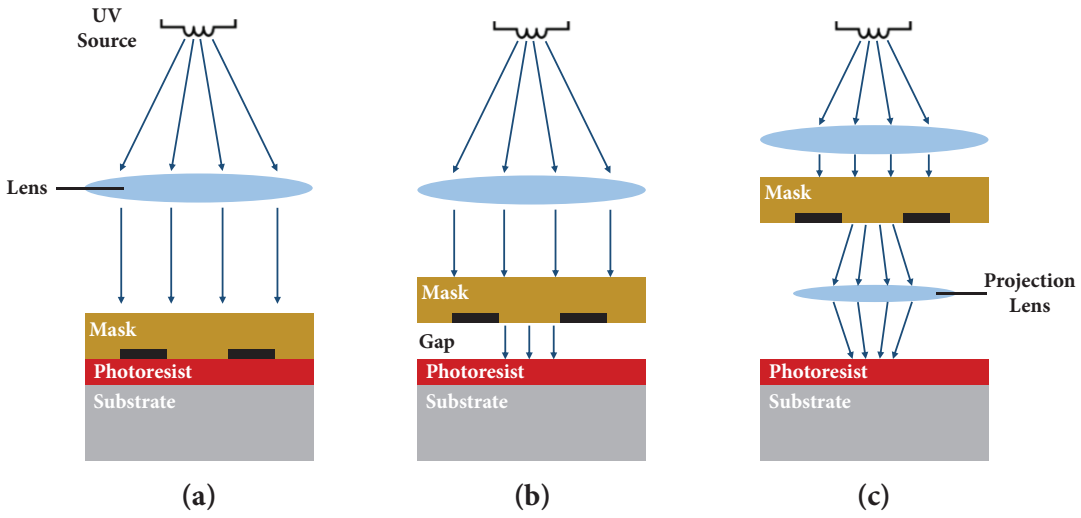

Figure 3.3 Photolithography types. (a) Contact lithography: the photomask is brought in direct contact with the photoresist layer on the substrate. (b) Proximity lithography: a small gap is left between the photomask and the photoresist layer on the substrate. (c) Projection lithography: imaging optics are used between the mask (reticule) and the photoresist layer on the substrate.

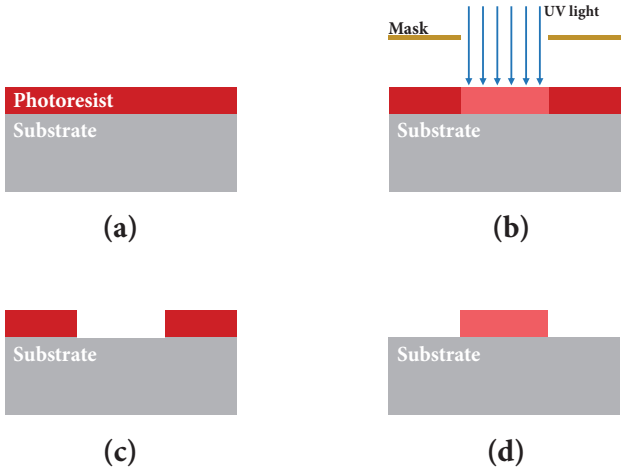

Figure 3.4 Photolithography process flow. (a) Substrate with photoresist on it. (b) Substrate with resist exposed to UV light through a photomask. (c) Substrate with positive photoresist after development. The exposed areas have been removed. (b) Substrate with negative photoresist after development. The exposed areas have not been removed.

3.4 Ion Implantation

Ion implantation is the process during which ions of a material are accelerated by an electric field and are impacted into a substrate. Ion implantation is broadly used in semiconductor device fabrication, to alter the physical or electrical properties of materials. An ion implantation system typically consists of an ion source, where the ions to be implanted are generated, an accelerator tube, where the ions are electrostatically accelerated, and a target chamber, where the target substrate sits. The implanted dose is the actual amount of implanted material, which is defined as the integral of the ion current over time. A schematic representation of an ion implantation system is given in **Fig. 3.5**.

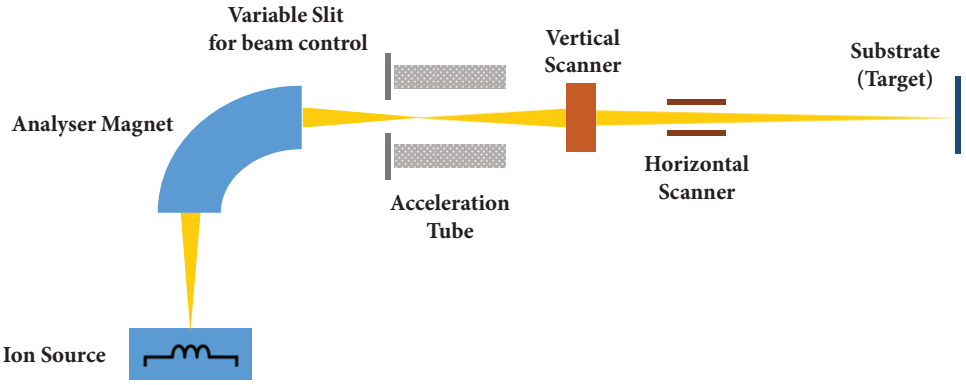

Figure 3.5 Diagram of the parts of an ion implantation system.

One of the most common forms of ion implantation is the insertion of dopants in a semiconductor. During this process, ions, created from gases of elements such as Boron or Phosphorus, are implanted in a semiconductor (in this case, the semiconductor considered is Silicon) and lead to the formation of charge carriers in it after annealing (holes for p-type doping and electrons for n-type doping). Doping is the typical method of forming p-n junctions on Silicon, and the one employed for the formation of the p-n junctions on Silicon-on-Insulator (SOI) that were used for my work. The wafer-scale ion implantation process took place in Tyndall National Institute and is described below.

Initially, alignment marks for the desired design are defined on a SOI wafer by electron-beam lithography. After developing, dry-etching and cleaning the resist used for electron-beam lithography, the wafer is spun with a 1.1 μm-thick layer of Fujifilm HiPR6512 resist. Ion implantation windows are defined in the appropriate areas of the wafer by projection photolithography on an Ultratech UTS1500 stepper. The exposed wafer is then developed in OPD5262 and ions are implanted in the exposed areas using an Eaton NV6200 implanter. The wafer is then stripped from the resist.

The implantation window patterning, the ion implantation, and the wafer cleaning steps are repeated for as many cycles as the number of the different dopants and doses desired. For the used p-n junctions, the wafers underwent four doping cycles - p^+, n^+, p and n, in the order mentioned. Boron ions were used for the p^+ and the p-type doping, and Phosphorus ions for the

n^+ and n- type doping. The wafer is then annealed at 1050° C for the formation of charge carriers and of the actual junctions. The detailed steps of the implantation process and the implanted doses can be found in Appendix A. **Fig. 3.6** depicts the flow of an ion implantation cycle.

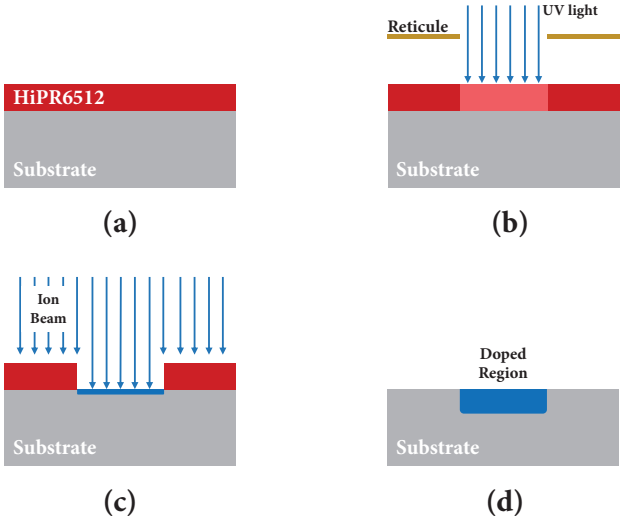

Figure 3.6 Ion implantation cycle flow. (a) Substrate with photoresist on it. (b) Projection photolithography: the resist is exposed to UV light through the reticule. (c) The exposed areas have been removed during the development. Ions of the chosen dopant are then implanted in the desired areas that are not protected by the resist. (b) Substrate after resist stripping and annealing. A doped region with the chosen dopant is formed on and below the surface of the exposed parts. Annealing will lead to the formation of charge carriers (electrons for p-type dopants or holes for n-type dopants).

3.5 Electron-Beam Lithography

Electron-beam (e-beam) lithography is one more process used to define patterns on a substrate. Contrary to photolithography that utilizes light, e-beam lithography uses a focused beam of electrons to expose a film of electron-sensitive resist (e-beam resist) that covers a substrate. The electron beam changes the physical structure of the resist by either breaking the polymer backbone bonds into soluble fragments of lower molecular weight (for positive resists) or by cross-linking the polymer chains to render them less soluble (for negative resists) [2]. In this way, the selective removal is enabled of the exposed (in the case of a positive resist) or the non-exposed regions (in the case of a negative resist) of the resist when developed by the appropriate solvent. The generated pattern on the resist can then be transferred to the substrate by etching.

The electron beam is generated from a thermionic or a field emission source, and is focused and steered by sets of electrostatic and/or magnetic lenses. The lenses can be controlled and set up by the user (typically via a computer interface) for the definition of the desired pattern. Depending on the thickness of the resist film, a specific amount of electrons per unit area, called the 'exposure dose' (measured in $\mu C/cm^2$), is needed for its full exposure. E-beam lithography offers higher resolution (typically down to a few nm) than photolithography, but it is a

significantly slower process due to the fact that it is sequential (there is only one beam of electrons that can expose only a single feature at a time). For that reason, e-beam lithography is mostly preferred in cases where the fabricated volume is relatively low, and high resolution and/or versatility are critical requirements. In this work, e-beam lithography was used for structures with sub-μm features, such as photonic crystals. For all the e-beam lithography steps, I have used a RAITH eLINE plus nanolithography system, with a maximum acceleration voltage of 30 kV and a maximum write-field size for 1000 x 1000 μm^2. The e-beam resist that was predominantly used was Zeon Chemicals ZEP 520A, a high-resolution positive resist that allows the definition of photonic crystal holes and of other sub-100 nm features. Other e-beam resists that were used extensively for the work presented here are Microchem SU-8 (negative) and Polymethyl Methacrylate (PMMA, positive). The details for the resist preparation, exposure and development are provided in **Table 3.1**.

In order to expose large areas, the e-beam lithography system fractures the desired design into segments, known as write fields. The content of each write field is mapped on an exposure grid, each grid-cell of which, represents the smallest 'pixel' that can be exposed with the system. Each write field is exposed separately and the minimum time to expose a given area for a given dose is given by [3]

$$Dose \cdot Area = t \cdot I \tag{3.1}$$

where *Area* is the exposed area, *t* is the time to expose the object, *I* is the electron beam current and *Dose* is the exposure dose. The patterning of the desired design is typically the result of a combination of two independent motions: the deflection of the beam that results in the exposure of the content of a single write field, and the movement of the stage that holds the substrate/sample for the exposure of the adjacent write fields. The size of each grid-cell is dependent on the memory size of the Digital-to-Analogue Converter (DAC) of the e-beam system and on the size of the selected write field. **Fig. 3.7a** depicts how the write field size affects the maximum achievable grid-cell size (i.e. the maximum positioning resolution). The blue continuous lines show the maximum deflection angle of the e-beam, while the red dashed ones represent the minimum angle $\delta\varphi$ that the e-beam can be deflected to. It is apparent that the smaller the write field (WF) size, the finer the grid-cell size δx that can be achieved.

Resist	Thickness (nm)	Baking Temp. (°C)	Baking Time (min)	Exposure Dose ($\mu C/cm_2$)	Developer	Develop. Time (sec)	Developer Temp. (°C)	Resist Stripper
ZEP 520A	440	180	10	55	Xylene	45	45	1165
SU-8	2100	100	3	60	EC Solvent	20	Room Temp.	EC Solvent
PMMA	600	180	5	300	H_2O:IPA (3:7)	55	Room Temp.	Acetone

Table 3.1 Preparation, exposure and development parameters for the main e-beam resists used for this work. A post-exposure bake at 100 °C for 3 minutes is required for SU-8.

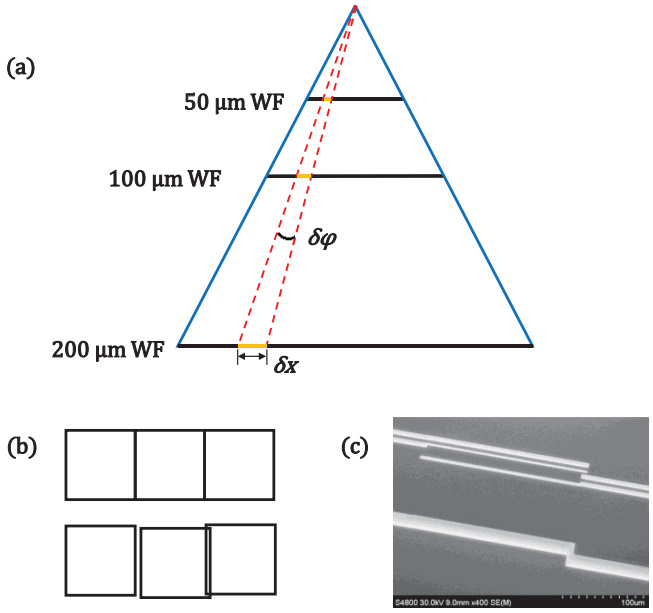

Figure 3.7 (a) Schematic representation of the relationship between the size of the write field (WF) and the maximum achievable positional resolution (or minimum grid-cell size δx). (b) Positioning of adjacent write fields in the ideal case and in a case with stitching errors. (c) SEM image of structures with stitching errors caused by incorrect adjacent write field alignment.

The e-beam system used for this work has a 16-bit DAC, which means that each write field can be divided in 64000 x 64000 grid of cells. The smallest write field size that can be achieved by the considered system is 50 x 50 μm^2, which implies a minimum cell width of 0.78 nm. Respectively, for a write field of 100 x 100 μm^2, the minimum cell width is 1.56 nm, while for the maximum available write field size of the system (1000 x 1000 μm^2) the minimum cell width is 15.63 nm. It is clear that smaller write field sizes offer better resolution, but the size of the write field that can be used for an exposure is often limited by the size of the exposed pattern. If the desired design extends into more than one write fields, the stage needs to move to different positions (corresponding to adjacent write fields) for its exposure to be completed. The stage movement is however less accurate than the deflection of the electron beam within a single write field, and can lead to positioning errors at the borders of adjacent write fields, known as stitching errors. Stitching errors are undesirable as they lead to incorrect transferring of the desired pattern on the substrate, and consequently to scattering losses. **Fig. 3.7b** gives a schematic representation of stitching errors resulting from incorrect positioning of adjacent write fields. In this work, the write field size that was primarily used was 100 x 100 μm^2, as it was found to offer a good trade-off between exposure time and resolution for sub-100nm features, while a low enough number of stitching errors could be achieved for larger structures (e.g. µm-range waveguides).

A critical aspect of e-beam lithography, which also mainly determines the feature resolution limit in a system, is the interaction of the electrons with the e-beam resist and the substrate beneath it. Upon entering the resist, the electrons undergo a series of inelastic scattering events, known as forward scattering, through which they transfer energy to the resist causing the change of its physical structure – a process that has previously been referred to as resist 'exposure'. Apart from exposing the resist, however, forward scattering causes the broadening of the

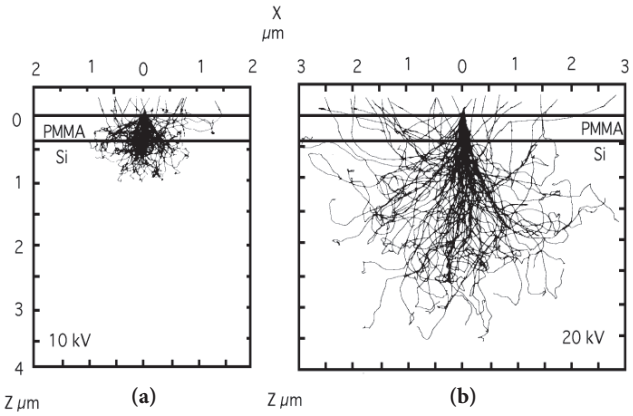

Figure 3.8 Monte Carlo simulations of electron scattering in photoresist (PMMA) on Silicon for electron beam lithography at (a) 10 kV and (b) 20 kV (reproduced from [4], with the permission of AIP Publishing, © 1975).

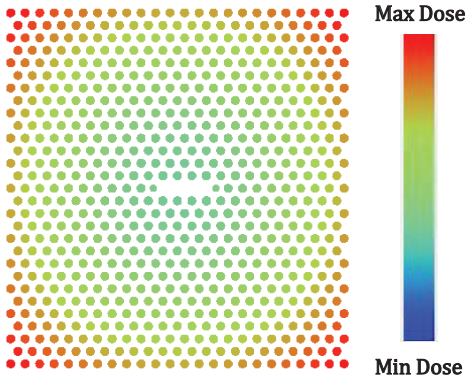

Figure 3.9 L3 cavity design with proximity error correction.

diameter of the electron beam. Evidently, larger resist-layer thickness leads to more pronounced beam broadening by forward scattering. Forward scattering is also observed in the substrate, which is however mostly responsible for the back scattering of a part of the incident electrons. The effects of the combined forward and back scattering of electrons can be seen in Fig. **3.8a** and **3.8b**. Using higher energy electrons (by increasing the acceleration voltage) or a thinner resist layer can decrease the forward scattering, but the generation of secondary back-scattered electrons cannot be avoided. Despite their lower energy, these secondary electrons are capable of changing the physical structure of the resist. That leads to the undesired exposure of resist regions adjacent to regions that are desirably exposed according to the design. The exposure of surrounding resist is responsible for the proximity effect, which is effectively the enlargement of the feature sizes in a given design. The aforementioned phenomenon is particularly undesirable in the fabrication of periodic photonic nanostructures as it leads to a change in their spectral response.

In order to tackle the proximity effect and fabricate devices with the desired feature sizes, NanoPECS™ (Proximity Error Correction Software by RAITH) is used by our research group. NanoPECS is a software that calculates the proximity effect and adjusts accordingly the exposure

dose of each feature in a given design [5]. **Fig. 3.9** shows an example of a proximity error corrected design pattern for an L3 photonic crystal cavity. The central regions of the photonic crystal design are assigned a lower exposure dose as a compensation for the strong proximity effect from the adjacent exposed sites. The regions away from the centre on the other hand, are assigned a relatively higher exposure dose as the proximity effect they experience is weaker, since there are fewer adjacent sites to be exposed. This technique results in a rather homogenous effective exposure dose throughout the entire pattern in practice.

3.6 Reactive Ion Etching

After the exposure of the resist by lithography and development, the generated pattern is transferred to the substrate of interest by Reactive Ion Etching (RIE). RIE is a type of dry etching that uses chemically reactive plasma to remove material from a substrate. The plasma is generated under low pressure, so for this process the substrate is placed in a cylindrical vacuum chamber, on a water-cooled conductive stage that is situated in the bottom part of the chamber as shown in **Fig. 3.10a**. The substrate plate is electrically isolated from the rest of the chamber. A second conductive plate hangs above it. Subsequently, the sample lies between the two plates (in touch with the bottom one), which act as electrodes. The reactive gases are injected in the chamber through small inlets on a circular tube that surrounds the top electrode, and exit to the vacuum pump system on the right. A software-controlled gate valve is used to precisely control the pressure in the chamber at each time. The gate valve can also isolate the chamber from the vacuum pump system during the substrate loading/unloading process, when venting of the chamber to the ambient pressure is required for opening the chamber's lid.

When a strong RF (Radio Frequency) electromagnetic field is applied between the conductive plates/electrodes, its oscillations ionize the molecules of the gas mixture in the chamber by stripping them from electrons, and lead to the initiation of a plasma. In each oscillation cycle of the RF field, the electrically accelerated electrons oscillate with it in the chamber, colliding with either the chamber walls or with the substrate holder. In the first case, the electrons are grounded and therefore do not change the electronic state of the system. In the latter case however, the electrons that collide with the substrate holder plate lead to the build-up of a negative charge and the development of a negative DC voltage on it. At the same time, the plasma exhibits a positive charge due to the high concentration of positive ions, which are much larger in size compared to electrons and move relatively little because of the RF field. The large voltage difference leads the positive ions to move towards the substrate holder, where they collide with the substrate to be etched. The positive ions attack the surface of the substrate and remove material from it both chemically – by reacting with it – and physically – by transferring some of their kinetic energy to it and 'detaching' parts of it. RIE allows very directional (anisotropic) etching, due to the DC induced directionality in the delivery of the reactive ions.

The etching conditions in a RIE system vary heavily with the process parameters: gas types, chamber pressure, gas flow and RF power [6]. The gas mixture and etching recipes depend on the materials of the substrate that is desired to be etched. Sulfur hexafluoride (SF_6) is

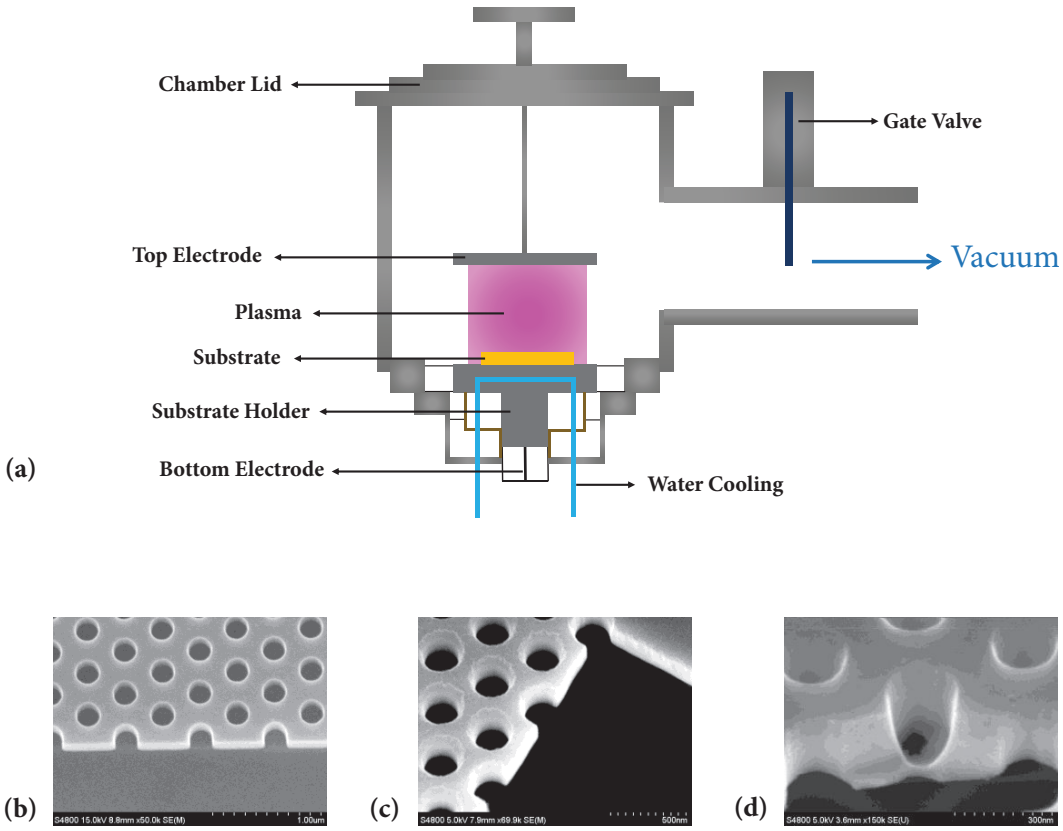

Figure 3.10 (a) Schematic representation of the RIE chamber. The tube on the right connects the chamber to a vacuum pump system and the gate valve controls the chamber pressure. (b) SEM image of photonic crystal etched under optimal parameters. The side walls are vertical, with minimal roughness. (c) SEM image of photonic crystal etched with increased RF power. A widening at the top edge of the holes can be observed. (d) SEM image of insufficiently etched photonic crystal (under-etching). A silicon 'lip' at the bottom of the hole can be observed.

commonly used for etching silicon. In our research group, a mixture of SF_6 and CHF_3 (fluoroform) gases is used for silicon etching. CHF_3 is used for the passivation of the etched side walls, offering additional verticality to the etching. For the etching of Silicon dioxide (SiO_2) or of SOG (HSQ), the reactive gas used was CHF_3, which etches and passivates the side walls at the same time. In order to achieve good etching results with a given RIE system (**Fig. 3.10b**), the etching recipe (etching time, chamber pressure and RF power) should be optimised depending on the substrate to be etched and on the gas types and flow used. Poor optimization of the etching parameters leads to non-optimal etching as shown in **Fig. 3.10c** and **3.10d**. The optimal parameters for the etching of the substrates that were most commonly used in this project are provided in **Table 3.2**.

Substrate	Gases	Flow Rate (sccm)	Etch pressure (mBar)	RF Power (W)	DC Bias (V)	Etch Rate (nm/min)
Silicon	SF_6/ CHF_3	100/100	$5.6x10^{-2}$	19	-210	110
SOG	CHF_3	100	$4x10^{-2}$	40	-510	20

Table 3.2 Etching parameters for the main substrate materials used for this work.

3.7 Electron-Beam Physical Vapour Deposition

3.7.1 Electron-Beam Physical Vapour Deposition

Electron-Beam Physical Vapour Deposition (EBPVD) is a vacuum deposition method used to produce thin films by bombarding a source material (known as target material) with an electron beam. The electron beam is generated from a charged tungsten filament by thermionic emission, field electron emission or the anodic arc method. The target material (in the form of crystals, flakes, wire or ingot) is placed in a water-cooled crucible, which sits at positive potential with respect to the filament. To avoid chemical interaction between the filament and the target material, the filament is kept out of the 'field of view' of the crucible, as shown in **Fig. 3.11**. A magnet is used to accelerate the electron beam and direct it from the source to the target crucible. An additional electric field is used to raster the beam over the crucible's surface. The EBPVD process takes part in a vacuum chamber for the traveling of the electrons from the source to the target crucible to be allowed.

Upon the collision of the electrons with the target, part of the electrons' kinetic energy is converted to thermal energy that heats up the evaporation material and causes it to melt or sublime. In this way, the electron beam transforms atoms of the target material into vapour, under sufficiently high temperature and pressure levels. These gas atoms are then transported by diffusion and precipitate into solid form, coating every surface in the chamber (including that of the substrate) with a thin layer of the target material. The substrate is fastened on the substrate holder, which rotates at a particular speed to allow the uniform deposition of the film over the surface of the substrate. In general, Physical Vapour Deposition (PVD) is advantageous compared to Chemical Vapour Deposition (CVD), as it takes place at lower temperatures, without the formation of corrosive gaseous products that might leave impurities on the deposited film. Additionally, the deposition rate in EBPVD is relatively high (ranging from a few to a few hundreds of nm per minute), as is the material utilization efficiency that EBPVD offers relative to other deposition methods.

An Edwards AUTO306 EBPVD system was used for the work presented here. An acoustic crystal monitor was fitted to the system as shown in **Fig. 3.11**, and was connected to an Edwards film thickness monitor for controlling the thickness of deposited material. Prior to each deposition cycle, the base pressure of the chamber was typically below $1x10^{-6}$ mBar. The typical

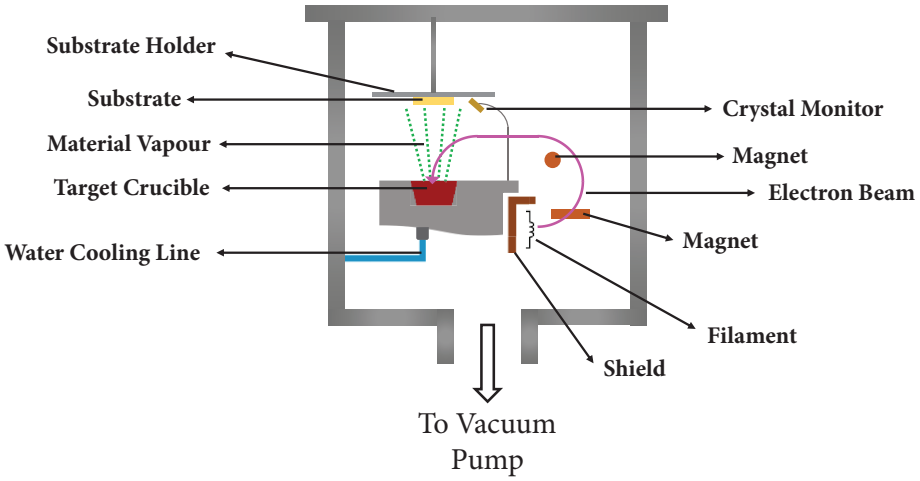

Figure 3.11 Schematic representation of a EBPVD chamber.

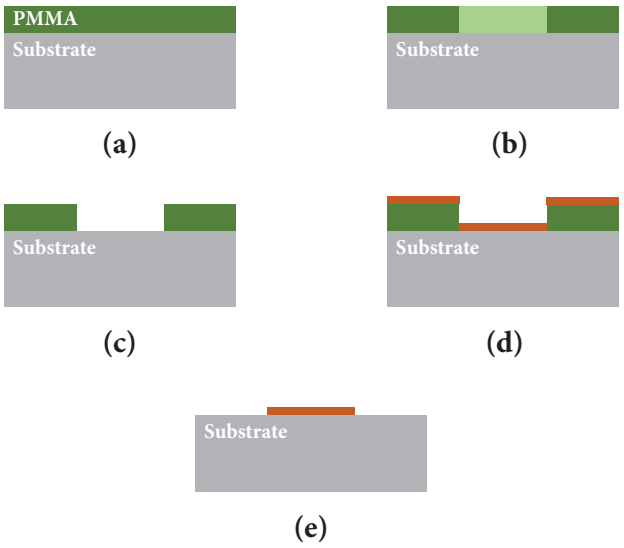

Figure 3.12 Lift-off process flow. (a) Substrate with PMMA resist on it. (b) The desired design is exposed on the resist via photolithography or e-beam lithography. (c) Substrate after development in a 3:7 mixture of H_2O and IPA. The exposed areas have been removed. (b) A film of the desired material is deposited on the entire surface of the substrate. (e) The substrate is immersed in Acetone, which strips it from the resist and the deposited material from the undesired areas.

deposition rate for the system used was between 0.1 and 0.3 nm/sec, with the average filament current varying depending on the target material. The EBPVD system was used for the deposition of Anti-Reflection coatings (mainly MgF_2 based) and for the deposition of metal contacts (based on Cr, Ni or Al, depending on the application).

For the formation of metal contacts, EBPVD was used as a step of the lift-off procedure. The lift-off process is a simple method of producing patterns of a target material on selected areas

of a substrate, and is commonly used for the formation of electrical contacts. During my work, for the lift-off process, the substrate was spun with a 500 nm thick layer of PMMA (positive resist) and was baked at 180 ^{O}C for 10 minutes. The desired design was patterned on the resist using photolithography or e-beam lithography and then developing in a mixture of de-ionized H_2O and IPA (3 parts de-ionized H_2O and 7 parts of IPA). The desired material was then deposited on the substrate using EBPVD. After the deposition process, the substrate was immersed in Acetone, which dissolves PMMA. The resist was stripped, removing with it the deposited material from the undesired parts. The flow of the lift-off process is depicted in **Fig. 3.12**.

3.7.2 Electron-Beam Physical Vapour Deposition for Anti-Reflection Coatings

The reflectivity at the interface between two dielectrics with refractive indices n_1 and n_2 ($n_1 < n_2$, as in **Fig. 3.13a**) is given by 'Fresnel's formula'

$$R = \left(\frac{n_2-n_1}{n_1+n_2}\right)^2. \quad \textbf{(3.2)}$$

An Antireflective or Anti-Reflection (AR) coating is a type of optical coating that can be applied to the surface of optical elements (e.g. lenses, waveguides, etc) to reduce back-reflections. The principle of the function of AR coatings is based on the destructive interference of the beams reflected off the different interfaces of the considered system. More specifically, considering the case of a single layer AR coating under normal incidence (**Fig. 3.13b**), the AR coating reduces the back-reflection of the input beam by creating a π phase difference between beam A (reflected off the interface of the dielectrics with indices n_1 and n_2) and beam B (reflected off the interface of the dielectrics with indices n_2 and n_3), which consequently interfere destructively. The reflectivity of both interfaces should be the same, which in Fresnel term implies that (following the notation of **Fig. 3.13b**)

$$\left(\frac{n_2-n_1}{n_1+n_2}\right)^2 = \left(\frac{n_3-n_2}{n_2+n_3}\right)^2 \quad \textbf{(3.3)}$$

The ideal refractive index for a single layer AR coating can be found from Eq. 3.3 to be $n_2 = \sqrt{n_1\, n_3}$. Considering that the phase change of a beam with vacuum wavelength λ_0 that propagates for distance d in a material with index n is $\delta = \frac{4\pi}{\lambda_0} nd\cos\theta$, and knowing that a phase change of π is desired during the round-trip propagation of the input beam in the AR film, it is apparent that the thickness of the AR layer must be $d_{AR} = \frac{\lambda_0}{4n_2}$ (for θ=0^o).

A single layer AR coating can eliminate the reflections at only one wavelength. However, multiple-layer AR coatings can supress back-reflections over a larger range of the wavelength spectrum (the bandwidth increases with the number of layers). A two-layer AR coating can be seen in **Fig. 3.13c**. The working principle is still based on destructive interference between successive reflected beams. For example, for the double-layer AR coating shown in **Fig. 3.13c**, there should be a π phase shift between the reflected beams A and B, and between the reflected beams B and C. It can be easily found then – similarly to the case with a single layer, and taking into account the π phase change that is picked up by a beam when it propagates from one material

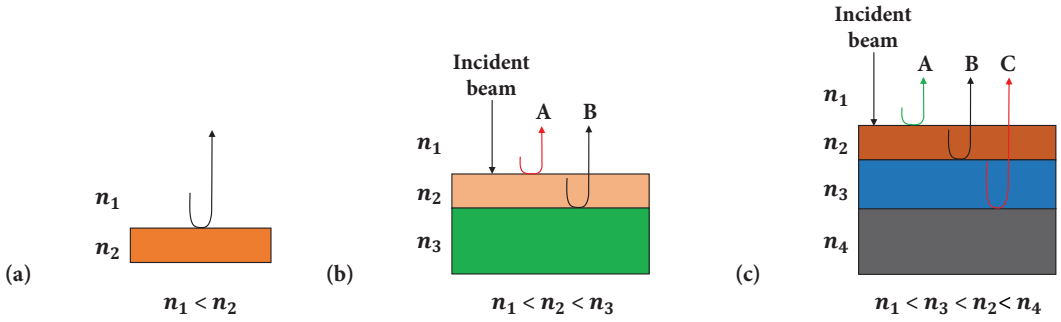

Figure 3.13 (a) Reflection (under normal incidence) between two dielectrics with refractive indices n_1 and n_2 ($n_1 < n_2$). (b) Reflection (under normal incidence) of a single beam at dielectric (refractive index n_3) with AR coating (refractive index n_2). (c) Reflection (under normal incidence) of a single beam at dielectric (refractive index n_4) with a two-layered AR coating (with layer indices n_2 and n_3).

to another with higher refractive index – that the thickness of both layers should be $\frac{\lambda_0}{4n_{layer}}$, where n_{layer} is the refractive index of the layer considered and λ_0 the considered vacuum wavelength. For a two-layer coating the refractive indices are related by $\frac{n_1^2 n_4}{n_3^2} = n_1$ (following the notation of **Fig. 3.13c**), which stems from an extended version of **Eq. 3.3**. Analogously, following the same principles, the thicknesses and refractive indices for the layers of n-layered AR coatings (n = 3, 4, 5, …) can be calculated.

As the minimization of back-reflections at the input and output of the waveguides used during the work described here was of major importance, AR coatings were used extensively. The considered waveguides were typically made of SU8 (n = 1.58), Silicon (n = 3.47) or Si_3N_4 (n = 1.85-2.10)[4] and the input and output interfaces were always between them and air. Even though the calculated optimal AR coating thickness is different for each of the considered materials (e.g. n_{opt1} = 1.25 for the air-SU8 interface and n_{opt2} = 1.86 for the air-Silicon interface), MgF_2 (with refractive index n ~ 1.37) was used for AR coatings on all of them, as it is the closest material with good physical properties for a coating. MgF_2 was deposited on the facets of the used waveguides using EBVPD (as described in Section 3.7.1) and the thickness of the coating was determined from the $\frac{\lambda_0}{4n_{MgF_2}}$ rule (with λ_0 = 1550 nm and n_{MgF2} = 1.37 – normal incidence was assumed). Single layer coatings were used for simplicity and for practical reasons (the deposition quality of the materials with a refractive index suitable for double-layer AR coatings available for the used EBVPD system was not optimal). Indicatively, **Fig. 3.14a** and **3.14b** show the reflectivity off the air-SU8 interface (beam incident on SU8 with n = 1.58 from air at an angle θ=0°) and the suppression that can be achieved by an ideal AR coating (n = 1.25) with $\frac{1550}{4 \cdot 1.25} = 310$ nm thickness and with a MgF_2 AR coating (n = 1.37) with $\frac{1550}{4 \cdot 1.37} = 282$ nm thickness. The results were calculated using the transfer matrix approach. Respectively, **Fig. 3.14c** presents the experimental transmission spectra (under normal incidence from air) of the same single-mode SU8 waveguide

[4] The refractive index values given here are for λ ~ 1.55 μm.

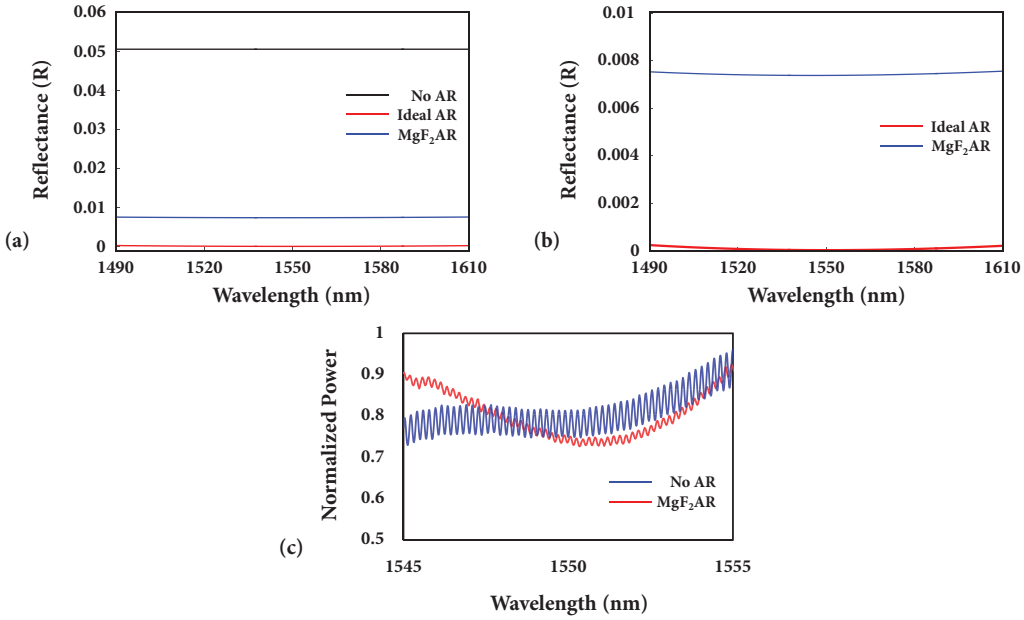

Figure 3.14 Reflectivity as a function of wavelength from an air (n = 1)/ SU8 (n = 1.58) facet (a) without coating (black line), with hypothetical ideal AR coating (n = 1.25) of 310 nm (blue line), with MgF_2 (n = 1.37) AR coating of 282 nm. (b) Close-up comparison of the performance of ideal AR coating (blue line) and MgF_2 AR coating on an air/SU8 interface (the specifications are the same as in (a)). (c) Experimental transmission of a single-mode SU8 waveguide on SiO_2 substrate without AR coating (blue line) and with a MgF_2 AR coating of ~ 282 nm on both facets (red line). Normal incidence of the input from air is considered.

on SiO_2 substrate prior to and after the deposition of a MgF_2 AR coating with thickness of ~280 nm on both of its facets. A suppression of the power reflectance of each facet by a factor of ~4 is observed (by evaluation of the fringe reflectivity of the transmission spectra with and without the AR coating)[5].

3.8 Conclusion

In this chapter, I have presented the main fabrication processes and tools that were used to fabricate the samples used for the work described in this thesis. A more detailed description of the parameters for each type of sample is given in the respective chapter.

[5] Following the previously used transfer matrix approach, an initial facet (air-SU8 interface) reflectivity of 5.4% can be estimated, corresponding to a supressed facet reflectivity of <1.4% after the deposition of AR coatings.

References

[1] K. Welna, S. L. Portalupi, M. Galli, L. O'Faolain and T. F. Krauss, "Novel Dispersion-Adapted Photonic Crystal Cavity with Improved Disorder Stability," *IEEE Journal of Quantum Electronics,* vol. 48, no. 9, pp. 1177-1182, SEP 2012.

[2] M. A. McCord and M. J. Rooks, "E-Beam Lithography," in *SPIE Handbook of Microlithography, Micromachining and Microfabrication, Vol. 1: Microlithography*, SPIE Publishing, 1997.

[3] N. William Parker, A. D. Brodie and J. H. McCoy, "High-throughput NGL electron-beam direct-write lithography system," in *Proc. SPIE 3997, Emerging Lithographic Technologies IV*, Santa Clara, CA, 2000.

[4] D. F. Kyser and N. S. Viswanathan, "Monte Carlo simulation of spatially distributed beams in electron-beam lithography," *Journal of Vacuum Science and Technology,* vol. 12, no. 6, pp. 1305-1308, DEC 1975.

[5] R. Wüest, "Proximity-effect induced density limitations for electron-beam patterned planar photonic nanomaterials," *Photonics and Nanostructures - Fundamentals and Applications,* vol. 7, no. 4, pp. 212-219, DEC 2009.

[6] H. Jansen, M. de Boer, R. Legtenberg and M. Elwenspoek, "The black silicon method: a universal method for determining the parameter setting of a fluorine-based reactive ion etcher in deep silicon trench etching with profile control," *Journal of Micromechanics and Microengineering,* vol. 5, no. 2, pp. 115-120, DEC 1994.

Chapter 4

Long External Cavity Laser Configuration

4.1 Introduction

Light sources have always been indispensable components of all types of optical transmitters, as they are necessary for the electrical-to-optical (E-O) signal conversion. With Silicon photonic technologies increasingly penetrating the datacommunication scene, the pursuit of an on-chip, silicon-compatible light source intensifies. As the future optical interconnect bandwidth demands are expected to be met through the channel scalability and parallelism offered by Wavelength Division Multiplexing (WDM), the ideal on-chip source is required to exhibit high power efficiency, a wide operating temperature range (up to 80 ^{o}C), precise wavelength registration, and small footprint for denser integration.

However, despite the several attempts [1, 2, 3], an efficient, electrically pumped laser at approximately 1310 or 1550 nm, has not yet been built on Silicon or any other Group IV element, owing to the low emission efficiency of these materials (result of their indirect bandgap). In this way, the use of III-V elements as gain materials is currently rendered imperative. Aiming at overcoming the coupling and packaging-cost problems of off-chip lasers, several solutions have been suggested for the combination of III-V elements with Silicon in order to obtain an on-chip laser cavity, as discussed in Chapter 1. Some of the most prominent approaches are the heterogeneous integration of III-V materials on Silicon by direct [4, 5, 6] or indirect bonding [7, 8, 9], the hetero-epitaxial growth of III-V on Silicon [10, 11, 12], and the formation of External Cavity (EC) lasers consisting of an intact III-V gain medium and a Silicon-based external reflector [13, 14]. EC lasers have attracted significant attention, as they exhibit better carrier injection efficiency and thermal impedance than heterogeneously integrated or hetero-epitaxially grown configurations, with comparable III/V-to-Silicon coupling losses [15]. Additionally, EC architectures allow the independent design, fabrication and optimization of the active medium and of the silicon circuits, the process flow of which is not affected by the integration of the III-V material.

In this chapter, I present a hybrid III-V/Silicon external cavity laser design that utilizes as an external resonant reflector the vertically coupled bus waveguide-photonic crystal cavity system that was shown in Section 2.4. The concept of using grating cavity resonant reflectors has been introduced for heterogeneously integrated lasers in [16, 17]. The attraction of photonic crystal cavities is their high Q-factor/V ratio, which indicates the possibility of achieving narrow-linewidth resonances with large Free Spectral Range (FSR > 100nm demonstrated in [18] and [19]) in small footprints. In this way high integration density and channel scalability are feasible, while the narrow-linewidth of the PhC cavity resonance provides a mechanism towards

single-mode lasing – all being features greatly desired in WDM interconnects. Furthermore, the large cross-sectional area of the bus waveguide on the external reflector (due to its low refractive index, as seen in Sections 2.4.2 and 2.4.3) enables efficient coupling between the active and the passive parts, even without the need of mode size converters.

The devices used for the experiments in this chapter were designed and fabricated by myself in the University of St Andrews. The experiments presented in this chapter were conducted by myself in the University of St Andrews, and the related material has been published in [20] and [21].

4.2 The Laser Cavity

The primary focus of the project was the demonstration of the functionality of the proposed laser configuration. In order to achieve that, a commercially available, packaged fiber-pigtailed SOA (Kamelian OPA-20-N-C-FA with minimum fiber-to-fiber gain of 20 dB for wavelengths around 1550nm) was employed as the gain medium. **Fig. 4.1** gives a schematic side view of the examined EC laser cavity. A pair of compact aspheric lenses (Newport 5722-C, diameter: 6.3mm, focal length: 4.5 mm, working distance: 2.9mm, AR coated for the wavelength range of 1000 to 1600 nm) were used to couple the light from the SOA to the external reflector, by first collimating (lens L1) and then focusing it (lens L2) on the bus waveguide of the reflector chip (marked with S) that played the role of one of the mirrors of the laser cavity (R_2). Optical feedback at the other end of the cavity was provided by a simple broadband fiber optic reflector, with power reflectivity $R_1 \sim 0.95$.

For the external reflector chip, a Dispersion Adapted (DA) photonic crystal cavity [22] was vertically coupled to a polymer SU8 ($n \approx 1.59$) bus waveguide, as described in Section 2.4.3. Although the DA design exhibits a relatively small Free Spectral Range (FSR), it was chosen as it is simple to fabricate and highly resilient to disorder. Moreover, its rich vertical k-space distribution enables the use of dielectrics with lower refractive index (e.g. polymers such as SU8) for the bus waveguide, allowing for larger cross-sectional areas. The DA cavity was fabricated on

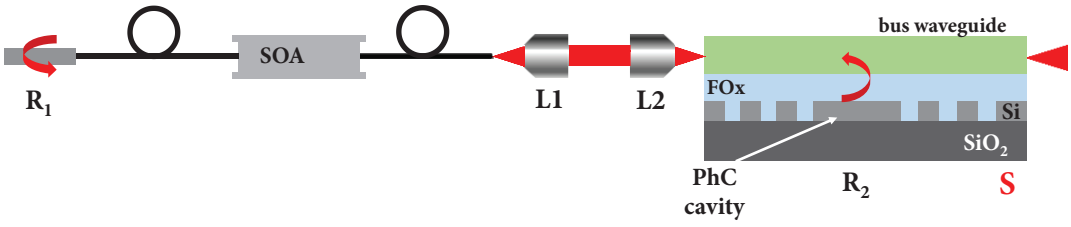

Figure 4.1 Schematic representation of the examined external cavity laser architecture and operation. The laser comprises a packaged, fiber-pigtailed Semiconductor Optical Amplifier (SOA) and an external reflector chip (S with reflectance R_2) that consists of a bus waveguide vertically coupled to a Silicon photonic crystal cavity. The second mirror is a fiber optic reflector (R_1). The output of the SOA is coupled to the bus waveguide by a pair of lenses (L1 and L2).

a SOITEC 220 nm Silicon-On-Insulator (SOI) platform by electron-beam lithography Reactive Ion Etching (RIE). Flowable oxide (FOx-15 by Dow Corning) was used for the top cladding layer of the PhC cavity. The width of the bus waveguide was ~3 μm and its height ~2.1 μm, resulting in low coupling losses (<3 dB/facet). AR coatings were used on both facets of the waveguide to minimize back-reflections. The complete fabrication process and fabrication details can be found in Chapter 3.

Amplified spontaneous emission in the SOA generates a broad IR frequency spectrum, which is coupled to the SU8 waveguide. Light at frequencies matching the resonances of the Silicon photonic crystal cavity are coupled to it from the bus waveguide (as described in Section 2.4), and power builds up in the cavity. As seen in Section 2.4, the light that evanesces from the PhC cavity back to the bus waveguide couples to a forward propagating mode – destructively interfering with the light propagating in the waveguide – and to a backwards propagating mode, which acts as optical feedback to the SOA. Due to the resonant nature of the Silicon-based mirror, it provides a wavelength-selective reflection only at the frequencies that correspond to the resonances of the PhC cavity. In this way, a conventional laser cavity is formed between the PhC cavity and the fiber reflector only for those wavelengths.

4.3 Experimental Setup and Laser Characterization

During this project, the transmission of the photonic crystal cavity-based chips was measured prior to them being employed as reflectors. For this, an end-fire technique was used to couple light in and out of each device. A schematic of the passive optical setup is shown in **Fig. 4.2a**. For the transmission measurements, the output of a broadband Amplified Spontaneous Emission (ASE, emission span: 1520-1620 nm) source was launched in single-mode fiber (SMF) and fed to an aspheric lens (AL1). A polarizing beam-splitter (PBS) was used to filter out TM polarized light from the collimated output of AL1. The TE polarized beam was focused on the cleaved facet of one the bus waveguides on the silicon chip (S) using an aspheric lens (AL2). The transmitted light was collected at the other end of the waveguide by a collimating aspheric lens (AL3). The collimated output was then focused by an aspheric lens (AL4) on a SMF fiber connected to an InGaAs photodetector (PD) – the output of which was read on a digital sampling oscilloscope (DSO) – and an optical spectrum analyser (OSA – with a maximum resolution of 0.01 nm) for the spectral power distribution of the device under test (DUT) to be measured. An infrared camera (IRC) was used to assist the alignment of the output of AL2 with the waveguides on the chip. The sensitivity of the camera spanned from visible to infrared frequencies, allowing the simultaneous observation of the chip and its features, and of the infrared light (from the ASE source) transmitted through the bus waveguides.

For the laser characterization, a setup broadly similar to the passive optical setup described above was used. A schematic of the laser characterization setup can be seen in **Fig. 4.2b**. The output of the laser cavity (as this was described in Section 4.2) was collected at the end of the SU8 waveguide of the employed resonant reflector device using a pair of aspheric lenses (AL3 for collimating and AL4 for focusing) and was launched in a SMF that was connected to the InGaAs

photodetector (and DSO) and the optical spectrum analyser (OSA)[1]. Lasing experiments for several PhC cavity devices were conducted at room temperature and emitted laser spectra were taken for different values of the drive current of the SOA. The measurements were limited by the resolution of the employed OSA (0.01nm).

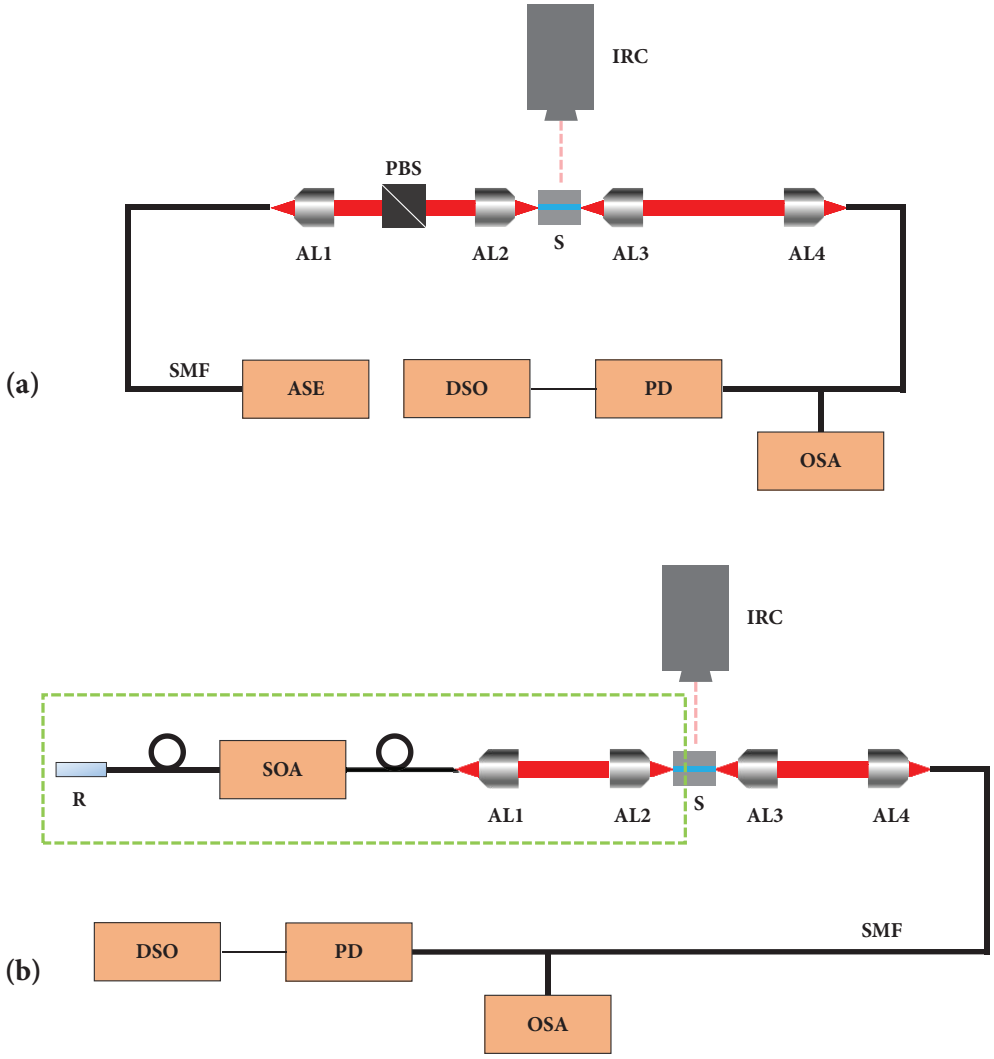

Figure 4.2 (a) Experimental setup for passive optical (transmission) measurements. (b) Experimental (characterization) setup of the proposed external cavity laser, comprising a fiber-pigtailed semiconductor optical amplifier (SOA). The dashed light green frame highlights the EC laser cavity. AL (1-4): aspheric lenses, PBS: polarizing beam splitter, S: silicon chip/photonic crystal cavity based reflector, R: fiber optic reflector, ASE: amplified spontaneous emission broadband source, DSO: digital sampling oscilloscope, PD: photodetector, OSA: optical spectrum analyser, SMF: single-mode fiber.

[1] For completeness, the laser emission was also collected at the end of the SU8 bus waveguide using a single-mode lensed fiber (that was then connected to the InGaAs PD and the OSA). The observed results were the same in both cases (lensed fiber and pair of aspheric lenses).

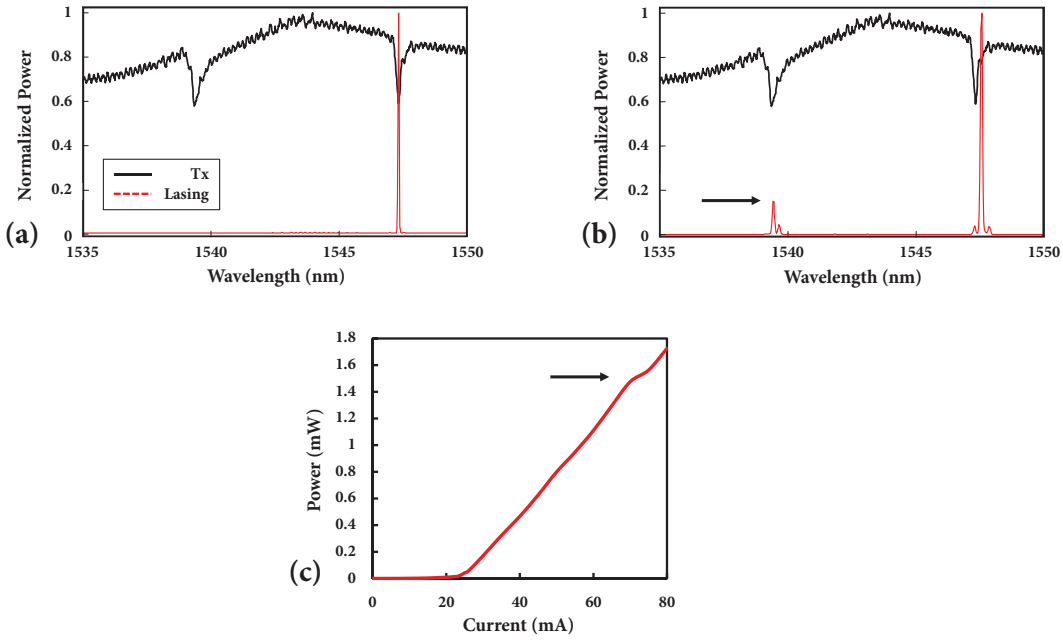

Figure 4.3 Characterization of external cavity laser with resonant external reflector comprising a DA PhC cavity with lattice constant a = 388 nm and fill factor r/a = 0.28. (a) Lasing spectrum (dashed red/Lasing) showing single-mode operation at 40 mA overlaid with the transmission spectrum of the aforementioned PhC cavity-based device (solid black/Tx). (b) Lasing spectrum at 80 mA overlaid with the transmission spectrum of (a). (c) L-I curve at room temperature. The arrows indicate a kink in the L-I curve (c), due to the appearance of a second lasing mode caused by a higher-order PhC cavity resonance, shown in (b).

Fig. 4.3c shows the light versus current (LI) curve for a laser cavity comprising a DA cavity with lattice constant a = 388 nm and fill factor r/a = 0.28 (r being the radius of a hole). The output power was measured with a Thorlabs digital power-meter after AL3 (or at the end of the lensed fiber, respectively). The threshold current for the examined device was found to be 23.6 mA (at an emitted wavelength of 1547.32 nm) and the experimental slope efficiency was η_s = 0.0324 mW/mA. Based on [23], a PhC cavity mirror reflectivity of ~40% and intra-cavity losses of ~7.7 dB (primarily due to coupling and mirror losses) were estimated from the experimental threshold gain and slope efficiency. Owing to the large length of the laser cavity (which ranged from 5 to 8 m, depending on the length of the fiber patchcords that were used), the longitudinal mode spacing is extremely narrow (<20 pm), effectively resulting in a longitudinal mode continuum. The emitted wavelength and the laser linewidth are therefore determined exclusively by the resonance characteristics of the PhC cavity (according to Section 2.5).

The kink observed in the LI curve (marked with an arrow in **Fig. 4.3c**) is caused by the appearance of a second lasing mode: as previously mentioned, the relatively small FSR of DA cavities results in multimodal behaviour. As cavity modes represent the various energy distributions in the cavity, different modes exhibit different coupling rates from and to bus waveguide and consequently different power reflection (R) and transmission (T) coefficients (according to Section 2.4). Each DA cavity mode can thus act as an individual reflector, resulting in the potential formation of more than one laser cavities that share the same gain medium. Each

of these laser cavities/modes has its own lasing characteristics (threshold, efficiencies, etc) that depend mainly on the power reflection coefficient of the corresponding DA mode. For the DUT, the lasing threshold condition for the higher-order DA cavity mode is satisfied at ~68 mA. The single-mode operation of the studied laser for current values below the threshold of the second lasing mode can be seen in **Fig. 4.3a**, which shows the lasing spectrum at 40 mA. The existence of the second lasing mode can be seen in **Fig. 4.3b**, showing the lasing spectrum at 80 mA. Both lasing spectra are overlaid with the transmission spectrum of the employed PhC cavity-based reflector[2]. It is apparent that each laser mode corresponds to a PhC cavity mode, proving that the emitted wavelength in the suggested architecture is determined by the resonances of the PhC cavity. The small offset of the lasing peaks from the center of the resonances in the transmission spectrum observed in **Fig. 4.3b**, is a result of the red-shift of the PhC cavity resonances (and consequently of the resonant reflection peaks) due to larger intra-cavity powers at higher drive currents.

4.4 Lithographic tuning

Precise control of the emitted wavelength is a key-feature of on-chip lasers for WDM optical links. Aiming at examining the suitability of the proposed external cavity configuration for such applications, lithographic control of its lasing wavelength was demonstrated by studying laser cavities comprising resonant reflectors with different PhC cavity resonances. The cavity resonances were tuned by varying the position of the four inner holes of the DA cavity design [22]. The considered holes were shifted between 36 and 44 nm outwards (in steps of 2 nm), with respect to the hole position in a W1 waveguide configuration, as shown in the inset of **Fig. 4.4**. Other than the aforementioned variation, the resonant reflector devices were identical, with lattice constant α = 388 nm and fill factor r/α = 0.28.

Fig. 4.4 shows lasing spectra (in room temperature) from laser cavities utilizing different external resonant reflector devices, at a drive current of 40 mA. The change in the emitted wavelength from the first lasing mode of each device can be observed. The non-equidistant and non-linear change is due to the combination of fabrication disorder and of the fact that the first lasing mode in each device did not always correspond to the same resonance order of the PhC cavity. The lasing characteristics (i.e. differential quantum efficiency and slope efficiency) of each laser cavity varied, depending on the power reflectance (R) of each resonant Si mirror device; the latter is basically determined by the coupling rate between the SU8 bus waveguide and the PhC cavity, which varied due to fabrication imperfections. The Side-Mode Suppression Ratio (SMSR) was in every case >25 dB. Given the tight longitudinal mode spacing due to the large length of the laser cavity, the SMSR is limited by the relatively low value of the cross-correlation between the mirror loss α_m and the net propagation gain $\gamma_{xy} g - \alpha_i$ (according to Section 2.5).

[2] The same transmission spectrum is used in both **Fig. 4.3a** and **Fig. 4.3b** for simplicity.

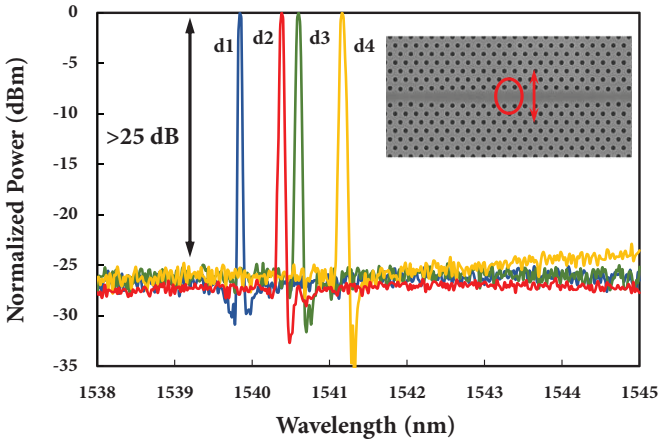

Figure 4.4 Lasing spectra for external cavity lasers utilizing resonant reflectors that comprise DA PhC cavities with different outward shifts of the two inner pairs of holes. Spectrum d1 (blue) corresponds to a shift of 36 nm with respect to the original hole position in a W1 waveguide, d2 (red) to a shift of 44 nm, d3 (green) to a shift of 40 nm and d4 (yellow) to a shift of 42 nm, respectively. The inset shows an SEM image of a DA PhC cavity. Tuning of the position of the four innermost holes (in red circle) results in variation of the cavity resonances (and resonant reflections).

4.5 Discussion

To conclude, in this chapter I have presented the function of a hybrid external cavity laser architecture comprising a fiber pigtailed SOA with a fiber optic reflector and a Si resonant reflector based on a PhC cavity vertically coupled to a dielectric bus waveguide. The vertical coupling scheme provides a solution to the problematic interfacing of Silicon photonic crystal cavities, facilitating their use in practical WDM interconnect applications where small footprint, large FSR, precise wavelength control and the potential of low energy modulation (stemming from their ultra-high Q-factor/V ratio) are of utter importance. Additionally, the low index of the bus waveguide allows for larger mode profiles and consequently more efficient coupling to the SOA or other relevant components (e.g. lensed fibers, other waveguides, etc).

An external cavity (EC) configuration was chosen as it allows for independent fabrication and optimization of the active and the passive parts. As seen in Section 4.3, the large laser cavity length of the fiber-coupled arrangement examined in this chapter corresponds to a sub-pm longitudinal mode spacing. Consequently, the emitted lasing wavelength and linewidth are determined exclusively by the resonances of the PhC cavity in the external reflector, and the proposed scheme can operate for a wide continuous range of laser cavity lengths, exhibiting high resilience to cavity length variations. In this way, the spatial separation of the active medium from the Silicon reflector is possible by simply using adequately long fiber patchcords. As the power consumption of the gain chip does not add to the on- chip heat dissipation in such a scheme, the overall thermal stability of the device is improved, which is a highly-desired feature in many Silicon Photonics applications (e.g. sensing, optical interconnects, etc). Nonetheless, the emitted

wavelength is still controlled by the on-chip elements (i.e. the PhC cavity) and thus the functionality remains on Silicon – a fact that, combined with the employed vertical coupling approach that maximises the area available for electronic circuitry, is an advantage for CMOS integration.

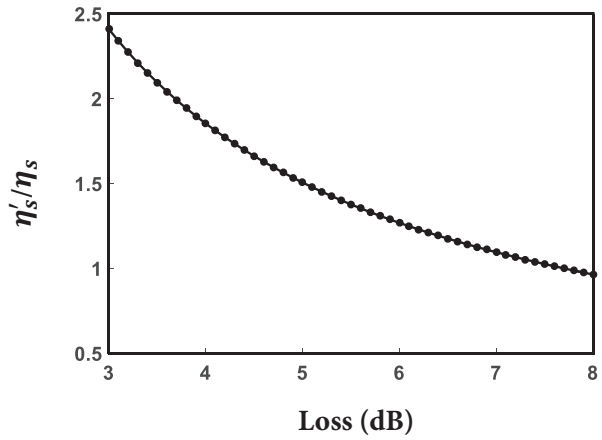

Figure 4.5 Ratio of calculated slope efficiency (η_s') over experimentally observed slope efficiency (η_s = 0.0324 mW/mA) as a function of laser cavity losses.

A lasing threshold of 23.6 mA and a slope efficiency of η_s = 0.0324 mW/mA were demonstrated for mW-lever output powers at 1547.32 nm. An improvement of the slope efficiency can be achieved by reducing the coupling losses in the laser configuration. **Fig. 4.5** shows the ratio of the slope efficiency calculated according to Section 2.5 (η_S') with respect to the experimentally observed slope efficiency (η_s) as a function of laser cavity losses (assuming that the mirror reflectivies are the ones considered in the experiments presented in this chapter and are kept constant) . It can be seen that a reduction of the intra-cavity losses down to 3 dB can lead to an estimated improvement of the slope efficiency by a factor of ~2.5.

The lithographic tuning of the emitted wavelength (with SMSR >25 dB) reveals a unique level of wavelength control in hybrid III-V/Silicon EC lasers, by simply shifting the position of four sites (holes) of the photonic crystal lattice in steps of 2 nm. The use of a PhC cavity-based resonant reflector is particularly relevant as, apart from the precise wavelength registration (stemming from the fact that the PhC cavity provides a mode selection mechanism, as described in Section 2.5) and the ultra-small Silicon footprint, such a reflector offers the potential of dynamically tuning the emitted wavelength of the laser by electro-optic modulation of the PhC cavity resonances, at ultra-low power budgets [24]. During this project, a combination of SU8 polymer waveguides and Dispersion Adapted (DA) PhC cavities was used for technological convenience (no additional deposition steps, easy fabrication, high tolerance to disorder). However, the possibility of using other low-index materials (e.g. Si_3N_4) has been demonstrated [25], along with the potential of employing different PhC cavity designs (e.g. the use of the line defect modulated cavity design of [18] shown in [26]). By utilizing a single-mode PhC cavity design in the suggested laser configuration, the appearance of multiple lasing modes from one device can be avoided, enabling tighter frequency channel spacing in WDM applications.

The extension of the working principle discussed here to a compact butt-coupled configuration (similar to the ones shown in [13], [14] and [15]) that can exhibit lower intra-cavity losses – and consequently lower threshold current and higher SMSR – is presented in Chapter 5. The incorporation of wavelength modulation functionality in the proposed architecture, as well as its further potential, are discussed in Chapter 6.

References

[1] H. Rong, R. Jones, A. Liu, O. Cohen, D. Hak, A. Fang and M. Paniccia, "A Continuous-Wave Raman Silicon Laser," *Nature,* vol. 433, pp. 725-728, Jan 2005.

[2] J. Liu, X. Sun, R. Camacho-Aguilera, L. C. Kimerling and J. Michel, "Ge-on-Si Laser operating at room temperature," *Optics Letters,* vol. 35, no. 5, pp. 679-681, MAR 2010.

[3] S. Wirths, R. Geiger, N. von der Driesch, G. Mussler, T. Stoica, S. Mantl, Z. Ikonic, M. Luysberg, S. Chiussi, J. M. Hartmann, H. Sigg, J. Faist, D. Buca and D. Grützmacher, "Lasing in direct-bandgap GeSn alloy grown on Si," *Nature Photonics,* vol. 9, pp. 88-92, JAN 2015.

[4] H. Park, A. W. Fang, S. Kodama and J. E. Bowers, "Hybrid silicon evanescent laser fabricated with a silicon waveguide and III-V offset quantum wells," *Optics Express,* vol. 13, no. 23, pp. 9460-9464, NOV 2005.

[5] X. Sun, A. Zadok, M. J. Shearn, K. A. Diest, A. Ghaffari, H. A. Atwater, A. Scherer and A. Yariv, "Electrically pumped hybrid evanescent Si/InGaAsP lasers," *Optics Letters,* vol. 34, no. 9, pp. 1345-1347, MAY 2009.

[6] A. W. Fang, H. Park, O. Cohen, R. Jones, M. J. Paniccia and J. E. Bowers, "Electrically Pumped hybrid AlGaInAs-silicon evanescent laser," *Optics Express,* vol. 14, no. 20, pp. 9203-9210, OCT 2006.

[7] T. Hong, G.-Z. Ran, T. Cheng, J.-Q. Pan, W.-X. Chen, Y. Wang, Y.-B. Cheng, S. Liang, L.-J. Zhao, L.-Q. Yin, J.-H. Zhang, W. Wang and G.-G. Qin, "A Selective-Area Metal Bonding InGaAsP–Si Laser," *IEEE Photonics Technology Letters,* vol. 22, no. 15, pp. 1141-1143, AUG 2010.

[8] J. Van Campenhout, P. Rojo-Romeo, D. Van Thourhout, C. Seassal, P. Regreny, L. Di Cioccio, J.-M. Fedeli and R. Baets, "Thermal Characterization of Electrically Injected Thin-Film InGaAsP Microdisk Lasers on Si," *Journal of Lightwave Technology ,* vol. 25, no. 6, pp. 1543-1548, JUN 2007.

[9] S. Keyvaninia, M. Muneeb, S. Stanković, P. J. Van Veldhoven, D. Van Thourhout and G. Roelkens, "Ultra-thin DVS-BCB adhesive bonding of III-V wafers, dies and multiple dies to a patterned silicon-on-insulator substrate," *Optical Materials Express,* vol. 3, no. 1, pp. 35-46, JAN 2013.

[10] M. E. Groenert, C. W. Leitz, A. J. Pitera, V. Yang, H. Lee, R. J. Ram and E. A. Fitzgerald, "Monolithic integration of room-temperature cw GaAs/AlGaAs lasers on Si substrates via relaxed graded GeSi buffer layers," *Journal of Applied Physics,* vol. 93, no. 1, pp. 362-367, JAN 2013.

[11] Y. Chriqui, L. Largeau, G. Patriarche, G. Saint-Girons, S. Bouchoule, I. Sagnes, D. Bensahel, Y. Campidelli and O. Kermarrec, "Direct growth of GaAs-based structures on exactly (0 0 1)-oriented Ge/Si virtual substrates: reduction of the structural defect density and observation of electroluminescence at room temperature under CW electrical injection," *Journal of Crystal Growth,* vol. 265, no. 1-2, pp. 53-59, APR 2004.

[12] Z. Wang, C. Junesand, W. Metaferia, C. Hu, L. Wosinski and S. Lourdudoss, "III–Vs on Si for photonic applications—A monolithic approach," *Materials Science and Engineering: B,* vol. 177, no. 17, pp. 1551-1557, OCT 2012.

[13] A. Zilkie, P. Seddighian, B. J. Bijlani, W. Qian, D. C. Lee, S. Fatholoumi, J. Fong, R. Shafiiha, D. Feng, B. J. Luff, X. Zheng, J. E. Cunningham, A. V. Krishnamoorthy and M. Asghari, "Power-Efficient III-V/Silicon external cavity DBR lasers," *Optics Express,* vol. 20, no. 21, pp. 23456-23462, OCT 2012.

[14] S. Tanaka, S.-H. Jeong, S. Sekiguchi, T. Kurahashi, Y. Tanaka and K. Morito, "High-output power, single-wavelength silicon hybrid laser using precise flip-chip bonding technology," *Optics Express,* vol. 20, no. 27, pp. 28057-28069, DEC 2012.

[15] X. Zheng, S. Lin, Y. Luo, J. Yao, G. Li, S. S. Djordjevic, J.-H. Lee, H. D. Thacker, I. Shubin, K. Raj, J. E. Cunningham and A. V. Krishnamoorthy, "Efficient WDM Laser Sources Towards Terabyte/s Silicon Photonic Interconnects," *IEEE Journal of Lightwave Technology,* vol. 31, no. 24, pp. 4142-4154, DEC 2013.

[16] Y. De Koninck, F. Raineri, A. Bazin, R. Raj, G. Roelkens and R. Baets, "Experimental demonstration of a hybrid III–V-on-silicon microlaser based on resonant grating cavity mirrors," *Optics Letters,* vol. 38, no. 14, pp. 2496-2498, JUL 2013.

[17] Y. De Koninck, G. Roelkens and R. Baets, "Electrically pumped 1550 nm single mode III-V-on-silicon laser with resonant grating cavity mirrors," *Laser & Photonic Reviews,* vol. 9, no. 2, pp. L6-L10, JAN 2015.

[18] E. Kuramochi, M. Notomi, S. Mitsugi, A. Shinya, T. Tanabe and T. Watanabe, "Ultrahigh Q Photonic Crystal Nanocavities Realized by the Local Width Modulation of a Line Defect," *Applied Physics Letters,* vol. 88, p. 041112, 2006.

[19] B.-S. Song, T. Nagashima, T. Asano and S. Noda, "Resonant-Wavelength Control of Nanocavities by Nanometer-Scaled Adjustment of Two-Dimensional Photonic Crystal Slab Structures," *IEEE Photonics Technology Letters,* vol. 20, no. 7, pp. 532-534, APR 2008.

[20] A. Liles, K. Debnath and L. O'Faolain, "External-Cavity Hybrid Laser with Silicon Photonic Crystal Cavity-based Resonant Reflector," in *IEEE 12th International Conference on Group IV Photonics (GFP)*, Vancouver (CA), 2015.

[21] A. A. Liles, K. Debnath and L. O'Faolain, "Lithographic wavelength control of an external cavity laser with a silicon photonic crystal cavity-based resonant reflector," *Optics Letters,* vol. 41, no. 5, pp. 894-897, FEB 2016.

[22] K. Welna, S. L. Portalupi, M. Galli, L. O'Faolain and T. F. Krauss, "Novel Dispersion Adapted Photonic Crystal Cavity with Improved Disorder Stability," *IEEE Journal of Quantum Electronics,* vol. 48, no. 9, pp. 1177-1183, SEP 2012.

[23] L. A. Coldren and S. W. Corzine , Diode Lasers and Photonic Integrated Circuits, New York, NY: J. Wiley & Sons, 1995.

[24] K. Debnath, L. O'Faolain, F. Y. Gardes, A. Steffan, G. T. Reed and T. F. Krauss, "Cascaded modulator architecture for WDM applications," *Optics Express,* vol. 20, no. 25, pp. 27420-27428, DEC 2012.

[25] K. Debnath, K. Welna, M. Ferrera, K. Deasy, D. G. Lidzey and L. O'Faolain, "Highly efficient optical filter based on vertically coupled photonic crystal cavity and bus waveguide," *Optics Letters,* vol. 38, no. 2, pp. 154-156, 2013.

[26] K. Debnath , "PhD Thesis: Photonic Crystal Cavity Based Architecture for Optical Interconnects," School of Physics and Astronomy, University of St Adrews, St Andrews, APR 2013.

Chapter 5

Compact External Cavity Laser Configuration

5.1 Introduction

In Chapter 4, the concept and function were shown of an external cavity (EC) laser comprising a fiber-pigtailed Semiconductor Optical Amplifier (SOA) and a Photonic Crystal (PhC) cavity-based resonant external reflector. As efficient, cheap (leaders in the field appreciate that the desired power-budget price for optical interconnects is as low as $1/Gbps [1]) lasing with precisely controlled wavelength over a larger temperature range is required by the demanding operating environment and cost structure of datacenters, the extension of the functional concept presented in Chapter 4 to a smaller laser configuration was the main focus of this project.

In this chapter, I present a compact hybrid III-V/Silicon external cavity laser architecture that consists of a Reflective Semiconductor Optical Amplifier (RSOA) die butt-coupled to a Silicon-based external reflector with a dielectric bus waveguide vertically coupled to a PhC cavity (previously presented in Chapter 2 and used in Chapter 4), similar to the ones presented in [2], [3], [4] and [5]. The motivation behind employing a PhC cavity-based reflector and choosing an EC laser scheme has been previously discussed. Here, I will initially demonstrate the EC laser cavity architecture, along with some basic laser characterization. As the examined configuration is particularly relevant to datacommunication applications, the thermal stability of the laser, as well as the alignment tolerance between the passive and the active parts (important for on-chip integration) are also studied.

The devices used for all the experiments in this chapter were designed and fabricated by myself in the University of St Andrews. The experiments for Section 5.3.1 and Section 5.3.2 were conducted by myself in the University of St Andrews, and by myself and Andrei P. Bakoz (affiliations: Cork Institute of Technology (CIT), Tyndall National Institute and ITMO University) in Tyndall National Institute. The experimental data for Section 5.3.3 were collected by Andrei P. Bakoz in Tyndall National Institute. The material related to this chapter has been published in [6], [7], [8], [9] and [10].

5.2 The Laser Cavity

5.2.1 Design Description

For the formation of the EC laser configuration examined in this chapter, a RSOA die on mount was butt-coupled to the bus waveguide of the Silicon reflector chip that was described and used in Chapters 2 and 3, and 4, respectively (**Fig 5.1**). The gain chip was a 250-μm long InP ridge optical amplifier with AlGaInAS quaternary quantum wells (QW), mounted on a ceramic tile with its front end overhanging, provided by CST Global. The Al(3+) ions contained in the QWs increase the height of the energy potential of the wells, restricting the temperature-dependent carrier leakage and thus resulting in higher gain at elevated temperatures [11]. The back facet of the RSOA die was HR-coated with power reflectance R > 90%, while its front facet was coated with a multi-layer AR-coating to minimize back-reflections. For the Silicon-based external

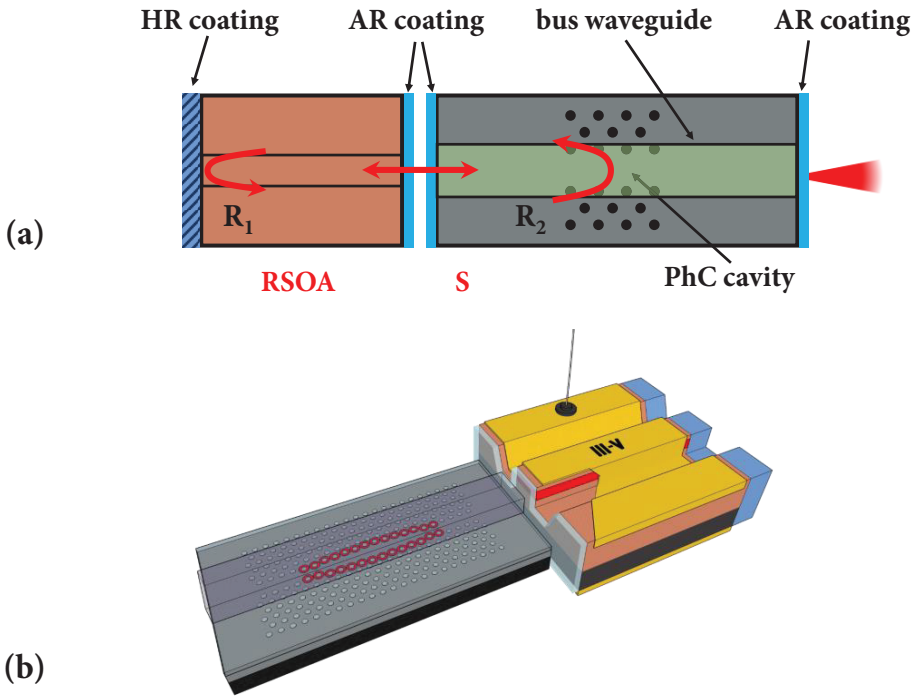

Figure 5.1 (a) Schematic representation of the compact external cavity laser configuration discussed in this chapter. The laser cavity is formed by butt-coupling a III-V-based Reflective Semiconductor Optical Amplifier (RSOA) to an external reflector chip (S), comprising a bus waveguide vertically coupled to a Silicon PhC cavity, that provides wavelength-selective optical feedback (R_2). The rear facet of the RSOA is HR-coated, acting as the second mirror of the laser cavity (R_1). AR-coatings are used on the front facet of the RSOA and on both facets of the Silicon chip to minimize back-reflections. (b) Three-dimensional representation of the examined compact external cavity laser configuration. The cut in the upper metal contact (yellow) of the RSOA chip reveals a ridge with a waveguiding QW structure (depicted in red). On the Silicon-based external reflector chip, the holes that define the PhC cavity are also marked with red (for consistency, a Dispersion Adapted design is considered here).

reflector chip, a polymer SU8 waveguide vertically coupled to a Dispersion Adapted (DA) photonic crystal cavity [12] was used in this case, too. The width and height of the polymer bus waveguide were again ~3 μm and ~2.1μm, respectively. Single-layer MgF_2 AR coatings were used on both facets of the waveguide. The complete fabrication process and details can be found in Chapter 3 and Section 4.2.

5.2.2 Design Considerations

The lasing mechanism is the same as for the fiber-pigtailed design and is presented in Section 4.2. The main focus of this configuration is the reduction of the footprint of the device (and thus of its cost), without compromising its performance. The use of a highly-optimized RSOA chip allows for the reduction of the length of the gain medium by more than a factor of two compared to competing approaches [2, 3, 13], resulting in very cost-effective use of III-V materials. Additionally, the use of PhC cavities on the external reflector end enables the reduction of the Silicon footprint to areas as small as 100 μm^2, further reducing the device cost by increasing the density of integration. Moreover, the large FSR that PhC cavities exhibit, offers the potential for increasing the number of employable frequency channels in a given frequency band. The aforementioned reasons make the examined architecture of particular interest to on-chip and chip-scale WDM networks.

Based on the discussion in Chapter 1, single-mode operation is crucial for WDM datacommunication links. High longitudinal mode selectivity and large side-mode suppression ratio (SMSR) are, therefore, features that are greatly desirable in the laser device studied in this chapter. As explained in Section 2.5, the use of a narrowband wavelength-selective external reflector provides an inherent route towards the selection of a single longitudinal mode: for a specific active part length (here the length of the RSOA die, i.e. 250 μm), an appropriate choice of the length of the passive section can result in a longitudinal mode spacing in the laser cavity (given by Eq. 2.19) large enough to ensure that only one longitudinal mode will overlap with the narrow linewidth of the reflection (corresponding to the situation depicted in **Fig. 2.11**). The combination of this fact with the large FSR of PhC cavities provides a route to single mode operation[1] and simultaneously to the suppression of adjacent side-modes. For the configuration considered in this chapter, passive section lengths[2] of 3 and 4 mm correspond to a longitudinal mode spacing (according to Eq. 2.19) of 0.22 and 0.17 nm, respectively, which is larger than or similar to the linewidth of the PhC cavities employed in this project (typically between 0.10 and 0.20 nm) and therefore adequate to provide single-mode lasing.

[1] The large FSR of PhC cavities implies the absence of reflections due to cavity resonances in the immediate spectral vicinity (and thus low lasing mode competition).

[2] The length of the passive section is not the physical length of the Silicon photonic reflector chip, but the length that accounts for the phase contribution of the passive section of the laser cavity and the wavelength-dependent phase contribution by the PhC cavity in the reflector. It can be approximated by the distance of the PhC cavity on the reflector chip from the facet closer to the RSOA die.

An effect with detrimental repercussions for the single-mode selectivity of the suggested EC laser configuration that had to be considered during this project, was the back-reflections from the chip facets. According to Section 2.5, the longitudinal mode selectivity in a laser cavity is determined by the combination of the mirror loss α_m with the net propagation gain $\gamma_{xy} g - \alpha_i$ that results in a single net gain maximum (notation following Chapter 2). In the laser architecture presented here, the non-zero reflectivity of the non HR-coated RSOA die facet and of both the Silicon chip facets (**Fig. 5.1a**) can lead to the formation of parasitic cavities and consequently the appearance of Fabry-Perot fringes on the gain and the reflection (i.e. mirror loss) spectra, respectively. Since the mode selection is dependent on the extremum of the product of the two aforementioned spectra, their 'modulation' can result in a net gain maximum that assists the lasing of one of the parasitic longitudinal modes instead of the longitudinal mode defined by the resonant reflector in the EC laser. An exaggerated schematic representation of the concept is depicted in **Fig. 5.2a**: the net gain ($\gamma_{xy} g - \alpha_i$) ripple and spectral distribution, combined with the modulation in the mirror loss (α_m) produce a net gain maximum that benefits the selection of the (parasitic) longitudinal mode shown in red, over the EC laser cavity longitudinal mode shown in black.

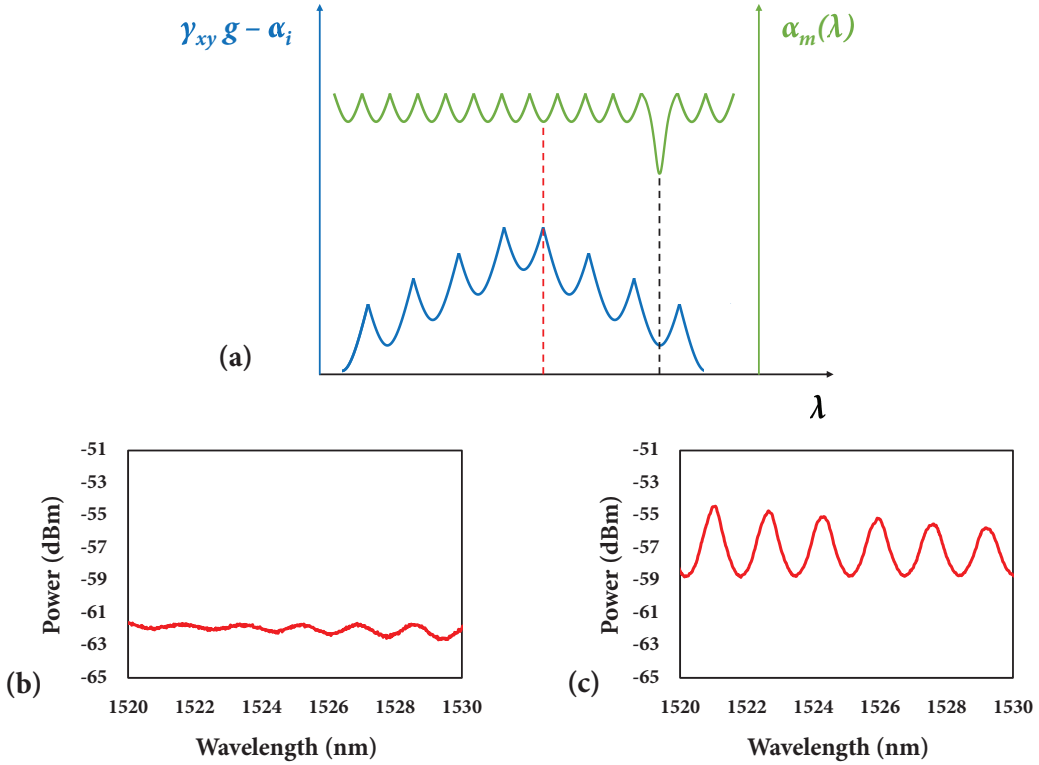

Figure 5.2 (a) Schematic illustration of net propagation gain $\gamma_{xy} g - \alpha_i$, (blue) and the net resonant mirror loss α_m (green), as a function of wavelength, for an EC laser with a vertically coupled bus wavguide-PhC cavity external reflector. The ripple/modulation of the two spectra caused by non-zero reflectivity of the front RSOA facet and of both facets of the bus waveguide on the silicon chip, respectively, can result in a net gain maximum that assists the lasing of one of the parasitic longitudinal modes (marked in red) instead of the longitudinal mode defined by resonance of the PhC cavity (marked in black). Transmission spectra at 60 mA of two RSOA dies with a gain ripple extinction ratio of (b) ~1 dB, and (c) >4 dB.

The impact of the above effect can be significantly diminished by eliminating the gain and reflection spectra modulation/ripple. It can be easily understood therefore that use of AR coatings (on both the RSOA and the Silicon chip) is of crucial importance for the single-mode selectivity and the side-mode suppression in the laser configuration of this chapter. Indeed, as previously shown in Section 3.7.2, the use of single-layer MgF_2 AR coatings on the facets of the SU8 waveguide on the Silicon reflector chip can result in an experimentally measured reduction of the facet power reflectance by a factor of up to 4 (corresponding to a facet reflectance of <1.5% or equivalently a reflection spectrum modulation depth of <0.066 dB). The main limiting factor during this project was the performance of the RSOA dies: aiming at maintaining the cost of the proposed laser configuration as low as possible, commercially available, cheap RSOA dies were used[3], which exhibited slight variations in the quality of the AR coating of their front facet. A maximum gain ripple extinction ratio (ER) deviation between ~1.7 dB and ~8.5 dB at the spectral region of interest (between 1510 and 1560 nm) was experimentally observed at a drive current of 60 mA for the available dies[4]. **Fig. 5.2b** and **5.2c** depict the difference in the amplitude of the gain ripple in the transmission spectra of two RSOA dies in the spectral region between 1520 and 1530 nm.

In order to ensure good mode selectivity, high SMSR, and lasing wavelength stability, RSOA dies with maximum extinction ratios <2.5 dB (at 60mA, between 1510 and 1560 nm) were used during this project, combined with reflector chips with relatively high power reflectance coefficients (R up to 40%, corresponding to an extinction ratio of 2.21 dB). This approach was followed in an attempt to maximize the likelihood of obtaining a net gain maximum as a result of the resonant reflection from the PhC cavity-based mirror (based on the above discussion). According to the analysis in Section 2.5, it is evident that in the presented configuration, for a given average internal loss value $<\alpha_i>$ and RSOA mirror reflectivity, lower resonant reflector reflectivity values result in higher differential quantum efficiencies (and therefore higher wall-plug efficiencies) and lower gain thresholds. This observation is in good agreement with the results presented by Zilkie et al. in [2], where high experimental efficiency for a similar EC laser design (utilizing a Bragg grating on SOI as an external reflector) was obtained for an output mirror grating with low reflectance (R = 0.15, corresponding to a extinction ratio of 0.7 dB). Based on the previously discussed considerations, it can be inferred that a further suppression of the facet back-reflections (by e.g. optimizing the AR coatings on the RSOA front facet and on facets of the bus waveguide on the Silicon chip) could lead to a significant improvement of the performance of the EC laser device of this chapter.

5.3 Experimental Setup and Characterization

[3] Retail cost of 15000€ per wafer of 40000 dies, corresponding to a die cost of < 0.40€/die (assuming a yield of ~95%). This price can be further reduced in the case of mass production.

[4] The maximum extinction ratio of the gain ripple in the transmission spectra (for the spectral region between 1510 and 1560 nm) at 50 mA was >1.5 dB and <=3 dB for 65% of the available for this project RSOA dies, >3 dB and <=5 dB for 18% of them, and >7.5 dB for the remaining 18%.

As in previous parts of the project, the transmission of the photonic crystal cavity-based chips used in this part was measured prior to their employment as reflectors. For this, the technique and optical setup shown in **Fig. 4.2a** and described in Section 4.3 were used. For the characterization of the compact EC laser, a similar setup was used and is shown in **Fig. 5.3**. A Reflective Semiconductor Optical Amplifier (RSOA) die was mounted on a thermally conductive AlN sub-mount, which was placed on a 5-axis alignment stage. The Si-based external reflector chip was placed on a single axis horizontal translation stage. The laser cavity was formed by edge-coupling the RSOA waveguide and the bus waveguide of the external reflector; alignment for optimum coupling was found by maximizing the output power at the end of the bus waveguide below threshold. The output of the laser cavity (as described in Section 5.2) was collected using a lensed single-mode fiber (SMF) [5] that was connected to an InGaAs photodetector (PD) – the output of which was read on a digital sampling oscilloscope (DSO) – and an optical spectrum analyser (OSA – with a maximum resolution of 0.01 nm), used for the observation of the spectral power distribution of the device under test (DUT). An infrared camera (IRC) was used to assist the alignment of the RSOA and the lensed fiber with the waveguides on the chip. The sensitivity of the camera spanned from visible to infrared frequencies, allowing the simultaneous observation of the components and their features, and of the infrared light (from the ASE source) transmitted through the bus waveguides. The temperature of both the mounted

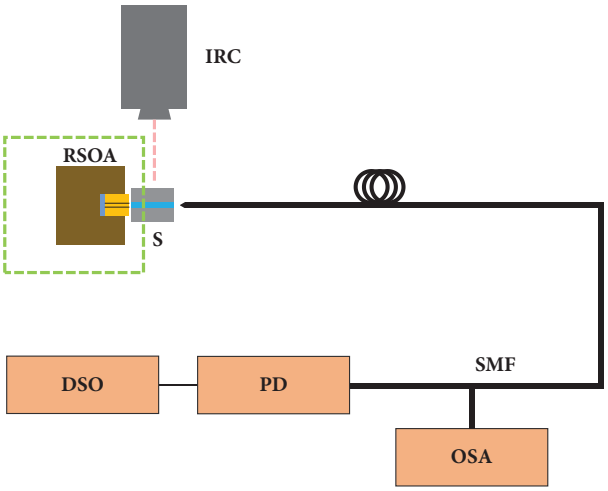

Figure 5.3 Experimental characterization setup of the proposed compact external cavity laser, comprising a Reflective Semiconductor Optical Amplifier on mount (RSOA). The dashed light green frame highlights the EC laser cavity. S: silicon chip/photonic crystal cavity based reflector, DSO: digital sampling oscilloscope, PD: photodetector, OSA: optical spectrum analyser, SMF: lensed single-mode fiber.

RSOA and of the external reflector chip could be independently controlled by using Peltier elements, which enabled spanning between 20 °C and 80 °C. It should be noted that the Peltier elements were used solely for the study of the behaviour of the device as a function of temperature.

[5] For completeness, the laser cavity emission was also collected at the end of the SU8 bus waveguide using a pair of aspheric lenses (and was launched in a SMF that was then connected to the InGaAs PD and the OSA). The observed results were the same in both cases (lensed fiber and pair of aspheric lenses).

Unless otherwise stated, the laser characterization was done at room temperature, as the examined device runs effectively without active cooling.

5.3.1 Laser Characterization

A microscope image of the compact EC laser cavity can be seen in **Fig 5.4**. **Fig 5.5a** shows the waveguide-coupled (wc) light versus current (LI) curve for a compact laser cavity comprising a DA cavity with lattice constant α = 390 nm and fill factor r/α = 0.28 (r the radius of a hole). The output power of the laser was measured using a Thorlabs digital power-meter connected to the lensed fiber. The threshold current was found to be 12.8 mA. The kinks in the LI curve are caused by mode-hopping, which occurs as the selected lasing mode of the cavity jumps to an adjacent longitudinal mode (as explained in Section 2.5) due to the thermo-optic effect as the laser temperature rises with drive current. **Fig. 5.5b** shows a contour plot of the lasing spectra measured at currents from 10 to 80 mA, with the drive current axis aligned that of **Fig. 5.5a**. It can be seen that the LI curve kinks happen at the same currents as the mode hops. Parasitic cavities from non-zero back-reflections from the Silicon chip facets can be responsible for minor LI discontinuities (as explained in Section 5.2.2). A wc-slope efficiency ηs > 0.14 mW/mA was measured, corresponding to a maximum wc-wall-plug efficiency of > 8% at 40 mA (as shown in **Fig. 5.5d)**.

As the experimentally observed laser linewidths were smaller than the resolution limit of the OSA (0.01 nm), a self-heterodyne method [14] was used to shift the spectral information of the high optical frequencies to lower frequencies that can be measured with electronics. For a

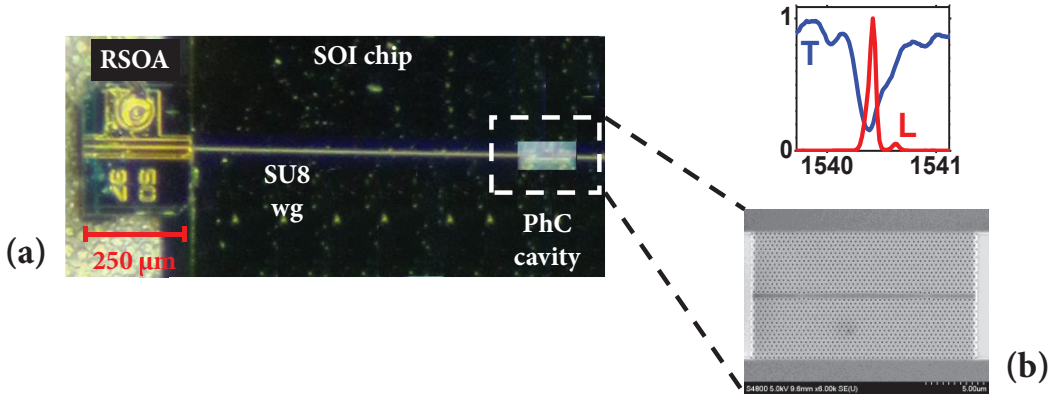

Figure 5.4 (a) Top-view microscope image of experimental setup. An overhanging RSOA chip (250 μm long) on mount is butt-coupled to the external reflector Silicon chip, comprising a polymer SU8 waveguide vertically coupled to a Dispersion Adapted (DA) photonic crystal cavity. (b) SEM image of the DA PhC cavity; the inset shows the correspondence of the lasing wavelength (L – red curve) of an indicative compact laser configuration to a resonance in transmission (T – blue curve) of the Silicon reflector chip.

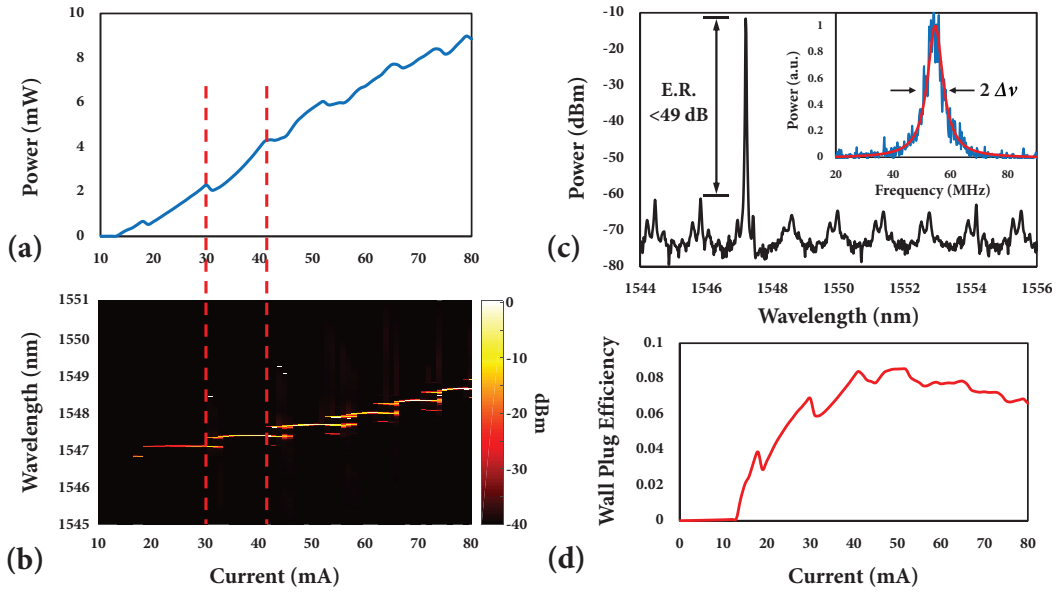

Figure 5.5 Characterization of compact external cavity laser with resonant external reflector comprising a DA PhC cavity with lattice constant a = 390 nm and fill factor r/a = 0.28. (a) Waveguide-coupled LI curve at room temperature, and (b) contour plot of normalized lasing spectra versus drive current and wavelength, with the current range matched to the x-axis of (a). (c) Lasing spectrum at 50 mA. An extinction ratio of <49 dB was observed. Inset: Self-heterodyne linewidth measurement spectrum (blue) with Lorentzian fit (red) centered at 55 MHz (the frequency of the AOM). A laser linewidth of ~4.5 MHz can was measured. (d) Wall-plug efficiency at room temperature as a function of drive current.

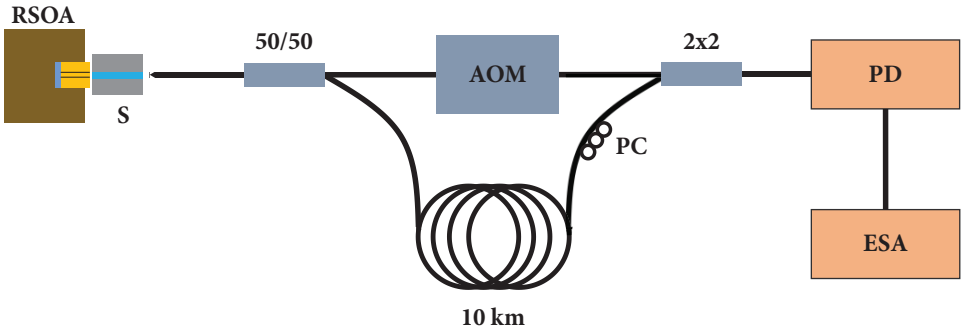

Figure 5.6 Setup for self-heterodyne linewidth measurement. The output of the laser is split into half with a 50/50 fiber-optic splitter. The two parts are sent through an acousto-optic modulator (AOM) driven at a constant frequency of 55 MHz and a fiber delay line of 10 km, respectively. The two uncorrelated parts are then combined again at 2x2 fiber-optic splitter and their beating is recorded by a high-speed photoreceiver (PD) connected to an electrical spectrum analyser (ESA). A fiber-optic polarization controller (PC) is used to ensure that the two beam parts maintain the same polarization.

self-heterodyne measurement the output beam of the studied laser is split into two portions; one of them is sent through an acousto-optic modulator (AOM), which is driven at a constant

frequency and shifts all the optical frequency components by that frequency. The second portion is sent through a long optical fiber that provides time delay. The two portions are then superimposed and the resulting interference pattern is recorded using a photodetector. For sufficiently long time delays[6], the two portions become uncorrelated, and thus the beam can interfere with a time delayed version of itself, as if they were the outputs of two independent lasers offset by the frequency of the AOM. The beating of the two portions is essentially a multiplication in the time domain and is therefore equivalent to a (self-)convolution in the frequency domain. Given the Lorentzian line shape of the two interfering portions, the resulting beat note is also a Lorentzian with a full width at half maximum (FWHM) linewidth exactly twice that of the original laser beam (as both considered portions have the same linewidth and all their frequencies interfere[7]) and centered at the frequency of the AOM [14].

The setup used for the self-heterodyne linewidth measurements during this project can be seen in **Fig. 5.6**. The output of the DUT was split in two parts using a 50/50 fiber-optic splitter. One portion of it was sent through an AOM driven at a constant frequency of 55 MHz and the second portion was sent through a fiber delay line of 10 km (a fiber length of 10 km was used to ensure that the two parts are uncorrelated). The two beam components were then combined at a 2x2 fiber splitter and their beat note was recorded using a high-speed InGaAs photoreceiver (PD – at 38 GHz) connected to a 26.5 GHz Electrical Spectrum Analyser (ESA). The output spectra were centered at the frequency of the AOM (55 MHz) and their linewidth was twice that of the DUT (indicative spectrum shown in the inset of **Fig. 5.5c**). Linewidths down to 4.5 MHz for single-mode lasing with side-mode suppression ratio (SMSR) up to ~50 dB were observed at 50 mA (**Fig. 5.5c**).

As for the long cavity configuration of Chapter 4, lithographic control of the lasing wavelength was also demonstrated for the compact EC configuration of this chapter by collecting the output from laser cavities comprising resonant reflector chips with different PhC resonances. The cavity resonances in this case were tuned by varying the lattice constant α of the employed DA PhC cavity design [12]. The lattice constant of the considered PhC cavities ranged from α = 382 nm to α = 388 nm (in steps of 2 nm) and their fill factor was r/α = 0.28. The lasing spectra (at room temperature) from the different EC laser cavities at a drive current of 22 mA can be seen in **Fig. 5.7**. A change in the emitted wavelength of the first lasing mode of each device can be observed, indicating that the examined compact external cavity configuration is a suitable candidate for WDM optical links. As in Chapter 4, the non-equidistant spacing of the lasing modes is a result of fabrication disorder and the lasing characteristics (differential quantum efficiency and slope efficiency) varied depending on the power reflectance of each Si resonant mirror device.

[6] The criterion that needs to be satisfied for the two beams to be uncorrelated is that the delay length must be larger than the coherence length of the laser output (given by $L_{coh} = c/\pi\,\Delta\nu$, with $\Delta\nu$ being the linewidth of the laser).

[7] The convolution of the two portions in this case can be seen as the integral of the pointwise multiplication of them [25].

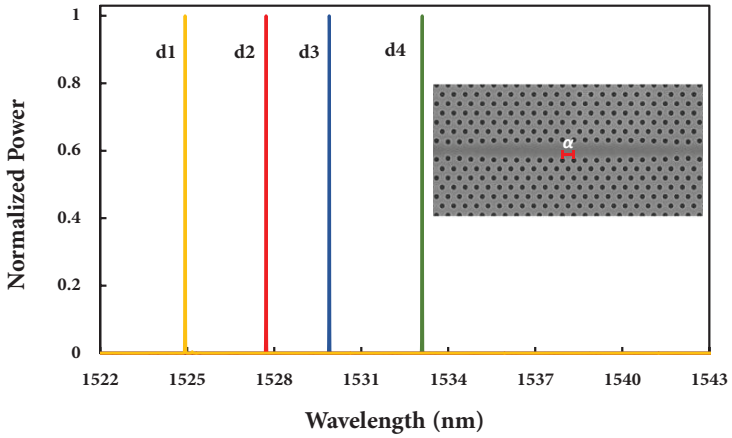

Figure 5.7 Lasing spectra for external cavity lasers utilizing resonant reflectors that comprise DA PhC cavities with different lattice constant α. Spectrum d1 (yellow) corresponds to a lattice constant α = 382 nm, d2 (red) to α = 384 nm, d3 (blue) to α = 386 nm and d4 (green) to α = 388 nm, respectively. The inset shows an SEM image of a DA PhC cavity. Tuning the lattice constant α (indicated in red) results in variation of the cavity resonances (and resonant reflections).

5.3.2 Alignment Tolerance

As previously discussed, one of the main application fields that the laser discussed here is aimed to address are WDM inter- and intra-chip optical networks (optical interconnects). Consequently, the suitability of the examined laser configuration for integration with silicon planar optical circuits is of particular relevance. In the selected EC architecture, Si/III-V integration can be achieved by butt-coupling via flip-chip bonding the RSOA chip on the SOI reflector chip, as described in [3, 15, 16, 17]. The vertical coupling platform utilized in the reflector chip is particularly advantageous for flip-chip bonding. The low refractive index of the bus waveguide allows for large cross-sections that facilitate better mode-field matching (and thus lower coupling losses) at the interface with the RSOA. FIMMWAVE was used to simulate the mode profiles of the RSOA and the ~3 x ~2.1 μm SU8 waveguides that were used for the experiments discussed in this chapter. A 1/e modal area of 4.51 μm^2 was calculated for the SU8 polymer waveguide (**Fig. 5.8b**), in close match to the respective 4.55 μm^2 mode area of the employed RSOA (**Fig. 5.8a**).

In order to achieve low-loss optical coupling with a flip-chip bonding configuration, the highly precise alignment of the two waveguides (the one of the RSOA and the one on the Silicon reflector chip) is also necessary. The RSOA-to-SU8 waveguide alignment sensitivity was therefore studied in the *x*, *y* and *z* directions (as these are indicated in **Fig. 5.8a**), both in simulations (using the FIMMPROP module by Photon Design) and experimentally. The waveguide structures used in the simulations were the same as the ones in the above described mode profile calculations. Single layer AR coating structures were considered on the facet of each waveguide at the RSOA-bus waveguide interface and the nominal maximum power coupling coefficient was found to be κ ~0.86. The RSOA waveguide was then displaced from the maximum

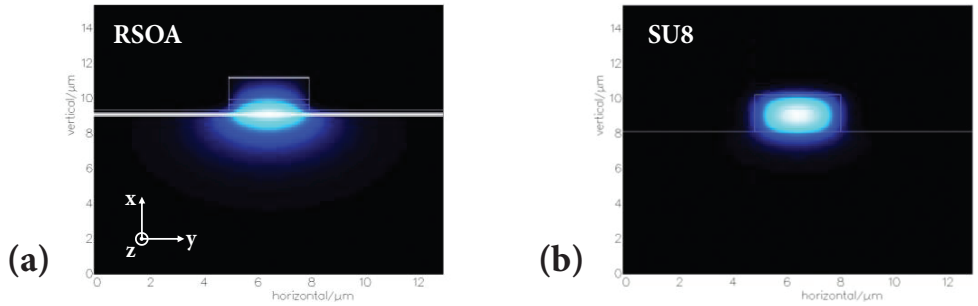

Figure 5.8 (a) Near-field profile of the mode on the facet of the RSOA. (b) Near-field profile of the mode on the facet of the SU8 bus waveguide.

coupling position with respect to the SU8 waveguide in steps of 0.1 μm, and the power coupling was studied relative to its maximum value in each of the *x*, *y* and *z* directions.

For the experimental part, the Silicon reflector chip was mounted on a single-axis translation stage and the RSOA on sub-mount was mounted on an individual 3-axis piezo-controlled precision stage. A lensed fiber was used at the output end of the examined SU8 waveguide on the Silicon reflector chip to measure the power. The RSOA was actively aligned (for driving currents below lasing threshold) with the SU8 polymer waveguide under study, and the position of maximum coupling was found. Typical RSOA-to-SU8 waveguide coupling losses of < 1.3 dB were measured at optimum alignment. The RSOA was then translated in the *x* and *y* directions from the maximum coupling position with respect to the polymer waveguide, and the power coupling was measured relative to its maximum value, as in the simulations. In order to study the impact of the waveguide misalignment to the performance of the laser, the aforementioned procedure was repeated and the threshold current of the laser cavity was recorded at different positions. The translation of the RSOA in the *z* direction was equivalent to the change of the EC laser cavity effective length and consequently of the length of the parasitic cavities formed due to non-zero facet reflections (as discussed in Section 5.2.2). As a result, discontinuities in the threshold current as a function of *z*-offset and case-dependent behaviour were observed. For this reason, threshold current results are presented only as a function of misalignment in the *x* and *y* directions.

Fig. 5.9a, **5.9b** and **5.9e** show indicative measurements of the normalized coupling efficiency as a function of lateral (*y*-direction), vertical (*x*-direction), and *z*-axis offset from the maximum coupling position, as well as the corresponding simulated results. **Fig. 5.9c** and **5.9d**, respectively, show the threshold current measurement of a typical laser cavity as a function of lateral (*y*-direction) and vertical (*x*-direction) offset from the maximum coupling position at a given (optimal) RSOA-SU8 waveguide separation. The difference in the alignment sensitivity – and consequently in the performance of the device – in the *x* and *y* directions, is attributed to the asymmetric mode profile of the RSOA (contrary to the more symmetric profile of the SU8 waveguide – shown in **Fig.5.8b** and **5.8c**), which leads to different matching (i.e. coupling) to the SU8 waveguide mode in the two directions. Respectively, the small discrepancy between the experimental and the simulated results in the *x* and *y* axes was because of slight variations in the

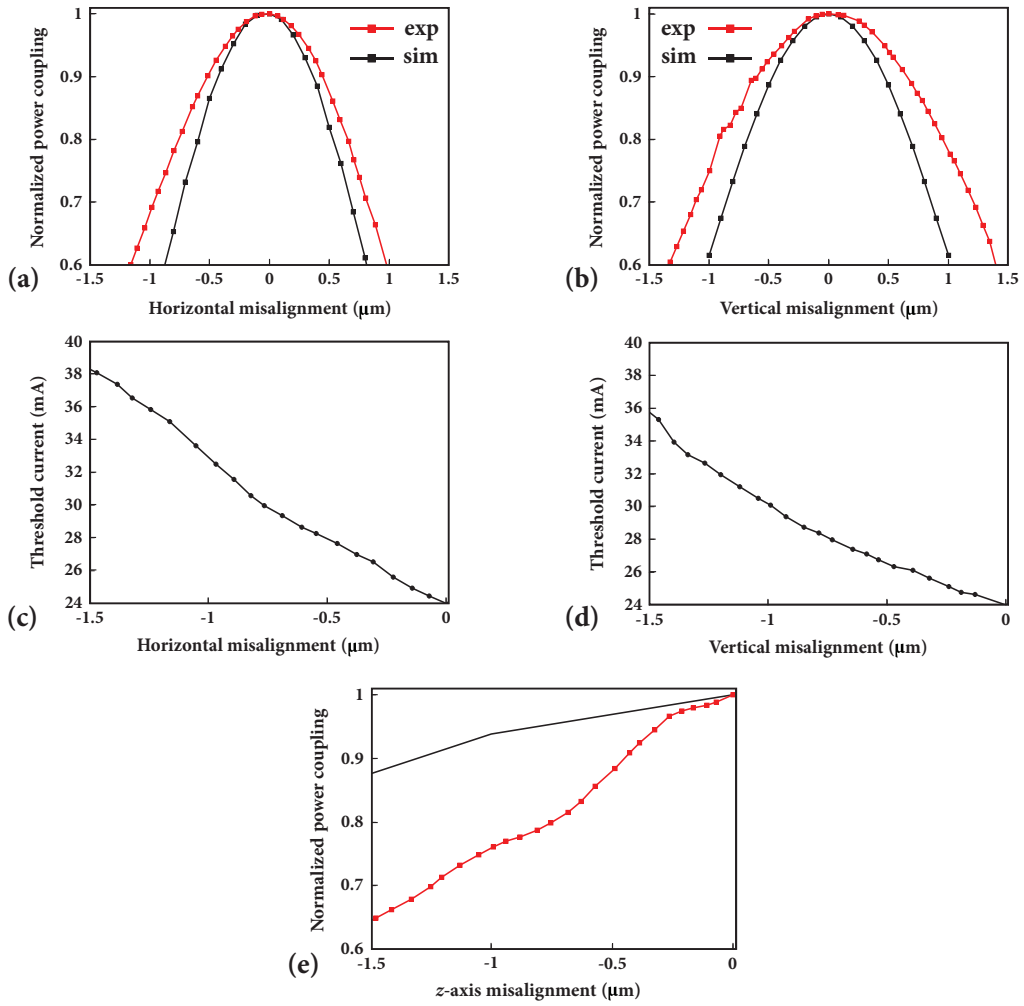

Figure 5.9 Experimental (black curve) and simulated (red curve) normalized power coupling coefficient as a function of (a) horizontal (*y*-axis), (b) vertical (*x*-axis), and (e) *z*-axis misalignment of the RSOA from the SU8 bus waveguide on the reflector chip, relative to the maximum coupling position. Threshold current as a function of (c) horizontal (*y*-axis) and (d) vertical (*x*-axis) RSOA-SU8 waveguide offset, relative to the minimum threshold current position.

dimensions of the fabricated SU8 waveguides (~ 3.2 μm x 2.15 μm) with respect to the values considered in the simulations(3.1 μm x 2.1 μm). The larger deviation observed between the experimental and the simulated results in the *z* axis was due to the fact that FIMMPROP is not optimized for mode solution (and propagation) in free space.

An increase of the coupling losses and of the threshold current of < 20% in the horizontal (*y*) direction and of < 15% in the vertical (*x*) direction was measured for a 500 nm misalignment from the optimal alignment position. Respectively, the measured increase in the coupling losses for the same offset (500 nm from the optimal alignment position) in the *z* direction was also < 15%. The experimentally observed alignment tolerances reveal the possibility for integration of the examined EC laser configuration by using chip bonding technology, for which similar

placement accuracies (±3σ <1.3 μm in the horizontal direction and ±3σ < 0.9 μm in the vertical direction) have been demonstrated [3, 17]. An additional advantage of the considered laser architecture is that the low-index bus waveguides on the Silicon reflector chip offer inherently high butt-coupling efficiency (through exhibiting low reflections and supporting large cross-sections). In this way, the need for using spot-size converting (SSC) or grating coupler (GC) structures is eliminated, a fact that simplifies not only the bonding, but also the design and fabrication processes.

5.3.3 Thermal Stability

As discussed in Chapter 1, precise wavelength control over a wide temperature range is a laser feature of key importance, especially in performance-demanding applications such as WDM optical interconnects. The motivation behind this necessity is the desire to avoid the use of active cooling and complicated control electronics for wavelength stabilization, in order to obtain higher energy efficiency and the potential for tighter WDM channel spacing (as explained in Sections 1.1 and 1.2). Given this situation, the performance and wavelength registration of the short EC laser presented in this chapter was studied at elevated temperatures. The selected configuration is of notable interest due to the inherently nonlinear behaviour of the photonic crystal cavity that is comprised in the Silicon reflector. Due to their ultra-high Q/V ratio [18], photonic crystal cavities can exhibit outstandingly high levels of stored energy (U), even for relatively low (sub-mW) levels of pumping power. This fact is of particular importance in photonic crystal cavities on Silicon platforms – like the ones considered in this project – as two-photon absorption (TPA) and free-carrier absorption (FCA) in Silicon are dependent on the intensity of the applied optical field [19], [20]. As a result, the large localized stored energy densities observed in Silicon PhC cavities can result in highly nonlinear behaviour.

More specifically, according to the analysis presented in [20] and following the notation used in Chapter 2, the intrinsic decay rate[8] of a PhC cavity Γ_0 can be written in terms of its linear and nonlinear components as

$$\Gamma_0(U) = \Gamma_{rad} + \Gamma_c + \bar{\Gamma}_{TPA}(U) + \bar{\Gamma}_{FCA}(U) \quad \textbf{(5.1)}$$

where Γ_{rad} is the decay rate due to radiation, Γ_C is the decay rate to the bus waveguide, and $\bar{\Gamma}_{TPA}(U)$ and $\bar{\Gamma}_{FCA}(U)$ are the averaged power/energy-dependent nonlinear decay rates corresponding to the two-photon and free-carrier absorptions, respectively. In the SOI platform considered in this project, and assuming the free-carrier absorption due to ionized dopants to be negligible, TPA is related to the imaginary part of the complex Kerr nonlinearity and is associated with a loss coefficient α_{TPA} that can be expressed as [19]

$$\alpha_{TPA} = \beta I(z) \quad \textbf{(5.2)}$$

where β is the TPA absorption coefficient (~0.5 cm/GW in Silicon at wavelengths near 1550 nm) and $I(z)$ is the pump intensity along (z-axis) the considered structure. The total optical power

[8] Here the decay rate is defined as the number of photons lost per unit time.

absorbed due to TPA in the effective volume of a resonant mode (V) of a PhC cavity for a given field distribution (i.e. at steady state) can therefore be described as [21]

$$P_{TPA} = \frac{\beta}{A_{eff}} \int P^2(r)\, dr \tag{5.3}$$

with A_{eff} being the effective modal area and $P(r)$ the power stored at a volume point r. The time-averaged decay rate due to TPA in the modal volume is thus

$$\Gamma_{TPA} \propto I^2 \tag{5.4}$$

with I expressing the intensity of the field stored in the cavity.

As every two photons absorbed via TPA lead to the appearance of an electron-hole pair, the rate of TPA-induced free carrier generation, assuming that the carriers are uniformly distributed inside the effective modal volume (V), is [19]

$$\frac{\partial N}{\partial t} = \frac{P_{TPA}}{2\hbar\boldsymbol{\omega_0}} - \frac{N}{\tau_c}\ . \tag{5.5}$$

with N the number of free carriers, τ_c the free-carrier lifetime (in the order of 400 picoseconds in oxide clad photonic crystals, like the ones considered in this project [22]), and ω_0 the resonant frequency of the PhC cavity. In this way and considering a steady state situation ($\partial N/\partial t$=0), TPA gives rise to a population (N) of free carriers that in turn induces FCA, which plays an important role in the nonlinear behaviour of a PhC cavity. The FCA is associated with a loss coefficient α_{FCA} that can be expressed as [19]

$$\alpha_{FCA} = \sigma N \tag{5.6}$$

with σ being the material dependent free-carrier cross-section (σ = 1.45 x 10^{-12} m^2 in Silicon). In this way, analogously to Eq. 5.4, the time-averaged decay rate due to FCA can be described as

$$\Gamma_{FCA} \propto \alpha_{FCA} I \tag{5.7}$$

The above discussion shows that TPA and FCA are related and they are both proportional to the modal confinement and the internal cavity energy U, and inversely proportional to the effective mode volume of the considered electromagnetic field in a PhC cavity [19, 20, 23]. The large energy densities that can be observed in the small volume of a PhC cavity lead to a change of the refractive index of the cavity, resulting in a power-dependent resonant wavelength. However, heating due to linear absorption is not the only factor responsible for that. The non-radiative recombination of the free carriers generated through the above described nonlinear processes (TPA and FCA) 'converts' the absorbed optical power to heat in the PhC cavity. The heat is generated in a region that matches the spatial distribution of the resonant mode in the cavity[9] as both TPA and FCA are dependent on the distribution of the electric field stored in the effective modal volume, producing one of the most effective nonlinear mechanisms of localized heating possible. Hence, the contributions of TPA (via the Kerr effect [19]), free-carrier dispersion and heating due to nonlinear absorption should be taken into

[9] With a slight broadening caused due to carrier diffusion.

account (in addition to heating due to linear absorption) when the power/heat-dependent dispersion of the resonance of a Silicon PhC cavity is considered.

The above described processes are of specific importance in the EC configuration examined in this chapter, as the reflector chip comprises a PhC cavity on SOI, the resonance of which defines the lasing wavelength (as explained in Chapters 2 and 4). The optical power (of the laser cavity) dissipated in the PhC cavity via TPA and FCA drives the temperature of the reflector significantly above ambient in a nonlinear fashion (as indicated by Eq. 5.4 and 5.7), resulting in a dependence of the lasing wavelength on the intra-cavity power stronger than in conventional lasers with similar output power/used in optical interconnect applications (but without actually negatively affecting the lasing threshold or efficiency as the Silicon reflector and gain chips are spatially separated).

It can be therefore inferred that wavelength stability in the studied EC laser architecture can be achieved without active cooling, simply by tuning the lasing power. More particularly, a zero net shift of the emitted wavelength can be obtained if the laser power is appropriately increased at lower operating temperatures. The strong nonlinear dependence of the emitted wavelength to the intra-cavity power indicates that wavelength stabilization with this technique can be achieved in the EC design discussed in this chapter at a lower power penalty that in other respective laser designs. The suggested strategy will result in a slowly varying average power at the network, which can be compensated for through electronic signal conditioning.

The aforementioned technique for wavelength stabilization was verified experimentally. The CW laser characterization at room temperature, described in Section 5.3.1, showed an emitted wavelength red-shift of ~2.5 nm for drive currents ranging between 15 and 80 mA. In order to explore the effects of temperature variations on the laser performance, the drive current was kept constant at 80 mA and the substrate temperature of both the RSOA and the Silicon reflector chips was swept (via the Peltier elements) between 20^{o} and 80^{o} C, in steps of 10^{o} C. The measured lasing spectra can be seen in **Fig. 5.10a**, revealing a red-shift of the emitted wavelength of ~4 nm for the considered temperature increase. To achieve the stabilization of the emitted wavelength, the measurements were repeated for the same temperature range (between 20^{o} and 80^{o} C, in steps of 10^{o} C), but this time for a varying drive current (between 150 and 50 mA). More specifically, as the substrate temperature of the active and the passive chips was decreased, the laser drive current was increased, causing the heating of the PhC cavity on the Silicon reflector and resulting in a ±0.38 nm emitted wavelength variation (with a central wavelength of 1550.85 nm) over the entire temperature span (**Fig. 5.10b**) for a laser output power increase by a factor of 9 (from ~1.4 mW of wc-output power at 80^{o} C to ~13 mW at 20^{o} C).

The above experiments/measurements were repeated with a packaged monolithic InP distributed feedback (DFB) laser (CQF935/56 by JDS Uniphase) that is commonly used as an external light source in optical telecommunication applications. The measured emitted wavelength red-shift for the DFB laser over the same substrate temperature range (between 20^{o} and 80^{o} C) at a fixed drive current of 80 mA was ~6 nm (**Fig. 5.10b**). **Fig. 5.10c** shows a comparison of the wavelength dependence on emitted power for the two configurations (DFB and short cavity EC laser of this chapter). A linear dependence (with a slope of < 0.04 nm/mW)

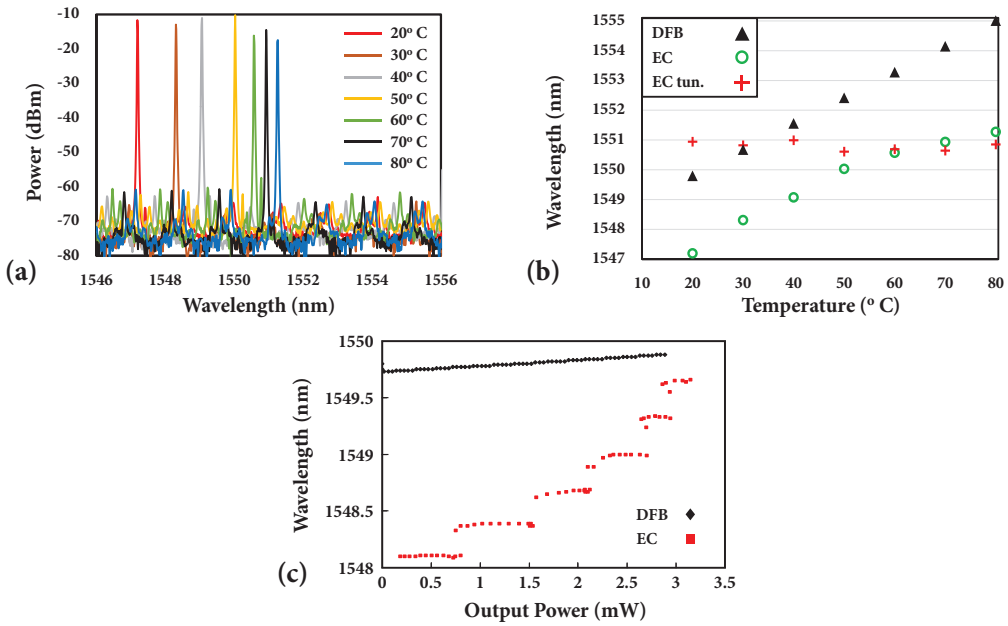

Figure 5.10 (a) Lasing spectra at 80 mA for a temperature span of 60° C (from 20° to 80° C, in steps of 10° C). A red-shift of the emitted wavelength of ~4 nm can be observed. (b) Emitted wavelength as a function of temperature for: a packaged DFB laser at a drive current of 80 mA (black triangles), a compact EC laser at 80 mA (green circles), and the same compact EC laser where wavelength stabilization is achieved by drive current tuning (from 150 mA to 50 mA, for 20° C through 80° C, respectively – red crosses). A ±0.38 nm emitted wavelength variation is observed for the power tuning technique. (c) Emitted wavelength as a function of the fiber-coupled output power for a packaged DFB laser (black rhombi) and a compact EC laser (red squares). The significantly stronger dependence of the emitted wavelength on the intra-cavity power can be inferred for the compact EC configuration. A compact external cavity laser with resonant external reflector comprising a DA PhC cavity with lattice constant α = 390 nm and fill factor r/α = 0.28 was considered for the above measurements.

is observed for the DFB laser, contrary to the nonlinear trend that the EC laser exhibits (which results in a wavelength shift of >1.5 nm over a range of < 3 mW). It can be thus deduced that wavelength stabilization through output power tuning cannot be achieved equally effectively for the considered DFB configuration as for the studied EC laser.

This assumption was confirmed experimentally, as an increase in the driving current of 150 mA (from 50 to 200 mA) was required for the compensation of a temperature shift of 10° C (between 20° and 30° C) of the DFB laser (15mA/° C), whereas a drive current change of 100 mA compensated for a temperature shift of 60° C (between 20° and 60° C) of the EC laser. The significant difference is attributed to the difference in the type of the reflector in each configuration: the DFB laser utilizes Bragg gratings as reflectors (with the wavelength shift caused by the thermal expansion of the grating period), while the considered EC laser features a PhC cavity on the reflector. Due to its high Q-factor/V ratio, the PhC cavity exhibits a significantly smaller effective mode volume. It can be easily understood that, as the nonlinear heating is inversely proportional to the modal volume, wavelength stabilization through power tuning can be more easily achieved with PhC cavity reflectors rather than with Bragg gratings.

Another important comparison to make is with an analogous hybrid EC laser structure with a Silicon resonant reflector on the μm scale. For this reason, the EC laser presented in [3] was considered, which utilizes a ring resonator as a wavelength selective element. The laser structure of [3] exhibits comparable waveguide-coupled (wc) output power and wall-plug efficiency, and an emitted wavelength red-shift with ambient temperature (at constant drive current and without) of 0.0787 nm/° C that matches closely to the value of 0.0845 nm/° C obtained for the EC laser studied here[10]. In the absence of any information for the laser in [3] regarding the emitted wavelength dependence on output power or drive current, an estimation can be made based on the modal volume of the resonator in each laser cavity (assuming the same SOI platform for both reflector chips). Given that the modal volume of the employed ring resonator is ~20 μm^3, as compared to a modal volume of ~2 μm^3 for the PhC cavity used in my project, it can be inferred that a 10 times higher density of power stored in the resonator would be needed to achieve the same heating rate. This larger heat capacity indicates a much weaker dependence of the emitted wavelength on the output power, and thereby a significantly smaller potential for wavelength stabilization through power tuning (in comparison to the case where a PhC cavity is the wavelength selective element in an EC laser configuration).

The highly nonlinear nature of the PhC cavity structure in the silicon reflector enables the effective stabilization of the emitted wavelength without active cooling, through tuning of the output power at a lowest power penalty, rendering the EC laser architecture presented in this chapter suitable for applications in which precise wavelength registration is of critical importance. However, the previously discussed experimental wavelength stability with a ±0.38 nm variation over a temperature span of 60° C (between 20° and 80° C) was achieved in the compact EC laser configuration under study for an output power decrease by a factor of 9. This result indicates the requirement for a datacommunication network/interconnection with a large dynamic range of operating power. In order to alleviate this requirement and improve the efficiency of the suggested wavelength stabilization technique, the removal of the Silicon substrate on the SOI reflector chip can be considered (e.g. by etching with XeF_2), as shown in **Fig. 11b**. **Fig. 5.11c** and **5.11d** show the simulated thermal profile of a DA PhC cavity[11] with Silicon (corresponding to the cross-section of **Fig. 5.11a**) and air substrate (corresponding to the cross-section of **Fig. 5.11b**) respectively, at room ambient temperature, for a stored power of 2 mW. It is apparent that in the absence of a substrate, the dissipation of the (nonlinearly) generated heat is less efficient, resulting in higher temperatures for the same levels of power stored in the PhC cavity. This is reflected on the comparison of the simulated PhC cavity temperature as a function of stored power in each case, shown in **Fig. 5.11e**. An enhancement of the heating mechanism by a factor > 2.5 can be observed, revealing the potential of undercutting to drastically reduce the power penalty required for the wavelength stabilization of the examined EC laser scheme. This increased sensitivity can be exploited to minimize the reduction in the average power variation required for the power tuning of the emitted wavelength, indicating the potential of using the EC laser configuration

[10] In both cases no wavelength stabilization technique (active cooling or power tuning) was employed, and a temperature range between 20° and 60° C was considered, as that was the span examined in [3].

[11] Simulation results obtained in COMSOL Multiphysics. The dimensions of the DA PhC cavity considered in the simulations were 10 μm x 20 μm, equal to the dimensions of the DA PhC cavities that were used in the experiments during the project. The corresponding modal volume was ~2 μm^3.

presented in this chapter in practical applications where precise wavelength registration/athermal operation is desired (e.g. WDM systems with dense channel spacing).

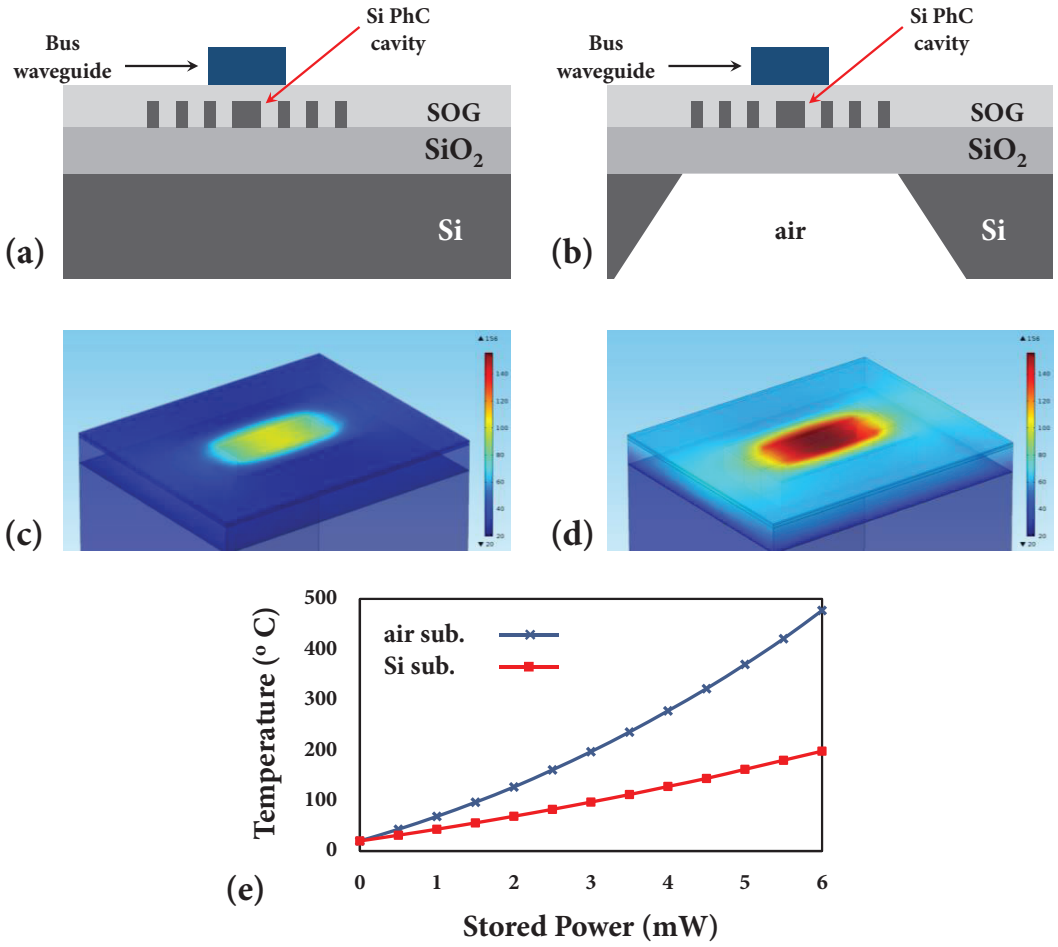

Figure 5.11 (a) Cross-section of the resonant reflector chip on SOI. (b) Cross-section of the resonant reflector chip on SOI with an undercut of the Silicon substrate underneath the PhC cavity. Thermal profile of the PhC cavity on the SOI resonant reflector chip with (c) a Silicon substrate (as shown in (a)), and (d) an air substrate (as shown in (b)), for a stored power of 2mW. (e) Simulated localized DA PhC cavity temperature as a function of stored power for Silicon (red) and air (blue) substrate.

5.4 Discussion

In this chapter I have presented the function and performance characteristics of a hybrid external cavity laser design consisting of a 250-μm long RSOA die on submount and a Silicon resonant reflector with a PhC cavity vertically coupled to a dielectric bus waveguide. As in Chapter 4, a combination of SU8 polymer waveguides and Dispersion Adapted (DA) PhC cavities [12] was used on the reflector chips for technological convenience. Lasing thresholds around 12-13 mA

were observed for waveguide-coupled (wc) output powers up to 8.5 mW (at 80 mA) and wc-wall-plug efficiencies up to ~8.5 % (at 41 mA) at emitted wavelengths around 1550 nm. The short length of the laser cavity was employed as an inherent mechanism towards single longitudinal mode operation. A single mode laser linewidth of ~4.5 MHz was measured using a self-heterodyne technique and the observed side-mode suppression ratios (SMSR) were consistently in excess of 40 dB (reaching a maximum of 50 dB). Lithographic tuning of the emitted wavelength was demonstrated by shifting the lattice constant of PhC cavity in steps of 2 nm, revealing the dependence of the emitted wavelength in the examined EC configuration on only the resonance of the PhC cavity on the reflector chip, as well as the potential of dynamically tuning the emitted wavelength of the laser by electro-optic modulation of the PhC cavity resonances, at ultra-low power budgets [24].

The vertical coupling scheme selected for the reflector chip, apart from offering a solution to the problematic interfacing of Silicon PhC cavities (enabling thus their use in real-life application where footprint and a high Q-factor/V ratio are key features), allows the use of bus waveguides with low refractive index. In this way, the implementation of waveguides with larger cross-sections is possible, with modal areas (4.51 μm^2 for the SU8 waveguides considered in this chapter) that permit highly efficient butt-coupling with the RSOA waveguides (e.g. <1.5 dB to the RSOA waveguides with modal areas of 4.55 μm^2 considered in this chapter) or with single mode fibers, without the use of auxiliary structures (such as spot-size converters or grating couplers). A further RSOA-to-SU8 waveguide alignment sensitivity study revealed an experimental increase of the coupling losses and of the laser threshold current of < 20% in the horizontal direction and of < 15% in the vertical and z[12] directions for a 500 nm misalignment from the optimal alignment position (in agreement with the results obtained from simulations). The above results indicate the possibility for integration of the proposed EC laser architecture in practical application platforms by chip bonding technology, for which similar placement accuracies ($\pm 3\sigma$ <1.3 μm in the horizontal direction and $\pm 3\sigma$ < 0.9 μm in the vertical direction) have been demonstrated [3, 17].

Finally, apart from the small footprint and large FSR that it provides, the use of a PhC cavity-based reflector is particularly relevant for the stabilization of the emitted wavelength. PhC cavities can exhibit significantly high stored energy densities, leading to nonlinear heating due to TPA and FCA. The spatial extent of this heating is very similar to that of the optical mode of the cavity, resulting in a self-heating mechanism, inversely proportional to the modal volume [19], [20], that shifts the resonant wavelength of the PhC cavity. As the emitted wavelength in the examined EC architecture is dependent only on the PhC cavity resonance, this effect provides a route to achieving wavelength stability by tuning the output power (and therefore the power stored in the PhC cavity). In this way, a zero net shift of the emitted wavelength can be obtained if the laser power is appropriately increased (by simply increasing the drive current of the RSOA) at lower operating temperatures. Through this 'power tuning' technique, wavelength stability with a ±0.38 nm variation around the central wavelength (1550.85 nm) was achieved over a temperature span of 60° C (between 20° and 80° C) for a laser output power decrease by a factor of 9. Owing to the fact that PhC cavities exhibit the ultimate Q-factor/V ratio [18], this strategy can be applied to the EC laser presented here at a much lower power penalty than for equivalent

[12] The z-direction is defined along the axis of propagation of light in the considered waveguides.

configurations comprising Silicon reflectors based on structures with smaller Q-factor/V ratio (e.g. ring resonators) or on Bragg gratings. As a comparison, an analogous device presented in [3] achieves wavelength selectivity by utilizing a ring resonator, the modal volume of which is ~20 μm^3 – 10 times larger than the modal volume of the PhC cavity used for this project. The potential of further improving the efficiency of the proposed wavelength stability technique by removing the Silicon substrate on the SOI reflector chip (e.g. by XeF_2 etching) was studied in simulations. The dependence of the temperature of a DA PhC cavity to the stored power was simulated to increase by a factor of > 2.5 in the case of an undercut cavity, as compared to the case of a cavity with Silicon substrate, suggesting that undercutting can drastically reduce the power penalty required for the wavelength stabilization of the examined laser. The selected EC scheme is additionally beneficial for this wavelength stabilization method, as the spatial separation of the passive and the active parts ensures that the characteristics of the device (threshold current and efficiency) are not compromised.

Chapter 6 discusses the potential of including wavelength modulation functionality in the EC laser architecture proposed in this chapter, as well as its further potential.

References

[1] T. Tekin, N. Pleros, R. Pitwon and A. Hakansson, Optical Interconnects for Data Centers, Woodhead Publishing, NOV 2016.

[2] A. Zilkie, P. Seddighian, B. J. Bijlani, W. Qian, D. C. Lee, S. Fatholoumi, J. Fong, R. Shafiiha, D. Feng, B. J. Luff, X. Zheng, J. E. Cunningham, A. V. Krishnamoorthy and M. Asghari, "Power-Efficient III-V/Silicon external cavity DBR lasers," *Optics Express,* vol. 20, no. 21, pp. 23456-23462, OCT 2012.

[3] S. Tanaka, S.-H. Jeong, S. Sekiguchi, T. Kurahashi, Y. Tanaka and K. Morito, "High-output power, single-wavelength silicon hybrid laser using precise flip-chip bonding technology," *Optics Express,* vol. 20, no. 27, pp. 28057-28069, DEC 2012.

[4] S. Lin, S. S. Djordjevic, J. E. Cunningham, I. Shubin, Y. Luo, J. Yao, G. Li, H. Thacker, J.-H. Lee, K. Raj, X. Zheng and A. V. Krishnamoorthy, "Vertical-coupled high-efficiency tunable III-V-CMOS SOI hybrid external-cavity laser," *Optics Express,* vol. 21, no. 26, pp. 32425-32431, DEC 2013.

[5] Y. Zhang, S. Yang, H. Guan, A. E.-J. Lim, G.-Q. Lo, P. Magill, T. Baehr-Jones and M. Hochberg, "Sagnac loop mirror and micro-ring based laser cavity for silicon-on-insulator," *Optics Express,* vol. 22, no. 15, pp. 17872-17879, JUL 2014.

[6] A. A. Gonzalez-Fernandez, A. A. Liles, S. Pesheyev, K. Debnath and L. O'Faolain, "Wavelength-controlled external cavity laser with a silicon photonic crystal resonant reflector," in *Proceedings SPIE 9753, Optical Interconnects XVI, 975317*, San Francisco (US), 2016.

[7] A. P. Bakoz, A. A. Liles, E. A. Viktorov, L. O'Faolain, T. Habruseva, G. Huyet and S. P. Hegarty, "Lasing Dynamics of photonic crystal reflector laser," in *Proceedings SPIE 9892, Semiconductor Lasers and Laser Dynamics VII, 989204*, San Francisco (US), 2016.

[8] A. P. Bakoz, A. A. Liles, E. A. Viktorov, L. O'Faolain, G. Huyet and S. P. Hegarty, "Photonic Crystal Reflector Laser," in *International Conference Laser Optics (LO)*, St Petersburg (RU), 2016.

[9] A. A. Liles, A. P. Bakoz, A. A. Gonzalez-Fernandez, T. Habruseva, S. Persheyev, G. Huyet, S. P. Hegarty and L. O'Faolain, "Hybrid Photonic Crystal Laser," in *18th International Conference on Transparent Optical Networks (ICTON)*, Trento (IT), 2016.

[10] A. A. Liles, A. A. Gonzalez-Fernandez and L. O'Faolain, "III-V/Silicon External Cavity Laser with Photonic Crystal Cavity Reflector," in *12th International Symposium on Photonic and Electromagnetic Crystal Structures (PECS XII)*, York (UK), 2016.

[11] E. Murphy, C. MIchie, H. White, W. Johnstone, A. E. Kelly and I. Andonovic, "High Temperature Wavelength Division Network for Avionic Applications," *Journal of Lightwave Technology ,* vol. 31, no. 18, pp. 3006-3013, SEP 2013.

[12] K. Welna, S. L. Portalupi, M. Galli, L. O'Faolain and T. F. Krauss, "Novel Dispersion Adapted Photonic Crystal Cavity with Improved Disorder Stability," *IEEE Journal of Quantum Electronics,* vol. 48, no. 9, pp. 1177-1183, SEP 2012.

[13] M. J. R. Heck, J. F. Bauters, M. L. Davenport, J. K. Doylend, S. Jain, G. Kurczveil, S. Srinivasan, Y. Tang and J. E. Bowers, "Hybrid Silicon Photonic Integrated Technology," *IEEE Journal of Selected Topics in Quantum Electronics,* vol. 19, no. 4, p. 610017, JUL/AUG 2013.

[14] T. Okoshi, K. Kikuchi and A. Nakayama, "Novel method for high resolution measurement of laser output spectrum," *Electronics Letters,* vol. 16, no. 16, pp. 630-631, JUL 1980.

[15] N. Fujioka, T. Chu and M. Ishizaka, "Compact and low power consumption hybrid integrated wavelength tunable laser module using silicon waveguide resonators," *Journal of Lightwave Technology,* vol. 28, no. 21, pp. 3115-3120, SEP 2010.

[16] T. Shimizu, N. Hatori, M. Okano, M. Ishizaka, Y. Urino, T. Yamamoto, M. Mori, T. Nakamura and Y. Arakawa, "High density hybrid integrated light source with a laser diode array on a silicon optical waveguide platform for inter-chip optical interconnection," in *IEEE Group IV Photonics*, London, 2011.

[17] F. E. Doany, R. A. Budd, L. Schares, T. N. Huynh, M. G. Wood, D. M. Kuchta, N. Dupuis, C. L. Schow, B. G. Lee, M. Moehrle, A. Sigmund, W. Rehbein, T. Y. Liow, L. W. Luo and G. Q. Lo, "A Four-Channel Silicon Photonic Carrier with Flip-Chip Integrated Semiconductor Optical Amplifier (SOA) Array Providing >10-dB Gain," in *IEEE 66th Electronic Components and Technology Conference* , Las Vegas, Nevada, USA, 2016.

[18] M. Notomi, K. Nozaki, A. Shinya, M. Shinji and K. Eiichi, "Toward fJ/bit optical communication in a chip," *Optics Communications,* vol. 314, pp. 3-17, MAR 2014.

[19] Q. Lin, O. J. Painter and G. P. Agrawal, "Nonlinear optical phenomena in silicon waveguides: Modeling and applications," *Optics Express,* vol. 15, no. 25, pp. 16604-16644, NOV 2007.

[20] P. E. Barclay, K. Srinivasan and O. Painter, "Nonlinear response for silicon photonic crystal microresonators excited via an integrated waveguide and fiber taper," *Optics Express,* vol. 13, no. 3, pp. 801-820, JAN 2005.

[21] T. K. Liang and H. K. Tsang, "Role of free carriers from two-photon absorption in Raman amplification in silicon-on-insulator waveguides," *Applied Physics Letters,* vol. 84, no. 15, pp. 2745-2747, APR 2004.

[22] L. O'Faolain, D. M. Beggs, T. P. White, T. Kampfrath, K. Kuipers and T. F. Krauss, "Compact Optical Switches and Modulators Based on Dispersion Engineered Photonic Crystals," *IEEE Photonics Journal,* vol. 2, no. 3, pp. 404-414, APR 2010.

[23] Y. Zhang, C. Husko, S. Lefrancois, I. H. Rey, T. F. Krauss, J. Schröder and B. J. Eggleton, "Non-degenerate two-photon absorption in silicon waveguides: analytical and experimental study," *Optics Express,* vol. 23, no. 13, pp. 17101-17110, JUN 2015.

[24] K. Debnath, L. O'Faolain, F. Y. Gardes, A. Steffan, G. T. Reed and T. F. Krauss, "Cascaded modulator architecture for WDM applications," *Optics Express,* vol. 20, no. 25, pp. 27420-27428, DEC 2012.

[25] B. Osgood, "Lecture Notes for EE 261 The Fourier Transform and its Applications (Electrical Engineering Department, Stanford University)," [Online]. Available: https://see.stanford.edu/materials/lsoftaee261/book-fall-07.pdf. [Accessed 16 MAY 2017].

Chapter 6

Compact External Cavity Laser for Direct Frequency Modulation and Future Work

6.1 Introduction

One of the major goals towards the realization of complex Silicon Photonic systems is the monolithic integration of hybrid III-V/Silicon lasers with other functional components (passive or active) [1]. As discussed in Chapter 1, the power consumption in optical transceivers for data-links is roughly proportional to the modulation speed of an optical carrier. Wavelength Division Multiplexing (WDM) supports the transmission of multiple frequencies over one channel, allowing each frequency to be modulated at a much lower speed than that of a single frequency channel with the same bandwidth. It is thus considered to be the most energy efficient route for achieving the projected required bandwidth [2, 3, 4, 5, 6]. Resonator based active devices, can exhibit significantly low power consumption and driver delay through their ability to enhance light-matter interaction and effectively decrease the active device region size. In this way, they can easily exceed their counterparts in electrical interconnects (EI) in terms of performance, while their wavelength-selective nature is inherently suited for WDM applications [7]. The main disadvantage of resonance-based devices, however, is their sensitivity to the operating temperature. Consequently, matching the emitted wavelength of a laser source to the resonances

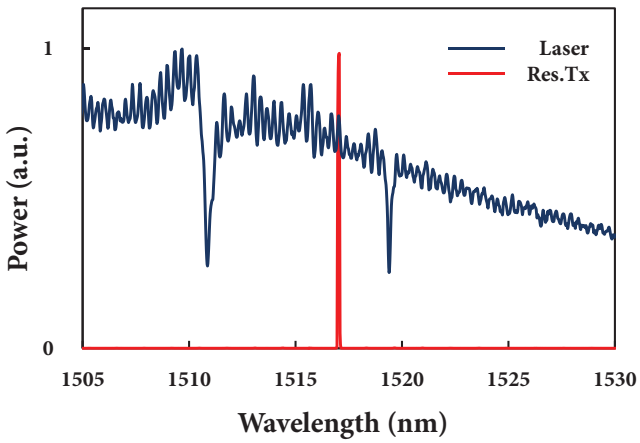

Figure 6.1 Schematic representation of the 'wavelength matching' problem: the emitted wavelength of the employed laser (red) does not coincide with the resonances of the resonant component (the transmission spectrum Tx of which is shown in blue).

of optical components of this type dictates the use of active cooling and control electronics, resulting in additional complexity and increased power consumption, and thus hindering their wide employment in practical applications [4, 8, 9]. A graphic representation of this 'wavelength-matching' problem is given in **Fig. 6.1**.

As electro-optic modulation is one of the most essential and fundamental functions of a Silicon photonic WDM optical network (and therefore also of a WDM optical interconnect), a significant amount of research has been put on tackling the above discussed problem of 'wavelength matching' for resonant modulators through the use of software or less power consuming electronics [10, 11], in order to take advantage of the high energy efficiency that they can offer. In this chapter, I explore the potential of direct modulation in the compact EC laser configuration presented in Chapter 5, by using a tunable Dispersion Adapted (DA) Photonic Crystal (PhC) cavity [12] as the resonant reflector, with a pn junction extending into the PhC defect, as described in [13]. The inclusion of the pn junction allows the electro-optical modulation of the refractive index of the PhC cavity – and therefore of its resonant response – in a way that is explained in the following section. As the emitted wavelength of the EC laser is decided by the resonant wavelength of the PhC cavity, tuning of the latter translates to a direct frequency modulation of the examined laser, eliminating the need for matching the lasing wavelength to the resonant wavelength of the modulator when the device is employed in a link that features resonant detection.

Similar approaches have been very recently demonstrated by Fujitsu [14] and Hewlett Packard [15], utilizing ring resonators as tunable elements in the laser cavity. In addition to the advantages of the vertical coupling scheme that have been discussed in Chapters 2 and 5, the attraction of PhC cavities for electro-optic modulation is their ultimate *Q*-factor/*V* ratio [16]: the total dissipated energy per bit in electro-optical modulators is $\Delta E_{bit} = (1/2)\, CV_{DD}^2$, where *C* is the modulator capacitance and V_{DD} is the supply voltage [17]. Owing to their ultra-small modal volume (*V*), PhC cavity-based modulators can exhibit very low capacitance (e.g. 5.6 x 10^{-18} F [18]) and thus a modulation power consumption of more than one order of magnitude lower than conventional ring resonators (sub-pJ/bit) [13, 18, 19]. Furthermore, PhC cavities typically have a large free spectral range (FSR), mitigating FSR-imposed limitations and significantly assisting channel scalability – in combination with the precise control of the PhC cavity resonances by lithographic tuning [20].

The devices used for all the experiments in this chapter were designed by myself. The doping and p-n junction formation on the devices took place in Tyndall National Institute. The rest of the fabrication was done by myself in the University of St Andrews. The experiments for Section 6.4 were conducted by myself in the University of St Andrews, and by myself and Andrei P. Bakoz (affiliations: Cork Institute of Technology (CIT), Tyndall National Institute and ITMO University) in Tyndall National Institute. The experimental frequency modulation data presented in **Fig. 6.9** were collected by Andrei P. Bakoz in Tyndall National Institute. The material related to this chapter has been published in [21].

6.2 Wavelength Tuning in Photonic Crystal Cavity Based Reflector

As explained in Chapters 2 and 5, the emitted wavelength of the examined EC laser is determined by the resonant wavelength of the PhC cavity on the vertically coupled reflector. The broad IR frequency spectrum generated in the RSOA through amplified spontaneous emission (ASE) is launched in the bus waveguide on the reflector chip. Light at frequencies matching the resonances of the Silicon PhC cavity couples to the cavity mode from the waveguide mode. A part of the coupled light is lost due to scattering and absorption inside the cavity and the rest couples back into the forward and backward propagating modes of the waveguide, the latter acting as wavelength-selective feedback for the laser cavity. It is therefore apparent that tuning the resonant wavelength of the PhC cavity (e.g. from a wavelength λ_1 to a wavelength λ_2) can result in a shift of the emitted wavelength (from a wavelength λ_1 to a wavelength λ_2), which translates into a modulation of the optical intensity monitored in λ_1. An illustrated representation of the situation can be seen in **Fig. 6.2**. Tuning of the resonant wavelength ($\Delta\lambda$) can be achieved through a shift (perturbation) of the refractive index of the PhC cavity material (Δn) that can be achieved optically, electrically or thermally. In all cases, the shift in the resonant wavelength (which can be a blue-shift if the refractive index decreases or a red-shift if the refractive index increases) is proportional to the change in the refractive index.

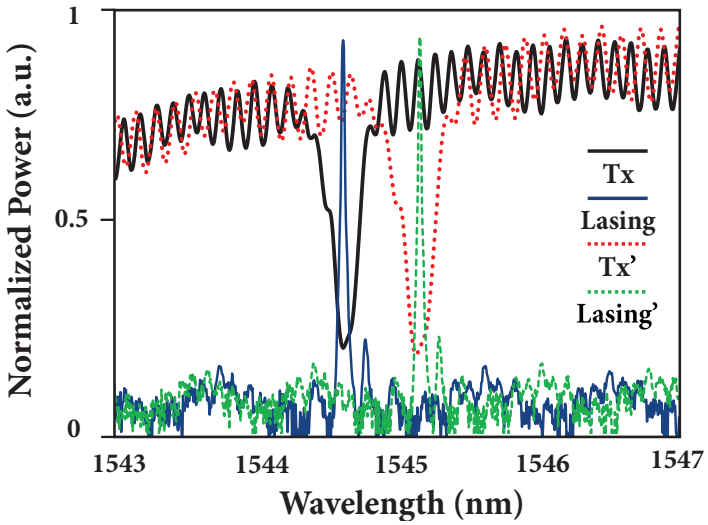

Figure 6.2 Illustration of direct frequency modulation in the compact EC laser configuration. Transmission spectra depict the shift of the resonant wavelength of the PhC cavity on the reflector from a wavelength λ_1 (Tx – black) to a wavelength λ_2 (Tx' – red dotted), which induces the shift of the emitted wavelength from λ_1 (Lasing – blue) to λ_2 (Lasing – green dotted), respectively.

The most efficient method of inducing a change in the refractive index of a bulk medium is by utilizing electro-optic effects (i.e. by applying an electric field), as they involve little or zero current flow and thus can offer low power operation. The application of an electric field to a material can result in a change in the real (electro-refraction) or in the imaginary part (electro-absorption) of the refractive index. The primary electro-optic effects that are useful in

semiconductor materials are the Pockels effet (linear electro-optic effect[1]) and the Kerr effect (quadratic electro-optic effect[1]) for electro-refraction, and the Franz-Keldysh effect for electro-absorption. However, the Pockels effect is absent from Silicon (due to its inversion symmetry) and the Kerr and Franz-Keldysh effects, though present, are very weak in it [22, 23].

In the absence of a strong electro-optical effect in Silicon, an alternative way of achieving the modulation of the refractive index in it is the plasma dispersion effect [24]. The plasma dispersion effect is related to the density of free carriers in a semiconductor, the change of which causes a change in the imaginary part of the refractive index (i.e. the absorption) in the semiconductor. This change can in turn affect the real part of the refractive index, with the relationship described by the Drude-Lorenz equations. Based on this fact, Soref and Bennett used optical absorption curves in literature and numerical analysis to evaluate the refractive index change (Δn) in Silicon for a wide range of electron-hole densities [22]. It was thus shown that the plasma dispersion induced Δn in Silicon is two orders of magnitude higher than the Δn due to the Kerr effect and the Franz-Keldysh effect, indicating that the plasma dispersion effect can be employed for the realization of modulator components in Silicon. They also produced empirical expressions for the relationship between the change in refractive index and absorption coefficient, and the change in the free carrier concentration in Silicon, for the communications wavelengths of 1.3 μm and 1.55 μm. These relationships are now universally used for the evaluation of plasma dispersion-based optical modulation in Silicon [24] and are given by

$$\Delta n = \Delta n_e + \Delta n_h = -[6.2 \times 10^{-22}\, \Delta N_e + 6.0 \times 10^{-18}\, (\Delta N_h)^{0.8}] \quad \textbf{(6.1)}$$

$$\Delta \alpha = \Delta \alpha_e + \Delta \alpha_h = 6.0 \times 10^{-18}\, \Delta N_e + 4.0 \times 10^{-18}\, \Delta N_h \quad \textbf{(6.2)}$$

at λ = 1.3 μm, and by

$$\Delta n = \Delta n_e + \Delta n_h = -[8.8 \times 10^{-22}\, \Delta N_e + 8.5 \times 10^{-18}\, (\Delta N_h)^{0.8}] \quad \textbf{(6.3)}$$

$$\Delta \alpha = \Delta \alpha_e + \Delta \alpha_h = 8.5 \times 10^{-18}\, \Delta N_e + 6.0 \times 10^{-18}\, \Delta N_h \quad \textbf{(6.4)}$$

at λ = 1.55 μm. ΔN_e and ΔN_h express the change in free electron and hole concentrations, while Δn_e and Δn_h express the change in the refractive index resulting from ΔN_e and ΔN_h, respectively. Finally, $\Delta \alpha_e$ and $\Delta \alpha_h$ express the change in the absorption coefficient as a result of ΔN_e and ΔN_h. In order to qualify this effect, a change in the carrier concentration of the order of $\Delta N_e = \Delta N_h = 5 \times 10^{17}$ cm^{-3} is considered, which can be easily produced by passing a current through Silicon. The material refractive index change caused by this ΔN at a wavelength of 1.55 μm is $\Delta n = -16.67 \times 10^{-4}$, which is sufficient for practical modulation applications in Silicon [24].

Plasma dispersion effect modulation in Silicon is typically achieved by forming a pn or a p-i-n junction in (or around) the effective modal volume of the optical component under consideration. Carrier plasma dispersion-based modulators on Silicon are divided into two main categories: injection type modulators and depletion type modulators. In the first case, the junction is forward biased and the applied voltage injects free carriers in it, causing a decrease in

[1] The terms 'linear' and 'quadratic' refer to the dependence of each effect on the applied electric field: the Pockels effect describes the refractive index change that is proportional to the electric field, while the Kerr effect describes the refractive index changes that is proportional to the square of the electric field.

the refractive index of the Silicon in the modal volume. In depletion type modulators, the junction is reverse biased and the application of voltage depletes the excess free carriers from the junction, resulting in an increase of the refractive index in the modal volume. The modulation speed of injection type modulators is typically limited to a few GHz by the free carrier lifetime in the junction [18, 25]. On the other hand, the speed in depletion based configurations is mainly determined by the RC constant of the junction and can by significantly higher [26, 27, 28].

Finally, refractive index modulation in Silicon can be achieved thermally, as a result of a local change in temperature. The thermo-optic coefficient in Silicon is dn/dt = 1.86 x 10^{-4}/K, corresponding to a temperature change of 9 °C for a Δn of 16.74 x 10^{-4} [24]. Even though this change is comparable in magnitude to the change induced by the plasma dispersion effect as shown previously, thermo-optic modulation is a much slower process (limited to modulation bandwidths in the MHz order) and therefore is primarily used for wavelength-tuning applications. Aiming at exploring the potential of the EC configuration of Chapter 5 for high-speed direct frequency modulation, the plasma dispersion effect was utilized for the experiments presented in this chapter.

6.3 The Laser Cavity

6.3.1 Design Description

The EC laser architecture examined in this chapter is almost identical the one presented in Chapter 5: a RSOA die on mount was butt-coupled to a bus waveguide that was vertically coupled to a Silicon PhC crystal cavity on an external reflector chip. The gain chip was again a 250-μm long InP ridge optical amplifier with AlGaInAS quaternary quantum wells (QW), mounted on a ceramic tile with its front end overhanging, as in Chapter 5. The back facet of the RSOA die was HR-coated with power reflectance R > 90%, while its front facet was coated with a multi-layer AR-coating to minimize back-reflections. A polymer SU8 waveguide (~3 μm x ~2.1μm) vertically coupled to a DA PhC cavity on SOI [12] was used on the external reflector chip in this case too. Both facets of the bus waveguide were coated with single-layer MgF_2 AR coatings. Unlike the configuration presented in Chapter 5, however, the resonant reflector chips used in the experiments of this chapter comprised a p^+pnn^+ junction extending into the DA PhC defect, as described in [13]. A schematic representation of the laser cavity and of the Silicon-based resonant mirror is given in **Fig. 6.3a** and **6.3b**, respectively.

The lasing mechanism is the same as described in Sections 4.2 and 5.2. As previously explained, the emitted wavelength of the EC laser examined here is decided by the narrow-bandwidth (sub-nm/few-pm) reflection of the resonant mirror at resonance of the PhC cavity on it. More specifically, following the notation of Section 2.5, the lasing wavelength is determined by the phase matching condition[2]

[2] Using the formula for a Fabry-Pérot (FP) cavity, as for a two-mirror semiconductor laser.

$$2\,k\left(\bar{n}_{ga}L_a + \bar{n}_{gp}L_{eff}(\lambda)\right) = 2m\pi \tag{6.5}$$

where $k = 2\pi / \lambda_{lasing}$ is its wave vector, $\bar{n}_{ga}$ and $\bar{n}_{gp}$ are the effective refractive indices of the active and the passive regions respectively, L_a is the length of the active region, and $L_{eff}(\lambda)$ is the effective passive length that also depends on the wavelength-dependent phase contribution of the PhC cavity. On this basis, a change in the resonant wavelength of the PhC cavity causes a change (in the *k* and *Leff* terms) of the phase matching condition (Eq. 6.5), and consequently a shift of the frequency of the longitudinal mode that lases. It is therefore understandable that direct frequency modulation of the proposed EC design at a given drive current can be achieved through the plasma dispersion modulation of the PhC cavity in the external reflector. The fabrication details of the tunable resonant mirrors are given in the following section.

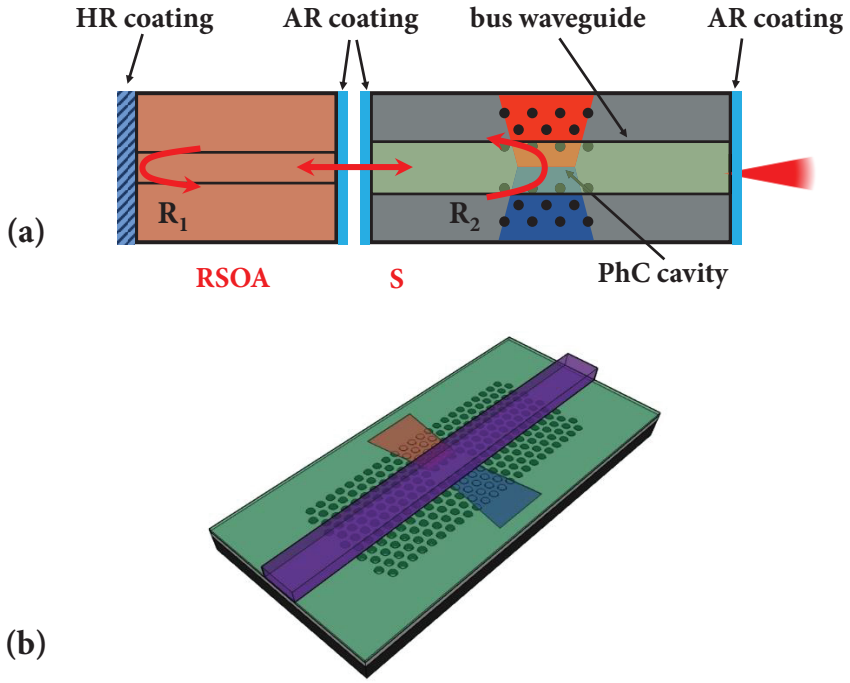

Figure 6.3 (a) Schematic representation of the compact external cavity laser configuration discussed in this chapter. The laser cavity is formed by butt-coupling a III-V-based Reflective Semiconductor Optical Amplifier (RSOA) to an external reflector chip (S), comprising a bus waveguide vertically coupled to a Silicon PhC cavity embedded in a pn junction, that provides tunable wavelength-selective optical feedback (R_2). The rear facet of the RSOA is HR-coated, acting as the second mirror of the laser cavity (R_1). AR-coatings are used on the front facet of the RSOA and on both facets of the Silicon chip to minimize back-reflections. Tuning of the cavity resonance through the plasma carrier effect corresponds to modulation of the emitted wavelength. (b) Three-dimensional representation of the employed external resonant reflector. A bus waveguide is vertically coupled to a PhC cavity with a pn junction extending in its defect. The red and blue regions represent the n- and p-doped regions of the pn junction.

6.3.2 Tunable Resonant Reflector Fabrication

Although the resonant reflector devices used for the experiments of this chapter were broadly similar to the ones used in Chapters 4 and 5, the inclusion of pn junctions dictated some additional fabrication steps. The complete process flow is presented in this section for completion.

As in all previous cases, the tunable reflector devices were fabricated on the 220 nm SOI platform. The ion implantation process for the creation of the p^+pnn^+ junctions took place in Tyndall National Institute on a wafer scale and the details of each step can be found in Appendix A. The processing begins with a 4-inch SOI wafer being given a CMOS pre-oxidation clean and spin-coated with a 750-nm layer of ZEP 520A. Alignment marks (defining the exact position of the junctions) are patterned on the resist using electron-beam lithography (**Fig. 6.4a**). After developing, dry-etching and stripping of the resist used for e-beam lithography, the wafer is spun with a 1.1-μm thick layer of Fujifilm HiPR6512 positive photoresist. Using the alignment marks as a reference point, ion implantation windows are defined in the appropriate areas of the wafer by projection lithography (**Fig. 6.4b**). The exposed wafer is developed in OPD5262 and ions are implanted in the exposed areas, as described in Section 3.4. The wafer is then stripped from the remaining resist.

The implantation window patterning, the ion implantation, and the wafer cleaning steps are repeated for as many cycles as the number of the different dopants and doses desired. For the pn junctions used in this project, the wafer underwent four doping cycles - p^+, n^+, p and n, in the order mentioned (**Fig. 6.4c**). Boron ions were used for the p^+ and the p-type doping, and Phosphorus ions for the n^+ and n- type doping. The wafer is then annealed at 1050° C for 15 seconds for the activation of the dopants and the formation of the actual junctions. The detailed process flow of the implantation process can be found in Appendix A. Upon the formation of the junctions, the wafer was diced in dies (which will be referred to as samples for convenience). Each sample corresponds to a projection lithography reticule. The subsequent processing of the samples took place in the University of St Andrews on a die scale and the process flow was similar to the one presented in Section 3.2.

The desired pattern (including the PhC cavities) on each sample is exposed on positive electron beam resist (ZEP 520A) using e-beam lithography (**Fig. 6.4d**). A 'three-point alignment' using the aforementioned alignment marks as reference points[3] is employed to ensure that the center of each PhC cavity coincides with the center of the depletion region of each pn junction. As in all previous cases, the Dispersion Adapted (DA) PhC cavity design [12] was employed for this part of the project too. Upon development, the defined pattern is transferred on Silicon by Reactive Ion Etching (RIE) (**Fig. 6.4e**). Following resist stripping and Piranha cleaning, a ~140-nm-thick Spin-on Glass (SOG) cladding layer is spin-coated and hard-baked on top of each sample, filling the holes of the photonic crystal, and the alignment mark regions are 'unmasked' as described in Section 3.2 (**Fig. 6.4f**). In the next step of the process flow, electrical vias are etched into the 140-nm thick SOG layer using photolithography and RIE, and metal

[3] Ultraclean Super-Tack, zero-residue tape is used to ensure that the regions where the alignment marks lie remain 'open'.

contacts are formed by depositing ~300 nm of aluminium (Al) using electron-beam physical vapour deposition (EBPVD) and lift-off, as described in Section 3.7 (**Fig. 6.4g**).

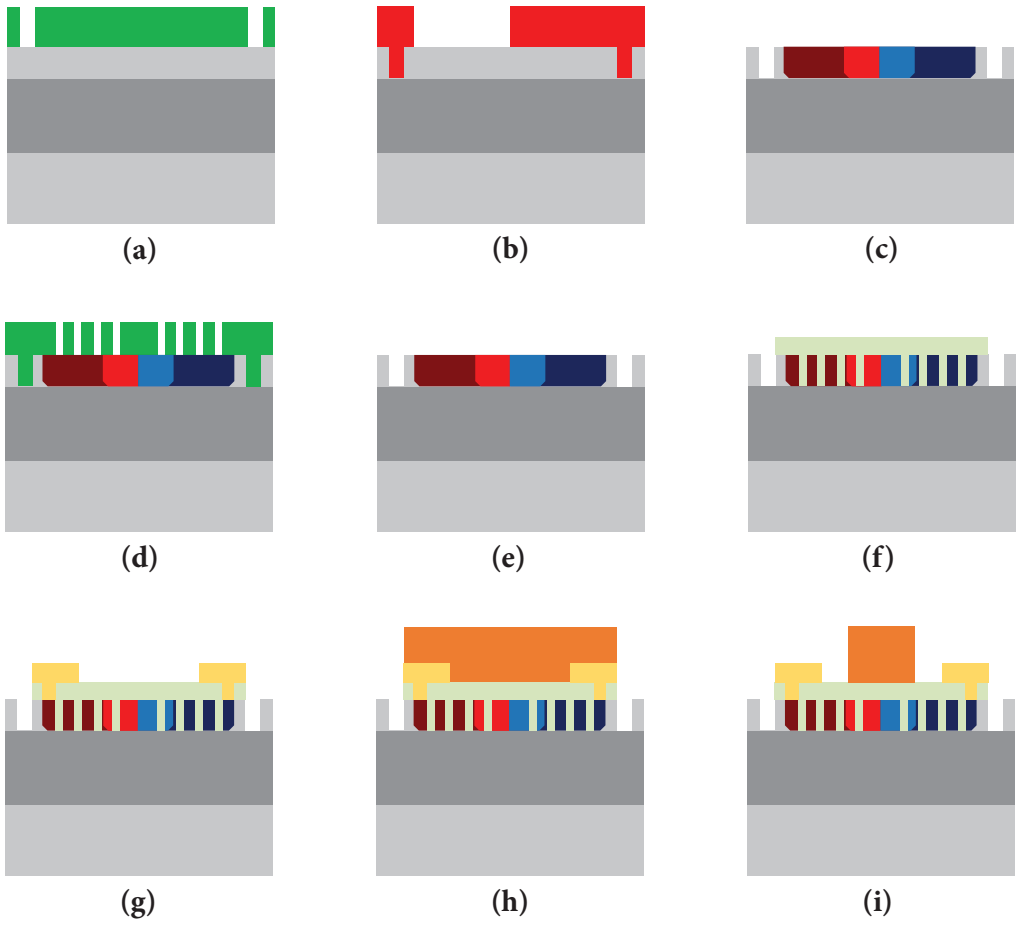

Fig. 6.4 Fabrication process flow of tunable resonant devices: (a) A 4-inch SOI is given a CMOS pre-oxidation clean and is spun with positive e-beam resist – ZEP 520A. Alignment marks are exposed on the resist by e-beam lithography. The wafer is developed in ZED-N50, and ZEP is removed from the exposed regions. Silicon is etched away from the uncovered parts by Reactive Ion Etching (RIE) and the desired pattern is transferred on the Silicon layer of the wafer. The patterned wafer is then stripped from the remaining resist and cleaned. (b) The wafer is spun with positive photoresist – Fujifilm HiPR6512. Ion implantation windows are exposed on the resist by projection lithography. The exposed wafer is developed and ions are implanted in Silicon at the exposed windows. The wafer is then stripped from the remaining resist and cleaned. (c) The implantation widow patterning, ion implantation and wafer cleaning steps (shown in (b)) are repeated for as many cycles as the number of different dopants and doses desired. For the devices used here, the wafers underwent four doping cycles: n^+ (dark blue), p^+ (maroon), n (light blue) and p (red). The wafer is then diced in dies/samples (corresponding to the projection lithography reticules). (d) Each sample is spun with ZEP 520A and the desired pattern (PhC cavities) is exposed on it by e-beam lithography. A 3-point alignment method using the alignment marks is utilized to ensure that the centre of the depletion region of each pn junction would coincide with the centre of each PhC cavity. (e) The sample is developed and the exposed pattern is transferred to Silicon by RIE. The patterned sample is stripped from the remaining resist and cleaned. (f) The sample is clad with SOG and the thickness of the SOG layer is reduced by RIE. (g) Electrical vias are etched through the SOG layer and electrical contacts are formed using lift-off. (h) The alignment-mark parts are covered, and the sample is spun with SU8 polymer. (i) Utilizing a 3-point alignment method, SU8 polymer waveguides are formed by electron-beam lithography and development in EC-solvent.

As a final step of the process, the bus waveguides are fabricated on top of the oxide-clad photonic crystal cavities. As previously, a ~2.1-μm-thick SU8 layer was used for the waveguides in this part of the project, and the areas with the alignment marks are covered with zero-residue tape in order to maintain the marks 'open' (**Fig. 6.4h**). The waveguide design is transferred on the SU8 polymer via e-beam lithography and a 'three-point alignment' is again employed (using the alignment marks on the Silicon layer as reference points) to ensure that that waveguides are located in the desired positions above the cavities. After a 3-minute post-exposure baking at 100 ^{0}C, the waveguides are formed by development in EC solvent (**Fig. 6.4i**). Further details on the above described fabrication steps can be found in Chapter 3 (particularly in Section 3.2). Once all the above steps are completed, the sample is cleaved (typically along a plane perpendicular to the direction of propagation of light in the waveguide) to form a chip with waveguide facets of good optical quality. In order to further reduce facet back-reflections, a ~280nm layer of MgF_2 ($n \approx 1.37$) is deposited by Electron-Beam Physical Vapour Deposition (EBPVD) on both ends of the bus waveguide as an Anti-Reflection (AR) coating, as described in Chapter 3.

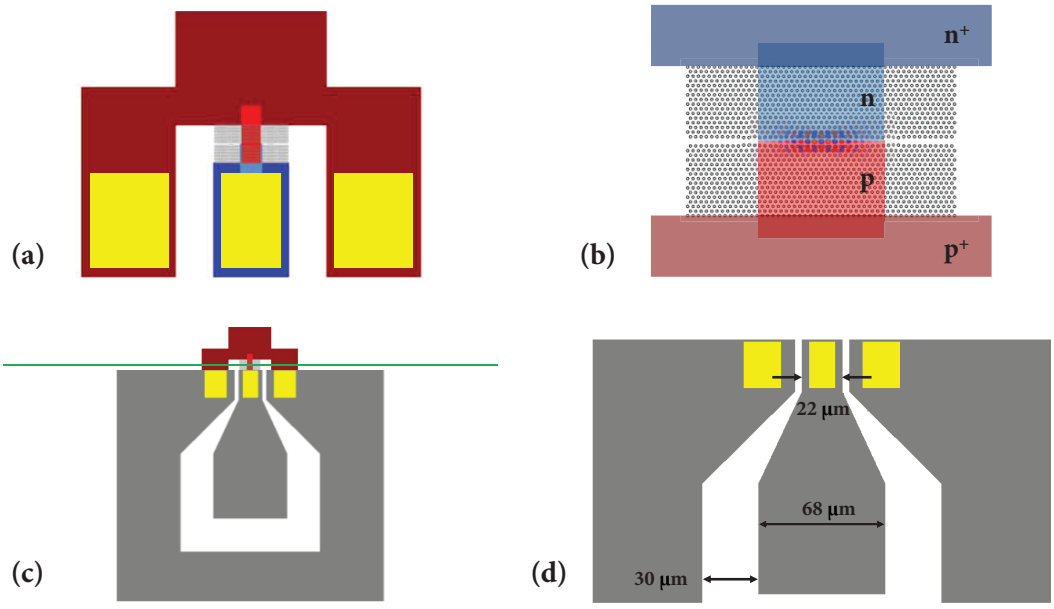

Figure 6.5 (a) Schematic representation of PhC cavity and pn junction. The different doping regions are shown in different colours: p^+ in maroon, n^+ in dark blue, p in red, n in light blue. The electrical vias are shown in yellow. (b) Position of p^+pnn^+ junction relative to the field distribution (*Ey*) of the first order mode of a DA PhC cavity. (c) Complete view of a tunable resonant reflector device. The doping regions are designed to keep the electrical vias and metal electrodes on the same side of the bus waveguide (in green). (d) Position of metal electrodes (in grey) with respect to electrical vias (in yellow).

Fig. 6.5a shows a schematic representation of the position of the doped regions relative to that of the DA PhC cavity, while **Fig. 6.5b** shows the position of the p^+pnn^+ junction relative to that of the optical mode of the cavity. A p^+pnn^+ configuration was selected as it is suitable for both depletion and injection type modulation. The gap between the p^+ and the n^+ regions was chosen to be 10 μm and was occupied by the p- and n-doped regions, each of which was 5 μm long. This design was selected to reduce the contact resistance and the diode resistance, while maximizing the overlap between the optical mode of the cavity and the depletion region of the

junction (**Fig. 6.5b**). At the same time, it can limit the overlap between the high intensity regions of the PhC cavity modes (that mainly lie in the cavity defect – **Fig. 6.5b**) with the highly doped regions (p^+ and n^+), which would result in higher free carrier absorption losses. The doping concentrations for the p^+ and n^+ doped regions were 6×10^{14} cm^{-3} and 3×10^{14} cm^{-3}. Respectively, the dopant density[4] for the p- and n-doped areas was 6×10^{12} and 1×10^{13}. The higher density for the p^+ and the n-doped parts was chosen to compensate for the additional resistance that arises from the larger area of those parts (as seen in **Fig. 6.5a**).

The doping regions were designed to keep all the electrical vias and contact pads on the same side of the bus waveguide (**Fig. 6.5**). In this way, the existence of a contact layer on the bus waveguide is avoided, preventing the severe losses that the metal would introduce in the propagating optical field. Electrical vias (their position can be seen in **Fig. 6.5a**) are opened to help the metal contacts (which otherwise lie on the SOG layer) reach the high-doped regions. The ground electrode covers the vias on the p^+ region, while the central (signal) electrode covers the vias on the n^+ region. The relative position of the windows for electrical vias and electrodes can be seen in **Fig. 6.5d**. The contact pads were arranged to also assist the use of high speed ground-signal-ground (GSG) microwave probes: the electrodes are designed to match a typical pitch (100 μm) of a 50 Ω RF probe, and their width and separation is impedance-matched to a coplanar waveguide transmission line to eliminate reflections of the RF signal (**Fig. 6.5d**).

6.4 Experimental Setup and Characterization

As in all previous parts of the project, the transmission of the active resonant mirror chips used in this part was measured prior to their employment in the experiments of this chapter. For this, the method described in Section 4.3 and the optical setup of **Fig. 4.2a** were used. For the DC characterization of the devices, a Keithley 2450 SourceMeter and a pair of needle probes on SUSS Microtec PH100 probe positioners were added on the existing optical setup (as shown in **Fig. 6.6**). Respectively, for the CW characterization of the compact EC laser cavity, the setup of **Fig. 5.3** was used. During uncooled CW operation, threshold currents as low as 9 mA in the C-band and single mode lasing linewidths < 10 MHz were observed – in agreement with the results presented in Chapter 5.

The diodes of the tunable resonant mirrors were characterized by up-sweeping the bias voltage across the pn junction of each device and measuring the corresponding current flow. An initial voltage sweep up to 12 V was necessary to 'activate' the contacts. Indicative IV curves before and after activation for a device comprising a DA PhC cavity with lattice constant $\alpha = 390$ nm and fill factor $r/\alpha = 0.28$ (r the radius of a hole) and a 5-μm-long pn junction can be seen in **Fig. 6.7a**. Injection type modulation (i.e. forward biasing of the junction) was considered

[4] Even though doping induces free carrier losses, it has been reported that Q-factors of > 40000 can be achieved even with carrier densities of the order of 10^{18} cm^{-3} at the centre of a PhC cavity [29]. It can be thus deduced that the doping densities used here do not significantly deteriorate the performance of the devices.

in the work presented here, therefore IV curves for positive voltages are shown. The observed cut-in voltage is < 1 V (more precisely around 0.7 V), in agreement with typical values for Silicon diodes (~0.6 – 0.7 V). The forward resistance of the junction is relatively high (~15 kΩ), attributed mainly to the high resistance of the metal-Silicon contacts.

The transmission spectra of the above described tunable vertically coupled bus waveguide-Silicon PhC cavity system were measured for different bias voltages. **Fig. 6.7b** shows the resonant wavelength shift (in transmission) as a function of the voltage applied in the pn junction. As a forward biased configuration is used, excess carriers are injected in the depletion region of the junction, reducing the refractive index and causing a blue-shift of the resonant wavelength. However, with the increase of the applied voltage the depletion region of the junction becomes 'thin' enough for its electric field to not be able to prevent charge carrier motion across the junction, resulting in a current flowing through the diode. This current flow increases the local temperature of the junction – and consequently of the centre of the PhC cavity – causing a red-shift of the resonant wavelength, as a result of the thermo-optic effect. These two shifts (blue-shift from carrier injection and red-shift due to current flow) tend to counteract; above some voltage (here ~2 V), the influence of the thermo-optic effect becomes stronger than that of the electro-optic effect (i.e. carrier injection), delivering a net red-shift, as can be seen in **Fig. 6.7b**. The observed wavelength shift was relatively small (with respect to Eq. 6.3), a fact that was attributed to poor device performance (which can be a result of poor pn junction performance or misalignment of the PhC cavity relative to the junction).

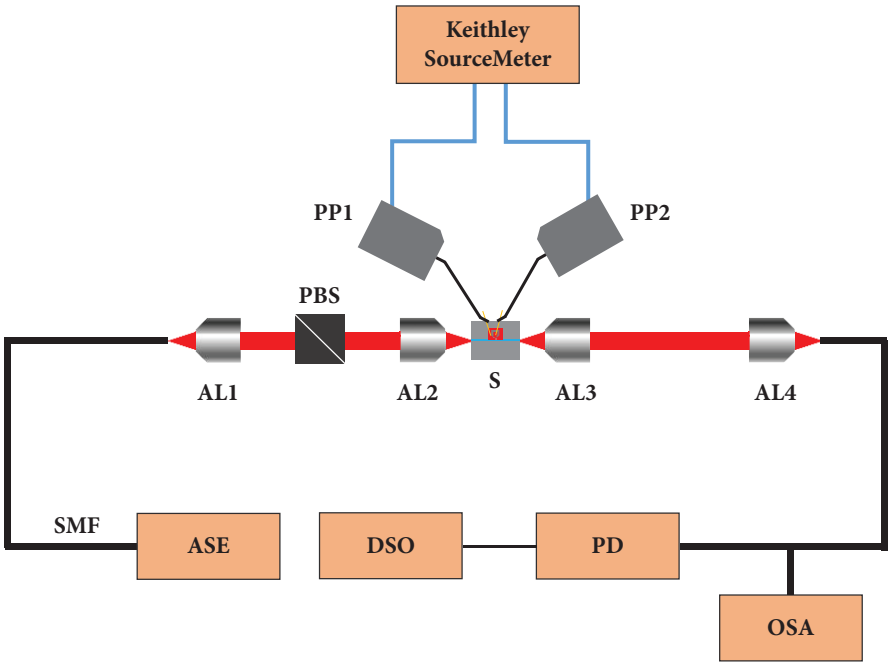

Figure 6.6 (a) Experimental setup for DC characterization of the tunable resonant reflector devices. ASE: amplified spontaneous emission broadband source, AL (1-4): compact aspheric lenses, PBS: polarizing beam splitter, S: silicon chip/tunable photonic crystal cavity based reflector, PP (1-2): probe positioners connected to a Keithley 2450 SourceMeter, DSO: digital sampling oscilloscope, PD: photodetector, OSA: optical spectrum analyser, SMF: single-mode fiber.

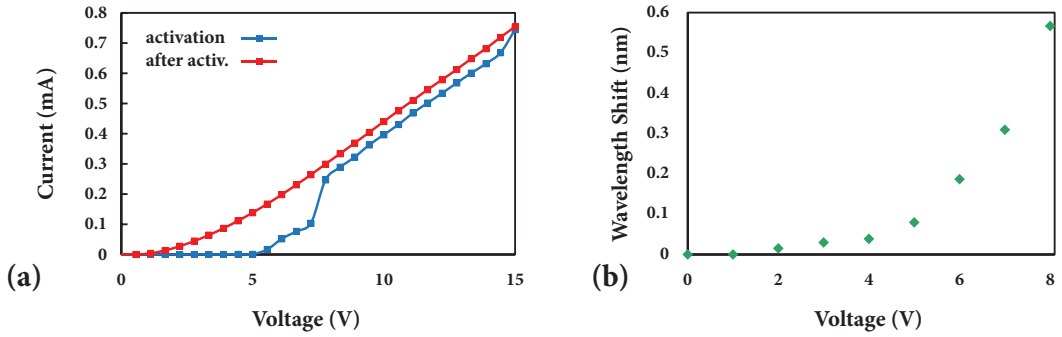

Figure 6.7 (a) 'Activation' IV sweep (blue) and IV curve after contact activation (red), and (b) resonant wavelength shift (in transmission) as a function of bias voltage, for a polymer waveguide vertically coupled to a Silicon DA PhC cavity with lattice constant α = 390 nm and fill factor r/α = 0.28, embedded in a pn junction.

6.4.1 Direct Frequency Modulation

For the demonstration of the suitability of the examined configuration for direct frequency modulation, the emitted wavelength of an EC laser device comprising the aforementioned 'active' resonant reflector was modulated through tuning the resonant wavelength of the PhC cavity on the Silicon chip. The (injection type) modulation of the PhC cavity resonance was achieved by forward biasing the pn junction in which the cavity is embedded and varying the applied voltage. A sine wave-function generated by a signal generator was used to drive the PhC cavity, and the electrical signal was applied to the metal contacts of the resonant reflector device by a pair of needle probes on SUSS Microtec PH100 probe positioners. An additional DC bias (provided by a power supply) was added via a bias T. The schematic of the complete laser cavity and of the equipment used for its modulation can be seen in **Fig. 6.8a**, while **6.8b** shows a microscope image of the compact EC laser cavity with a tunable PhC cavity-based resonant reflector.

The EC laser drive current was kept constant at 30 mA (corresponding to single mode operation with a SMSR > 46 dB) and a forward DC bias of V_{DC} = 2.6 V was used. The emission of the laser was collected with a lensed fiber at the output of the Silicon reflector chip (as for the experiments of Chapter 5), and heterodyne detection was employed for the observation of the frequency modulation of the device under study. The setup of the heterodyne measurement can be seen in **Fig. 6.8c**. Similar to the case of the self-heterodyne linewidth measurement described in Chapter 5, for the heterodyne detection, the modulated output of the studied laser is superimposed with the output of a narrow-linewidth tunable laser, which is tuned to match the central emitted wavelength of the laser under study (i.e. the emitted wavelength at V_{DC} – here V_{DC} = 2.6 V), and the resulting interference pattern is recorded using a fast Digital Sampling Oscilloscope (DSO). As the outputs of the two lasers are uncorrelated, the tunable laser acts as a frequency reference and the bandwidth of the obtained beat note corresponds to the modulation bandwidth of the output of the studied laser (i.e. the frequency/wavelength shift of the modulated laser above and below a central reference frequency).

For the measurements during this project, the output of the examined directly modulated compact EC laser (as shown in **Fig. 6.8a**) was combined with the output of a 'reference'

narrow-linewidth (<300 kHz) tunable laser at a 3x3 fiber-optic splitter. The reference laser was tuned to match the central emitted wavelength of the EC laser (i.e. the emitted wavelength at V_{DC} = 2.6 V) at 1545.57 nm. Their beating was observed at the output of the splitter using a Thorlabs Power Meter (PM), a fast (100 GS/s, 33 GHz) digital sampling oscilloscope (DSO) and an optical spectrum analyser (OSA).

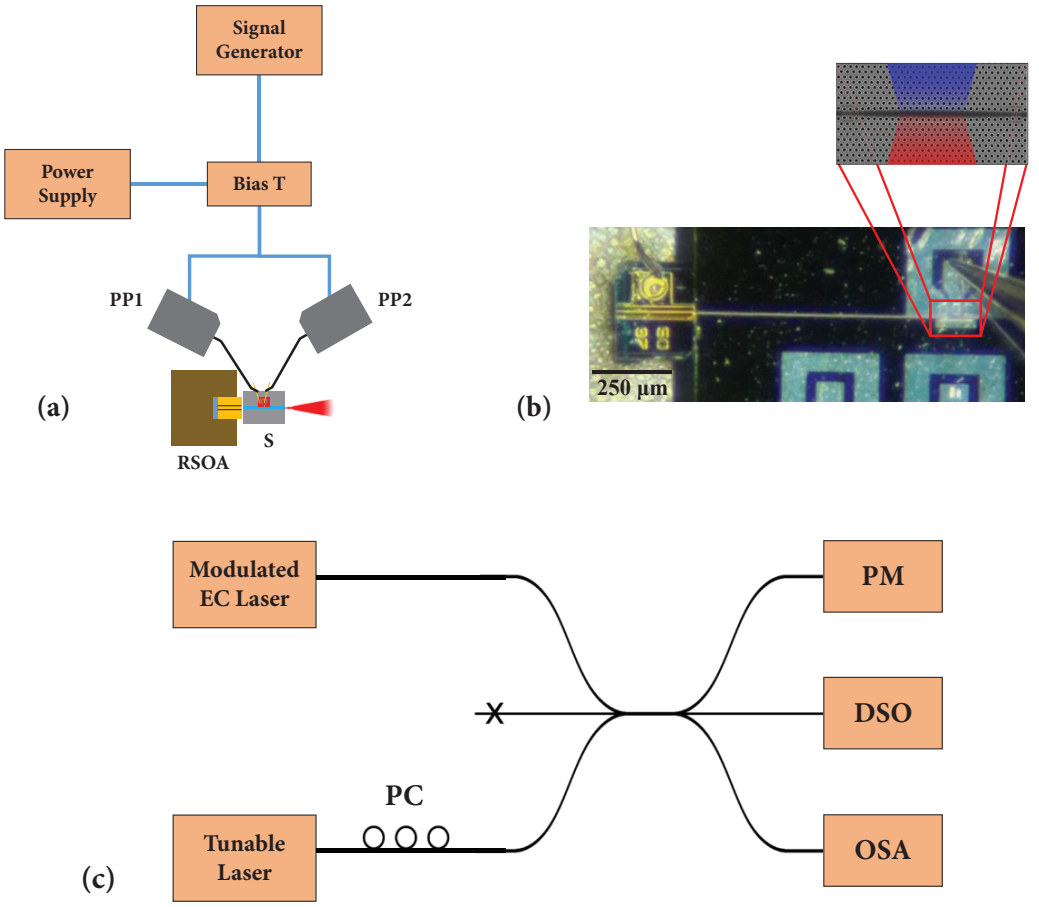

Figure 6.8 (a) Schematic representation of compact EC configuration for direct frequency modulation and experimental equipment for the modulation of the resonant wavelength of the PhC cavity. A signal generator and needle probes on probe positioners (PP1 and PP2) were used to drive the pn junction on the Silicon reflector chip. A DC bias was added with a bias T. (b) Top-view microscope image of compact EC laser device for direct frequency modulation. An overhanging RSOA chip (250 µm long) on mount is butt-coupled to the external reflector Silicon chip, comprising a polymer SU8 waveguide vertically coupled to a Dispersion Adapted (DA) photonic crystal cavity that is embedded in a pn junction. The tips of the needle probes used to apply the driving voltage can be seen on the metal electrodes. The inset shows a SEM image of a DA PhC cavity: the blue and red regions indicate the p- and n-doped regions of the pn junction. (c) Setup used for heterodyne detection. The output of the studied modulated EC laser (as shown in (a)) is combined at a 3x3 fiber-optic splitter with the output of a tunable laser that is tuned to match the central emitted wavelength of the EC laser (i.e. the emitted wavelength at the DC bias voltage, V_{DC}). Their beat note is observed using a power meter (PM), a fast digital sampling oscilloscope (DSO) and an optical spectrum analyser (OSA). A fiber-optic polarization controller (PC) is used to ensure that the two beam parts maintain the same polarization.

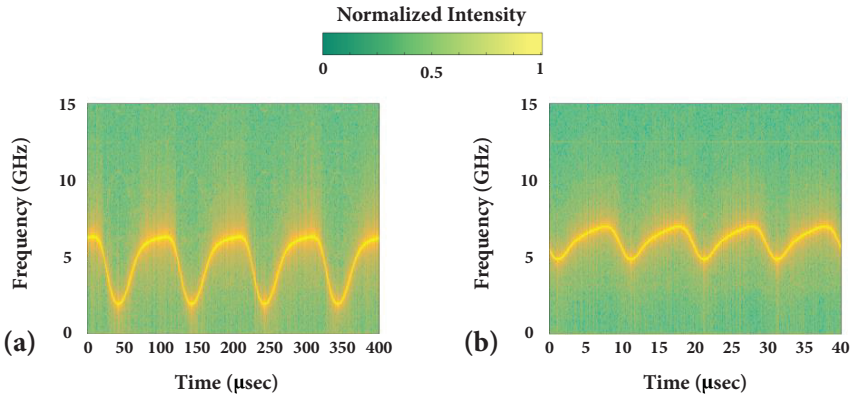

Figure 6.9 Heterodyne detection of the frequency modulation of the output of the compact EC configuration examined in this chapter by a sine waveform with frequency (a) 10 kHz (corresponding to a frequency shift $\Delta\nu$ = 4.3 GHz), and (b) 100 kHz (corresponding to a frequency shift $\Delta\nu$ = 2.2 GHz).

A peak-to-peak voltage V_{pp} = 4 V was used. **Fig. 6.9a** and **6.9b** show the heterodyne spectra of the modulated EC laser for a sine waveform frequency of 10 kHz and 100 kHz (0.1MHz). The corresponding frequency bandwidths of the output signal were $\Delta\nu$ = 4.3 GHz (i.e. $\Delta\lambda$ = 34.5 pm) and $\Delta\nu$ = 2.2 GHz (i.e. $\Delta\lambda$ = 17.6 pm), respectively. A further increase of the frequency of the driving sine waveform resulted in an even smaller frequency shift of the wavelength emitted by the studied EC laser. In carrier injection schemes, modulation frequency limitations typically arise by the free carrier lifetime in the depletion region of the pn junction. However, as discussed in Chapter 5, the photon lifetime in oxide clad cavities is of the order of 100s of picoseconds [30], corresponding to modulation speeds of a few GHz. It can thus be inferred that the modulation speed of the device examined here is not fundamentally limited by the optical design (i.e. the employed PhC cavity); the speed limitations can be attributed to a combination of the electrical setup/design used (e.g. impedance mismatch and high electrical signal reflections due to the use of needle probes) and the poor device performance (pn junction misalignment with respect to the centre of the PhC cavity and high contact resistance – both are issues that can be very easily overcome in a CMOS fabrication facility). The AC power consumed for the modulation of the EC laser is given by $P_{AC} = V_{rms}^2/R$, where V_{rms} is the root mean square voltage of the driving signal. Given that the driving wave-function employed here is sinusoidal, $V_{rms} = V_{pp}/\ 2\sqrt{2}$. For V_{pp} = 4 V and R = 15 kΩ, the AC power consumption is 133 μW or ~1.33 nJ/bit for a modulation frequency of 100 kHz. The total power consumed for the modulation of the examined EC laser (including the 2.6 V of the DC bias) is ~247 μW. The high power consumption results from the high resistance of the current device and the impedance mismatch due to the use of needle probes.

6.5 Discussion

In this chapter, I have explored the potential of the EC laser design examined in this thesis for direct frequency modulation. Similarly to the configuration presented in Chapter 5, the laser cavity used here consisted of a 250-μm long III-V RSOA die on submount and a Silicon resonant

reflector with a bus waveguide vertically coupled to a PhC cavity that was embedded in a pn junction. As in all the previous parts of this project, a combination of SU8 polymer waveguides and Dispersion Adapted (DA) PhC cavities [12] was used on the resonant reflector chips here. The CW functionality and performance of the examined EC laser devices were in good agreement with the results presented in Chapter 5.

As the emitted wavelength in the design discussed in this project is dependent on only the resonance of the PhC cavity on the reflector chip, direct frequency modulation of the laser was achieved through tuning of the resonant wavelength of the DA cavity. The chosen mechanism for that was the carrier dispersion effect, which was implemented by injection type modulation of the pn junction that the PhC cavity was embedded in. Direct frequency modulation of the examined EC laser at modulation speeds up to 100 kHz (limited by the employed electrical setup and the device performance) was achieved by forward biasing of the diode on the resonant reflector with a peak-to-peak voltage of V_{pp} = 4 V and a DC bias voltage of V_{DC} = 2.6 V, for a constant RSOA drive current of 30 mA.

In addition to the advantages of the proposed EC configuration that were discussed in Chapter 5 (Section 5.4), the potential for direct modulation through tuning of the resonant reflector offers a solution to the wavelength matching problem (if appropriately combined with resonant detection, as described in Section 6.1) and paves the way to the less-complicated employment of resonant modulation in practical applications[5]. Even though the modulation performance demonstrated here is not optimal (low speed and high total power consumed), the possibility for modulation of the employed vertically coupled bus waveguide-PhC cavity system of the resonant reflector at much higher frequencies (up to 1 Gbps) and much lower consumed power levels (P_{AC} = ~0.6 fJ/bit) has already been presented in [13]. The use of a PhC cavity as the tunable element of the examined laser architecture is particularly advantageous: owing to their high finesse, PhC cavities can combine ultra-small footprint and narrow resonance linewidth, with large FSR. In this way, lower capacitances (i.e. lower switching energies), and higher channel scalability and density can be achieved with this architecture, as compared to configurations utilizing other types for resonant reflectors (e.g. ring resonators or Bragg gratings). Moreover, the studied in this chapter EC laser can be integrated with active and passive components demonstrated in the vertically coupled platform [13, 31, 32] for the realization of more complex power-efficient Silicon Photonics systems. For all the aforementioned reasons, the proposed scheme is an appealing solution for WDM operation in optical interconnects.

6.6 Improvements and Future Work

The work presented in this chapter – and in general in this thesis – was primarily aiming at exploring and demonstrating the potential of using the vertically coupled bus waveguide-PhC cavity system as a resonant reflector for an EC laser design that would be suitable for direct frequency modulation. As a result, a number of features are still open to further investigation and

[5] As it simplifies the control software and electronic circuitry required otherwise.

optimization. In this section, I discuss some relevant research topics that can be undertaken in the future.

6.6.1 Optimization of Direct Frequency Modulation

As described earlier in this chapter, a pair of needle probes was used to apply the modulated electrical signal to the metal contacts of the tunable resonant mirror in the examined EC laser architecture. As a result, the modulation speed was limited due to performance restrictions and impedance mismatch. To overcome this issue, the experiments described in Section 6.4 could be repeated using a high speed ground-signal-ground (GSG) microwave probe (especially given that the contact electrodes are designed to match the impedance of a coplanar waveguide transmission line). The employed electrical design could also be improved by reducing the contact resistance (e.g. through multilayer contacts [33] or through using a passivation layer at the metal-Silicon interface [34, 35, 36]).

Moreover, a further increase of the modulation speed can be achieved by considering depletion type modulation of the resonant wavelength of the PhC cavity on the reflector chip. In such a scheme, the pn junction that the PhC cavity is embedded in is reverse-biased and the change in the refractive index occurs through the depletion of the excess free carriers in the (depletion region of the) junction. It has already been reported that the carrier density change needed for frequency shifts equivalent to the ones reported here ($\Delta\nu$ = 2.5 – 4.5 GHz) can easily be obtained in a depletion type modulation configuration [37]. For operation in the carrier depletion mode, the modulation power consumption is only determined by the switching energy of the device [38], the values of which are anticipated to be of sub-fJ/bit order for the employed vertically coupled system [37]. Even though the selected for this project pn diode configuration (p^+pnn^+) is in principle suitable for depletion type modulation, the direct frequency modulation of the studied EC laser architecture in depletion mode was severely limited by the quality of the tunable resonant reflectors. More specifically, the poor performance (in terms of achieved refractive index change Δn) in reverse bias, in combination with the relatively large linewidth (>150 pm) of the PhC cavities on the employed tunable Silicon mirrors, resulted in changes of the PhC cavity phase contribution that were not sufficient for considerable shifts in the emitted wavelength to be observed (according to Section 6.3.1 and Eq. 6.5).

In addition to the employed p^+pnn^+ junction design, an interdigitated junction scheme can be considered for depletion type modulation. A schematic representation of the two diode designs relative to a DA PhC cavity is given in **Fig. 6.10**. The interdigitated design allows a larger overlap of the depletion region of the junction with the optical mode of the PhC cavity (due to the topology of the p- and n-doped regions, as shown in **Fig. 6.10b**) and is thus less sensitive to misalignment during the fabrication than the simple pn design (shown if **Fig. 6.10a**). Through the above described considerations, Gbps direct frequency modulation of the examined EC laser architecture can be achieved at an ultra-low power budget.

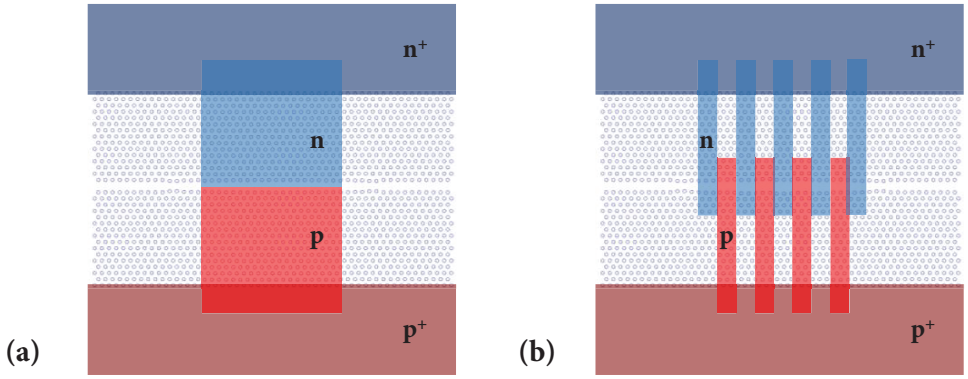

Figure 6.10 Pn junction designs (relative to a DA PhC cavity) suitable for depletion type modulation: (a) pn (p^+pnn^+) junction used for the work described here, and (b) interdigitated pn junction.

6.6.2 Improvement of the Compact EC Configuration

The performance of the compact EC laser configuration presented in Chapters 5 and 6 can be improved in terms of mode selectivity, side-mode suppression ratio (SMSR), and lasing wavelength stability by further minimizing the effect of the modes of parasitic cavities formed due to facet-reflections (as discussed in Sections 2.5 and 5.2.2). This can be achieved by an improvement of the AR coatings on the chip facets (e.g. use of mutli-layer AR coatings on the

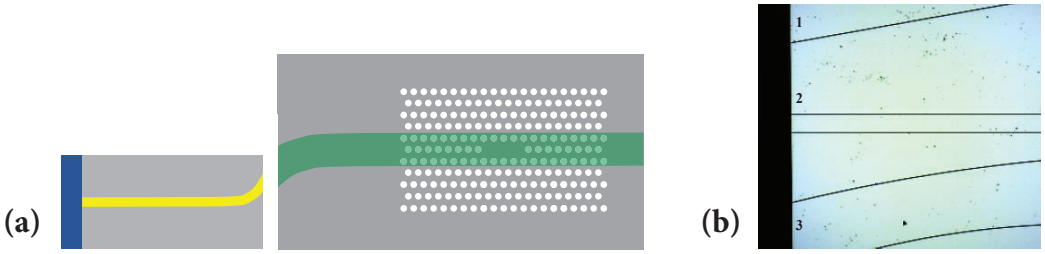

Figure 6.11 (a) RSOA with a waveguide bent at the front facet butt-coupled to external vertically coupled waveguide-PhC cavity reflector with waveguide bent at the insertion facet. (b) Microscope image of angled (1), straight (2) and bent (3) SU8 polymer waveguides on SiO_2 substrate.

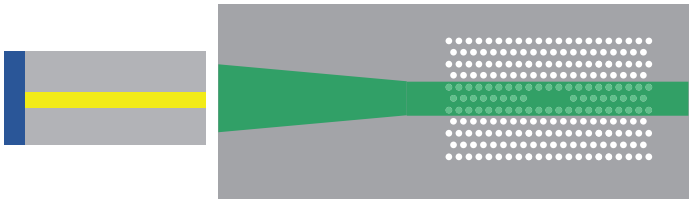

Figure 6.12 Compact EC laser configuration comprising an RSOA butt-coupled to an external vertically coupled waveguide-PhC cavity reflector with a taper section at the insertion facet of the bus waveguide.

Silicon reflector chip, as described in Section 3.7.2) or through the use of alternative laser cavity designs (e.g. use of angled or bent waveguides that would minimize back-reflections [39, 40] – schematic representation in **Fig. 6.11**).

In addition to the aforementioned alterations, the potential to further enhance the examined in this project compact EC laser architecture can be explored through the use of a taper section at the insertion end of the bus waveguide (**Fig. 6.12**), which would reduce its sensitivity to misalignment (according to Section 5.3.2). Finally, the Dispersion Adapted (DA) PhC cavity design [12] was used for the experimental demonstrations presented in this thesis, due to its large fabrication tolerance and its good mode overlap with the employed low index bus waveguides. However, DA PhC cavities do not exhibit the highest possible FSR, resulting in mutli-modal behaviour. The use of alternative PhC cavity designs with single-mode operation or much higher FSR (e.g. line defect modulated cavity [41] or double heterostructure cavity [42]) can be considered on the Silicon-based resonant reflector, for the demonstration of scalability with the proposed EC laser configuration, and for avoiding undesired lasing from higher order PhC cavity modes (as discussed in Chapter 4). The suitability of the line defect modulated PhC cavity for the vertically coupling platform has already been demonstrated in [37].

6.6.3 Bonding and EC Laser Arrays

Another direction that can be explored with the compact EC laser configuration studied in this project is the potential for practical III-V/Silicon integration. In the considered EC architecture, Si/III-V integration can be achieved by butt-coupling via flip-chip bonding [43, 44, 45, 46]. Using this technology, the RSOA chip can be bonded with metallic solder onto the Silicon substrate of the SOI reflector chip after partly removing the top Silicon and buried oxide (BOx) layers, as shown in **Fig. 6.13**. Compared to the wafer- or die-bonding technologies [47, 48, 49, 50] that have emerged as alternative candidates for III-V integration on Silicon, the main advantage of a chip bonding configuration is the higher flexibility in the independent design and

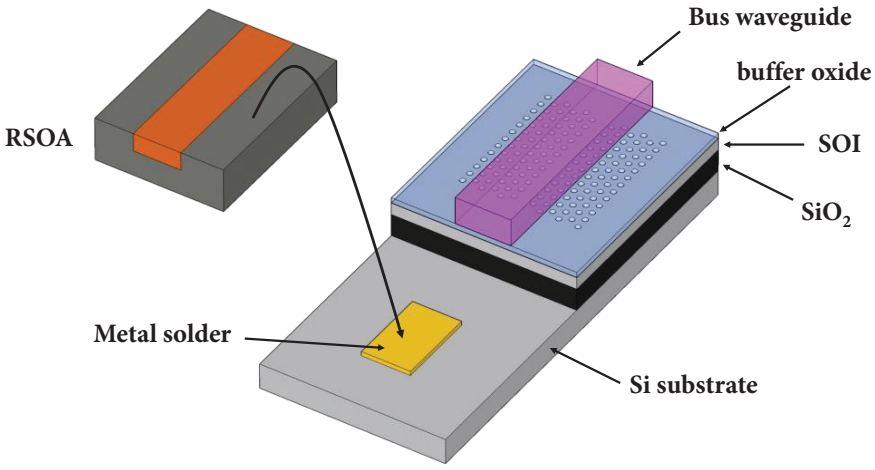

Figure 6.13 Conceptual representation of the chip bonding integration of the III-V RSOA chip on the SOI-based reflector chip for the formation of the discussed EC laser.

optimization for higher yield of the Silicon and RSOA chips. Additionally, it can allow better thermal conductance between the III-V chip and the substrate (i.e. better RSOA heat dissipation to the substrate), which is a favourable characteristic for transmitters that operate at high temperatures. Flip-chip bonding technology can be used to bond the III-V-based RSOA dies onto the Silicon substrate of either passive or active SOI resonant reflector chips, resulting in integrated versions of the compact EC laser configurations presented in Chapters 5 (CW operation) and 6 (directly modulatable), respectively.

Further to that, the demonstration of arrays of the EC laser design proposed in Chapters 5 and 6 should be examined. Similar to the configurations presented in [45, 46], such laser arrays can be obtained by butt-coupling an RSOA array to a Silicon chip with an array of resonant reflector devices (**Fig. 6.14**), significantly reducing the footprint per channel and the aggregate output power (or potentially the aggregate modulation speed). Ultimately, all the aforementioned techniques can be combined and along with previous demonstrations of passive and active components on the vertically coupled platform [13, 31, 32, 51] be used for the demonstration of a complete low-power-consumption (aiming to sub-100 fJ/bit power budgets) Silicon Photonic interlink.

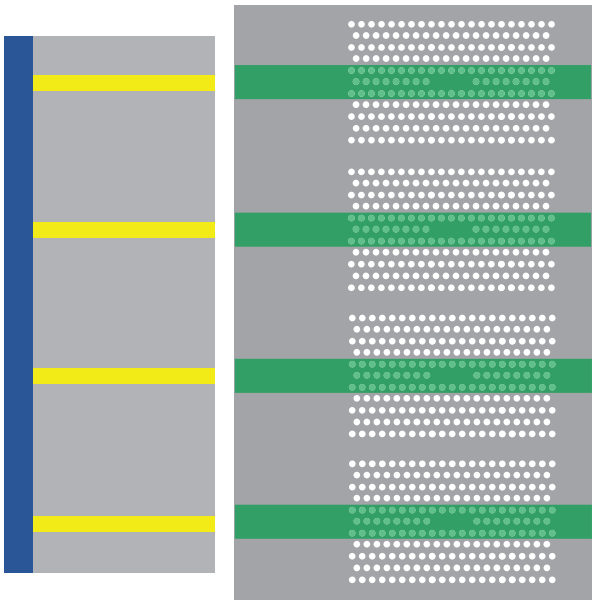

Figure 6.14 Compact EC laser array configuration comprising a 4-channel RSOA array butt-coupled to a Silicon chip with an array of four resonant reflectors based on a vertically coupled bus waveguide-PhC cavity system.

References

[1] Z. Zhou, B. Yin and J. Michel, "On-chip light sources for silicon photonics," *Light: Science & Applications* , vol. 4, pp. e358:1-13, NOV 2015.

[2] H. Liu, C. F. Lam and C. Johnson, "Scaling Optical Interconnects in Datacenter Networks Opportunities and Challenges for WDM," in *2010 IEEE 18th Annual Symposium on High Performance Interconnects (HOTI)*, Mountain View, CA, AUG 2010.

[3] A. Ghiasi, "Large data centers interconnect bottlenecks," *Optics Express,* vol. 23, no. 3, pp. 2085-2090, JAN 2015.

[4] M. Haurylau, G. Chen, H. Chen, J. Zhang, N. A. Nelson, D. H. Albonesi, E. G. Friedman and P. M. Fauchet, "On-Chip Optical Interconnect Roadmap: Challenges and Critical Directions," *IEEE Journal of Selected Topics in Quantum Electronics,* vol. 12, no. 6, pp. 1699-1705, NOV-DEC 2006.

[5] Z. Li, I. Shubin and X. Zhou, "Optical interconnects: recent advances and future challenges," *Optics Express,* vol. 23, no. 3, pp. 3717-3720, FEB 2015.

[6] T. Tekin, N. Pleros, R. Pitwon and A. Hakansson, Optical Interconnects for Data Centers, Woodhead Publishing, NOV 2016.

[7] M. Haurylau, H. Chen, J. Zhang, G. Chen, N. A. Nelson, D. H. Albonesi, E. G. Friedman and P. M. Fauchet, "On-chip optical interconnect roadmap: challenges and critical directions," in *2nd IEEE International Conference on Group IV Photonics, 2005*, Antwerp, BE, SEP 2015.

[8] I. S. Amiri, A. Afroozeh and H. Ahmad, Integrated Micro-Ring Photonics: Principles and Applications as Slow Light Devices, Soliton Generation and Optical Transmission, CRC Press, 2016.

[9] G. T. Reed, Silicon Photonics: The State of the Art, Chichester, UK: John Wiley & Sons Ltd, APR 2008.

[10] J. A. Cox, A. L. Lentine, D. J. Savignon, D. C. Trotter and A. L. Starbuck, "Wavelength control of resonant photonic modulators with balanced homodyne locking," in *2014 Conference on Lasers and Electro-Optics (CLEO)*, San Jose, CA, DEC 2014.

[11] W. A. Zortman, A. L. Lentine, D. C. Trotter and M. R. Watts, "Bit-Error-Rate Monitoring for Active Wavelength Control of Resonant Modulators," *IEEE Micro,* vol. 33, no. 1, pp. 42-52, OCT 2012.

[12] K. Welna, S. L. Portalupi, M. Galli, L. O'Faolain and T. F. Krauss, "Novel Dispersion-Adapted Photonic Crystal Cavity with Improved Disorder Stability," *IEEE Journal of Quantum Electronics,* vol. 48, no. 9, pp. 1177-1182, SEP 2012.

[13] K. Debnath, L. O'Faolain, F. Y. Gardes, A. Steffan, G. T. Reed and T. F. Krauss, "Cascaded modulator architecture for WDM applications," *Optics Express,* vol. 20, no. 25, pp. 27420-27428, DEC 2012.

[14] T. Akiyama, S. Tanaka, T. Kurahashi, H. Ebe and S. Sekiguchi, "A novel transmitter leveraging high-speed ultralow-power modulation of a Si microring modulator by eliminating tuning power," in *Optical Fiber Communications Conference and Exhibition (OFC), 2016*, Anaheim, CA, MAR 2016.

[15] D. Liang, X. Huang, G. Kurczveil, M. Fiorentino and R. G. Beausoleil, "Integrated finely tunable microring laser on silicon," *Nature Photonics,* vol. 10, pp. 719-722, SEP 2016.

[16] M. Notomi, K. Nozaki, A. Shinya, M. Shinji and K. Eiichi, "Toward fJ/bit optical communication in a chip," *Optics Communications,* vol. 314, pp. 3-17, MAR 2014.

[17] D. A. B. Miller, "Energy consumption in optical modulators for interconnects," *Optics Express,* vol. 20, no. S2, pp. A293-308, MAR 2012.

[18] T. Tanabe, K. Nishiguchi, E. Kuramochi and M. Notomi, "Low power and fast electro-optic silicon modulator with lateral pin embedded photonic crystal nanocavity," *Optics Express,* vol. 17, no. 25, pp. 22505-22513, DEC 2009.

[19] K. Nozaki, T. Tanabe, A. Shinya, S. Matsuo, T. Sato, H. Taniyama and M. Notomi, "Sub-femtojoule all-optical switching using a photonic-crystal nanocavity," *Nature Photonics,* vol. 4, pp. 477-483, MAY 2010.

[20] O. Painter, A. Husain, A. Scherer, P. T. Lee, I. Kim, J. D. O'Brien and P. D. Dapkus, "Lithographic tuning of a two-dimensional photonic crystal laser array," *IEEE Photonics Technology Letters,* vol. 12, no. 9, pp. 1126-1128, SEP 2000.

[21] A. A. Liles, A. P. Bakoz, A. A. Gonzalez-Fernandez, T. Habruseva, G. Huyet, S. P. Hegarty and L. O'Faolain, "Compact III-V/Silicon External Cavity Laser Configuration with Photonic Crystal Cavity Reflector for Direct Frequency Modulation," in *13th International Conference on Group IV Photonics (GFP)*, Shanghai (CN), 2016.

[22] R. A. Soref and B. R. Bennett, "Kramers Kronig analysis of electro-optical switching in silicon," in *Proceedings of SPIE, Integrated Optical Circuit Engineering IV, 32*, Cambridge, MA, MAR 1987.

[23] R. A. Soref and B. R. Bennett, "Electrooptical Effects in Silicon," *IEEE Journal of Quantum Electronics,* vol. 23, no. 1, pp. 123-129, JAN 1987.

[24] G. T. Reed and C. E. Png, "Silicon Optical Modulators," *Materials Today,* vol. 8, no. 1, pp. 40-50, JAN 2005.

[25] Q. Xu, B. Schmidt, J. Shakya and M. Lipson, "Cascaded silicon micro-ring modulators for WDM optical interconnection," *Optics Express,* vol. 14, no. 20, pp. 9430-9435, OCT 2006.

[26] D. J. Thompson, F. Y. Gardes, J.-M. Fedeli, S. Zlatanovic, Y. Hu, B. P. P. Kuo, E. Myslivets, N. Alic, S. Radic, G. Z. Mashanovich and G. T. Reed, "50 Gb/s silicon optical modulator," *IEEE Photonics Technology Letters,* vol. 24, no. 4, pp. 234-236, FEB 2012.

[27] H. Xu, X. Li, X. Xiao, Z. Li, Y. Yu and J. Yu, "Demonstration and Characterization of High-Speed Silicon Depletion-Mode Mach–Zehnder Modulators," *IEEE Journal of Selected Topics in Quantum Electronics,* vol. 20, no. 4, p. 3400110, JUL 2014.

[28] J. M. Shainline, J. S. Orcutt, M. T. Wade, K. Nammari, B. Moss, M. Georgas, C. Sun, R. J. Ram, V. Stojanović and M. Popović, "Depletion-mode carrier-plasma optical modulator in zero-change advanced CMOS," *Optics Letters,* vol. 38, no. 15, pp. 2657-2659, AUG 2013.

[29] P. Cardile, G. Frannzò, R. Lo Savio, M. Galli, T. F. Krauss, F. Priolo and L. O'Faolain, "Electrical conduction and optical properties of doped silicon-on-insulator photonic crystals," *Applied Physics Letters,* vol. 98, no. 20, pp. 203506:1-3, MAR 2011.

[30] L. O'Faolain, D. M. Beggs, T. P. White, T. Kampfrath, K. Kuipers and T. F. Krauss, "Compact Optical Switches and Modulators Based on Dispersion Engineered Photonic Crystals," *IEEE Photonics Journal,* vol. 2, no. 3, pp. 404-414, APR 2010.

[31] K. Debnath, F. Y. Gardes, A. P. Knights, G. T. Reed, T. F. Krauss and L. O'Faolain, "Dielectric waveguide vertically coupled to all-silicon photodiodes operating at telecommunication wavelengths," *Applied Physics Letters,* vol. 102, p. 171106, APR 2013.

[32] K. Debnath, R. Moore, A. Liles and L. O'Faolain, "Toolkit for photonic integrated circuits based on inverted rib waveguides," *Journal of Lightwave Technology,* vol. 33, no. 19, pp. 4145-4150, AUG 2015.

[33] L. Vivien and L. Pavesi, Handbook of Silicon Photonics, Boca Raton: CRC Press, Taylor & Francis Group , 2013.

[34] M. Eizenberg and S. P. Murarka, "Forming low-resistance contact to silicon". US Patent US4502209 A, 5 MAR 1985.

[35] E. Timurdogan, C. M. Sorace-Agaskar, J. Sun, E. Shah Hosseini, A. Biberman and M. R. Watts, "An ultralow power athermal silicon modulator," *Nature Communications,* vol. 5, pp. 4008:1-11, JUN 2014.

[36] J. G. Zhu, X. L. Yang and M. Tao, "Low-resistance titanium/n-type silicon (1 0 0) contacts by monolayer selenium passivation," *Journal of Physics D: Applied Physics,* vol. 40, pp. 547-550, JAN 2007.

[37] K. Debnath , "Doctoral Thesis: Photonic Crystal Cavity Based Architecture for Optical Interconnects," The University of St Andrews, St Andrews, APR 2013.

[38] L. Chen, K. Preston, S. Manipatruni and M. Lipson, "Integrated GHz silicon photonic interconnect with micrometer-scale modulators and detectors," *Optics Express,* vol. 17, no. 17, pp. 15248-15256, Aug 2009.

[39] A. Zilkie, P. Seddighian, B. J. Bijlani, W. Qian, D. C. Lee, S. Fatholoumi, J. Fong, R. Shafiiha, D. Feng, B. J. Luff, X. Zheng, J. E. Cunningham, A. V. Krishnamoorthy and M. Asghari, "Power-Efficient III-V/Silicon external cavity DBR lasers," *Optics Express,* vol. 20, no. 21, pp. 23456-23462, OCT 2012.

[40] J.-H. Lee, I. Shubin, J. Yao, J. Bickford, Y. Luo, S. Lin, S. S. Djordjevic, H. D. Thacker, J. E. Cunningham, K. Raj, X. Zheng and A. V. Krishnamoorthy, "High power and widely tunable Si hybrid external-cavity laser for power efficient Si photonics WDM links," *Optics Express,* vol. 22, no. 7, pp. 7678-7685, MAR 2014.

[41] E. Kuramochi, M. Notomi, S. Mitsugi, A. Shinya, T. Tanabe and T. Watanabe, "Ultrahigh Q Photonic Crystal Nanocavities Realized by the Local Width Modulation of a Line Defect," *Applied Physics Letters,* vol. 88, p. 041112, 2006.

[42] B.-S. Song, S. Noda, T. Asano and Y. Akahane, "Ultra-high-Q Photonic Double-Heterostructure Nanocavity," *Nature Materials,* vol. 4, pp. 207-210, 2005.

[43] S. Tanaka, S.-H. Jeong, S. Sekiguchi, T. Kurahashi, Y. Tanaka and K. Morito, "HIgh-output power, single-wavelength silicon hybrid laser using precise flip-chip bonding technology," *Optics Express,* vol. 20, no. 27, pp. 28057-28069, DEC 2012.

[44] N. Fujioka, T. Chu and M. Ishizaka, "Compact and low power consumption hybrid integrated wavelength tunable laser module using silicon waveguide resonators," *Journal of Lightwave Technology,* vol. 28, no. 21, pp. 3115-3120, SEP 2010.

[45] T. Shimizu, N. Hatori, M. Okano, M. Ishizaka, Y. Urino, T. Yamamoto, M. Mori, T. Nakamura and Y. Arakawa, "High density hybrid integrated light source with a laser diode array on a silicon optical waveguide platform for inter-chip optical interconnection," in *IEEE Group IV Photonics*, London, 2011.

[46] F. E. Doany, R. A. Budd, L. Schares, T. N. Huynh, M. G. Wood, D. M. Kuchta, N. Dupuis, C. L. Schow, B. G. Lee, M. Moehrle, A. Sigmund, W. Rehbein, T. Y. Liow, L. W. Luo and G. Q. Lo, "A Four-Channel Silicon Photonic Carrier with Flip-Chip Integrated Semiconductor Optical Amplifier (SOA) Array Providing >10-dB Gain," in *IEEE 66th Electronic Components and Technology Conference* , Las Vegas, Nevada, USA, 2016.

[47] H. Park, M. Sysak, H. Chen, A. Fang, D. Liang, L. Liao, B. Koch, J. Bovington, Y. Tang, K. Wong, M. Jacob-Mitos, R. Jones and J. Bowers, "Device and integration technology for

silicon photonic transmitters," *IEEE Journal of Selected Topics in Quantum Electronics,* vol. 17, no. 3, pp. 671-688, MAY/JUN 2011.

[48] B. Ben Bakir, A. Descos, N. Olivier, D. Bordel, P. Grosse, J. Gentner, F. Lelarge and J. Fedeli, "Hybrid Si/III-V lasers with adiabatic coupling," in *IEEE Group IV Photonics* , London, UK, 2011.

[49] G. Roelkens, J. Van Campenhout, J. Brouckaert, D. Van Thourhout, R. Baets, P. Rojo Romeo, P. Regreny, A. Kazmierczak, C. Seassal, X. Letartre, G. Hollinger, J. Fedeli, L. Di Cioccio and C. Lagahe-Blanchard, "III-V/Si photonics by die-to-wafer bonding," *Materials Today,* vol. 10, no. 7-8, pp. 36-43, JUL-AUG 2007.

[50] X. Luo, L. Cao, J. Song, X. Hu, Y. Cheng, C. Li, C. Liu, T.-Y. Liow, M. Yu, H. Wang, Q. J. Wang and P. G.-Q. Lo, "High-throughput multiple dies-to-wafer bonding technology and III/V-on-Si hybrid lasers for heterogeneous integration of optoelectronic integrated circuits," *Frontiers in Materials,* vol. 2, pp. 28/1-28/21, APR 2015.

[51] K. Debnath, K. Welna, M. Ferrera, K. Deasy, D. G. Lidzey and L. O'Faolain, "Highly efficient optical filter based on vertically coupled photonic crystal cavity and bus waveguide," *Optics Letters,* vol. 38, no. 2, pp. 154-156, 2013.

Chapter 7

Conclusion

In this thesis, I have introduced and explored the potential of an electrically-pumped hybrid III-V External Cavity (EC) laser design, suitable for Silicon Photonic applications (with a primary focus on energy-efficient Silicon Photonic WDM data-communication systems). The examined laser architecture comprises a III-V Reflective Semiconductor Optical Amplifier (RSOA) and an external Silicon wavelength-selective reflector, based on a Photonic Crystal (PhC) cavity vertically coupled to a low-refractive-index bus waveguide [1].

The EC approach ensures high yield and performance (as it enables the independent design, fabrication, testing and optimization of the III-V and the Silicon chips), as well as good heat dissipation through the spatial separation of the passive and the active parts that it offers. Even though EC devices using Bragg gratings [2, 3, 4], ring resonators [5, 6], and Sagnac interferometers [7] as Silicon reflectors have previously been demonstrated, the use of a PhC cavity-based mirror is particularly relevant: providing the ultimate spatial and temporal light confinement [8], PhC cavities can combine very small footprint with large Free Spectral Range (FSR), and hence are ideal for WDM interconnects that require high integration density and tight frequency channel spacing. The vertically coupled PhC cavity-bus waveguide system, apart from facilitating the coupling of light to/from Silicon PhC cavities, was selected for further technological reasons. More specifically, the low refractive index of the bus waveguide allows for larger waveguide cross-sections, as well as for lower reflectivity at the interface with air, in comparison to the case of Silicon waveguides. As a result, adequately low direct butt-coupling losses can be observed (<3 dB/facet) to both III-V RSOA waveguides and optical fibers, eliminating the need for use of spot-size converters (SSC) or other equivalent structures on the Silicon reflector chip, and thus simplifying its fabrication process.

To examine the validity of the studied concept, a long EC laser configuration comprising a fiber pigtailed SOA with a fiber optic reflector and the above described resonant mirror was demonstrated in Chapter 4. The external reflector chip consisted of an SU8 polymer waveguide vertically coupled to a Dispersion Adapted (DA) PhC cavity [9] on the 220 nm Silicon-On-Insulator (SOI) platform. Output powers of >1.5 mW and a slope efficiency of η_s = 0.0324 mW/mA were observed for lasing in the S- and C-bands. The change of the emitted wavelength (with SMSR* >25 dB in every case) by lithographically tuning the employed PhC cavities confirmed that the lasing wavelength in the studied in this thesis design is determined by the resonances of the PhC cavity.

* Side-mode suppression ratio.

The presented working principle was extended to a compact EC laser configuration comprising a 250-μm long RSOA die on sub-mount and the aforementioned Silicon resonant reflector chip, in Chapter 5. Lasing thresholds around 12-13 mA were found for waveguide-coupled (wc) output powers up to 8.5 mW (at 80 mA) and wc wall-plug efficiencies up to ~8.5 % (at 41 mA) at emitted wavelengths around 1550 nm. Single mode laser linewidths of ~4.5 MHz were measured using a self-heterodyne technique and the observed side-mode suppression ratios (SMSR) were consistently in excess of 40 dB (reaching a maximum of 50 dB). The performance of the device was on par with the performance of analogous hybrid EC laser structures [2, 3, 4, 5, 6].

Except for the smaller size and the larger FSR that it provides, the use of a PhC cavity-based reflector is also comparatively favorable for the stabilization of the emitted wavelength – a highly desired feature in WDM optical interconnects. The optical power of the laser cavity dissipated in the PhC cavity via two-photon absorption (TPA) and free-carrier absorption (FCA) causes a nonlinear increase of the temperature of the reflector significantly above ambient, resulting in a strong dependence of the lasing wavelength on the intra-cavity power. It is understandable thus that a zero net wavelength shift can be achieved in the considered EC laser configuration without active cooling, by appropriately increasing the laser power at lower operating temperatures. Through this technique, wavelength stability with a ±0.38 nm variation around the central wavelength (1550.85 nm) was achieved over a temperature span of 60° C (between 20° and 80° C) for a laser output power decrease by a factor of 9 (while simulations suggest that an increase in the efficiency of the technique by a factor of >2.5 can be achieved by removing the Silicon substrate on the SOI reflector chip). Owing to the fact that PhC cavities exhibit the ultimate Q-factor/V ratio [8], this strategy can be applied to the considered compact EC laser at a much lower power penalty than for equivalent configurations comprising Silicon reflectors based on structures with smaller Q-factor/V ratio (e.g. ring resonators or Bragg reflectors).

Further, the suitability of the considered laser configuration for integration with silicon planar optical circuits (e.g. by butt-coupling via flip-chip bonding [10, 11, 12, 13]) was examined through a RSOA-to-SU8 waveguide alignment sensitivity study. An experimental increase of the coupling losses and of the laser threshold current of < 20% in the horizontal direction and of < 15% in the vertical and z[1] directions for a 500 nm misalignment from the optimal alignment position was observed (in agreement with the results obtained from simulations), indicating the possibility for integration in practical application platforms (as similar placement accuracies have been demonstrated for flip-chip bonding systems [10, 13]).

Finally, the suitability of the proposed EC laser design for direct frequency modulation was shown in Chapter 6. As the emitted wavelength is determined by the resonant wavelength of the PhC cavity on the Silicon reflector, modulation of the laser output can be realized by modulating the PhC cavity resonances. Similar approaches have been very recently demonstrated by Fujitsu [14] and Hewlett Packard [15], utilizing ring resonators as tunable elements in the laser cavity. This method is of particular interest in WDM optical interconnects, as it enables the employment of low-power-consumption resonant modulators in practical applications by

[1] The z-direction is defined along the axis of propagation of light in the considered waveguides.

eliminating the need to match the emitted wavelength of a laser source to their resonances. For the experimental proof of the concept, the DA PhC cavity on the resonant reflector of the above described compact EC laser configuration was embedded in a p^+pnn^+ junction that extended into its defect [16]. Tuning of the resonant wavelength was obtained through the carrier dispersion effect, by biasing the pn junction. Direct frequency modulation of the considered EC laser at speeds up to 100 MHz (limited by the employed electrical setup and design) was achieved for injection type modulation of the pn diode, at a constant RSOA drive current of 30 mA. Even though the demonstrated modulation performance was not optimal, the proof-of-concept use of a PhC cavity as the tunable element of the examined EC laser is rather advantageous: due to their ultra-small modal volume (V), PhC cavity-based modulators can exhibit very low capacitance (e.g. 5.6×10^{-18} F [17]) and thus a potential modulation power consumption (sub-pJ/bit) of more than one order of magnitude lower than conventional ring resonators [16, 17, 18] (which are employed in the works by Fujitsu and Hewlett Packard).

To sum up, I demonstrated the possibility of using a vertically coupled PhC cavity-bus waveguide system as a reflector in an EC laser architecture. Different configurations (fibre- and die-based) of such EC lasers were built and characterized. The experimentally observed performance, alignment tolerance, wavelength stability with temperature, and suitability for direct frequency modulation reveal the potential of the proposed scheme to be an appealing candidate for WDM operation in Silicon optical interconnects. The demonstration of a laser solution based on the vertically coupled platform is an addition to the active and passive components based on the same concept [16, 19, 20] towards the realization of more complex power-efficient Silicon Photonics systems.

References

[1] K. Debnath, K. Welna, M. Ferrera, K. Deasy, D. G. Lidzey and L. O'Faolain, "Highly efficient optical filter based on vertically coupled photonic crystal cavity and bus waveguide," *Optics Letters,* vol. 38, no. 2, pp. 154-156, 2013.

[2] S. Tanaka, S.-H. Jeong, S. Sekiguchi, T. Kurahashi, Y. Tanaka and K. Morito, "High-output power, single-wavelength silicon hybrid laser using precise flip-chip bonding technology," *Optics Express,* vol. 20, no. 27, pp. 28057-28069, DEC 2012.

[3] A. Zilkie, P. Seddighian, B. J. Bijlani, W. Qian, D. C. Lee, S. Fatholoumi, J. Fong, R. Shafiiha, D. Feng, B. J. Luff, X. Zheng, J. E. Cunningham, A. V. Krishnamoorthy and M. Asghari, "Power-Efficient III-V/Silicon external cavity DBR lasers," *Optics Express,* vol. 20, no. 21, pp. 23456-23462, OCT 2012.

[4] T. Creazzo, E. Marchena, S. B. Krasulick, P. K. L. Yu, D. Van Orden, J. Y. Spann, C. C. Bliving, L. He, H. Cai, J. M. Dallesasse, R. J. Stone and M. Amit, "Integrated tunable CMOS laser," *Optics Express,* vol. 21, no. 23, p. 28048, NOV 2013.

[5] T. Chu, N. Fujioka and M. Ishizaka, "Compact, lower-power-consumption wavelength tunable laser fabricated with silicon photonic-wire waveguide micro-ring resonators," *Optics Express,* vol. 17, no. 16, pp. 14063-14068, AUG 2009.

[6] S. Lin, S. S. Djordjevic, J. E. Cunningham, I. Shubin, Y. Luo, J. Yao, G. Li, H. Thacker, J.-H. Lee, K. Raj, X. Zheng and A. V. Krishnamoorthy, "Vertical-coupled high-efficiency tunable III-V-CMOS SOI hybrid external-cavity laser," *Optics Express,* vol. 21, no. 26, pp. 32425-32431, DEC 2013.

[7] Y. Zhang, S. Yang, H. Guan, A. E.-J. Lim, G.-Q. Lo, P. Magill, T. Baehr-Jones and M. Hochberg, "Sagnac loop mirror and micro-ring based laser cavity for silicon-on-insulator," *Optics Express,* vol. 22, no. 15, pp. 17872-17879, JUL 2014.

[8] M. Notomi, K. Nozaki, A. Shinya, M. Shinji and K. Eiichi, "Toward fJ/bit optical communication in a chip," *Optics Communications,* vol. 314, pp. 3-17, MAR 2014.

[9] K. Welna, S. L. Portalupi, M. Galli, L. O'Faolain and T. F. Krauss, "Novel Dispersion Adapted Photonic Crystal Cavity with Improved Disorder Stability," *IEEE Journal of Quantum Electronics,* vol. 48, no. 9, pp. 1177-1183, SEP 2012.

[10] S. Tanaka, S.-H. Jeong, S. Sekiguchi, T. Kurahashi, Y. Tanaka and K. Morito, "HIgh-output power, single-wavelength silicon hybrid laser using precise flip-chip bonding technology," *Optics Express,* vol. 20, no. 27, pp. 28057-28069, DEC 2012.

[11] N. Fujioka, T. Chu and M. Ishizaka, "Compact and low power consumption hybrid integrated wavelength tunable laser module using silicon waveguide resonators," *Journal of Lightwave Technology,* vol. 28, no. 21, pp. 3115-3120, SEP 2010.

[12] T. Shimizu, N. Hatori, M. Okano, M. Ishizaka, Y. Urino, T. Yamamoto, M. Mori, T. Nakamura and Y. Arakawa, "High density hybrid integrated light source with a laser diode array on a silicon optical waveguide platform for inter-chip optical interconnection," in *IEEE Group IV Photonics*, London, 2011.

[13] F. E. Doany, R. A. Budd, L. Schares, T. N. Huynh, M. G. Wood, D. M. Kuchta, N. Dupuis, C. L. Schow, B. G. Lee, M. Moehrle, A. Sigmund, W. Rehbein, T. Y. Liow, L. W. Luo and G. Q. Lo, "A Four-Channel Silicon Photonic Carrier with Flip-Chip Integrated Semiconductor Optical Amplifier (SOA) Array Providing >10-dB Gain," in *IEEE 66th Electronic Components and Technology Conference* , Las Vegas, Nevada, USA, 2016.

[14] T. Akiyama, S. Tanaka, T. Kurahashi, H. Ebe and S. Sekiguchi, "A novel transmitter leveraging high-speed ultralow-power modulation of a Si microring modulator by eliminating tuning power," in *Optical Fiber Communications Conference and Exhibition (OFC), 2016*, Anaheim, CA, MAR 2016.

[15] D. Liang, X. Huang, G. Kurczveil, M. Fiorentino and R. G. Beausoleil, "Integrated finely tunable microring laser on silicon," *Nature Photonics,* vol. 10, pp. 719-722, SEP 2016.

[16] K. Debnath, L. O'Faolain, F. Y. Gardes, A. Steffan, G. T. Reed and T. F. Krauss, "Cascaded modulator architecture for WDM applications," *Optics Express,* vol. 20, no. 25, pp. 27420-27428, DEC 2012.

[17] T. Tanabe, K. Nishiguchi, E. Kuramochi and M. Notomi, "Low power and fast electro-optic silicon modulator with lateral pin embedded photonic crystal nanocavity," *Optics Express,* vol. 17, no. 25, pp. 22505-22513, DEC 2009.

[18] K. Nozaki, T. Tanabe, A. Shinya, S. Matsuo, T. Sato, H. Taniyama and M. Notomi, "Sub-femtojoule all-optical switching using a photonic-crystal nanocavity," *Nature Photonics,* vol. 4, pp. 477-483, MAY 2010.

[19] K. Debnath, F. Y. Gardes, A. P. Knights, G. T. Reed, T. F. Krauss and L. O'Faolain, "Dielectric waveguide vertically coupled to all-silicon photodiodes operating at telecommunication wavelengths," *Applied Physics Letters,* vol. 102, p. 171106, APR 2013.

[20] K. Debnath, R. Moore, A. Liles and L. O'Faolain, "Toolkit for photonic integrated circuits based on inverted rib waveguides," *Journal of Lightwave Technology,* vol. 33, no. 19, pp. 4145-4150, AUG 2015.

Appendix A

Ion Implantation Process Flow and Implantation Doses (for the process followed in Tyndall National Institute)

The following process flow was followed for the Photonic Crystal (PhC) device wafers in phase 2. Included are the steps to define the 'inter-digitated implant', patterned by e-beam lithography.

Unless stated otherwise, all photolithography steps used Fujifilm HiPR6512 resist / OPD5262 developer for patterning. The wafers got a dehydration-bake @ 180°C for 40 minutes prior to resist spin-coating and nominal resist thickness after development was approx. 1.1 μm. The reticule-layers were exposed on the Ultratech UTS1500 stepper and the e-beam layers were exposed on the JEOL JBX-6000FS patterning-system.

MODULE	NOTES	Mask Details
Start-Material	SOI : device-layer = 220 nm / P-Type (10 Ω.cm) Buried-Oxide = 2 μm	
Clean	CMOS pre-oxidation Clean (HZPLUSFZ) : Hot DI / Ozone / NH_4OH / HF	
Zero-Level – Part One	Dehydration-Bake followed by ZEP resist coating (thickness = 750 nm)	
Zero-Level – Part One	JEOL e-beam patterning (high-current)	E-Beam : Zero-Level
Zero-Level – Part One	Development in ZED-N50 developer followed by IPA rinse	
Zero-Level – Part One	Dry-Etch (Cl_2 / HBr / O_2 plasma) on Trikon M0RI etcher	
Zero-Level – Part One	Resist-Strip : Ash (O_2 plasma) followed by H_2SO_4 / H_2O_2 wet-strip	
Zero-Level – Part Two	Photolithography (Dehydration Bake / Resist spin-coating / Mask Exposure / Development)	Mask # 1 : NAP449 align-clear
Zero-Level – Part Two	Dry-Etch (C_4F_8 / CH_2F_2 plasma) on Trikon M0RI etcher	
Zero-Level – Part Two	Dry-Etch (SF_6 / C_4F_8 plasma) on STS-ASE etcher	

Zero-Level – Part Two	Wet-Etch in [5:1] BOE (also removes oxide from back-side)	
Zero-Level – Part Two	Resist-Strip : Ash (O_2 plasma) followed by H_2SO_4 / H_2O_2 wet-strip	
Clean	CMOS pre-deposition Clean (SPMCLEAN) : Hot DI / Ozone	
Initial-Oxide	PECVD deposition : 50 nm SilOx	
PPLUS implant	Photolithography (Dehydration Bake / Resist spin-coating / Stepper Exposure / Development)	Reticle # 1 : P-PLUS
PPLUS implant	Boron Implant ($6e^{14}$ @ 30 keV) on Eaton NV6200 implanter	
PPLUS implant	Resist-Strip : Ash (O_2 plasma) followed by H_2SO_4 / H_2O_2 wet-strip	
NPLUS implant	Photolithography (Dehydration Bake / Resist spin-coating / Stepper Exposure / Development)	Reticle # 2 : N-PLUS
NPLUS implant	Phos Implant ($3e^{14}$ @ 80 keV) on Eaton NV6200 implanter	
NPLUS implant	Resist-Strip : Ash (O_2 plasma) followed by H_2SO_4 / H_2O_2 wet-strip	
RTA-1	60 seconds @ 1000°C in N_2 ambient	
P-DOPING implant	Photolithography (Dehydration Bake / Resist spin-coating / Stepper Exposure / Development)	Reticle # 3 : P-DOPING
P-DOPING implant	Boron Implant ($6e^{12}$ @ 30 keV) on Eaton NV6200 implanter	
P-DOPING implant	Resist-Strip : Ash (O_2 plasma) followed by H_2SO_4 / H_2O_2 wet-strip	
N-DOPING implant	Photolithography (Dehydration Bake / Resist spin-coating / Stepper Exposure / Development)	Reticle # 4 : N-DOPING
N-DOPING implant	Phos Implant ($1e^{13}$ @ 80 keV) on Eaton NV6200 implanter	
N-DOPING implant	Resist-Strip : Ash (O_2 plasma) followed by H_2SO_4 / H_2O_2 wet-strip	

N-DOPING implant	Dehydration-Bake followed by ZEP resist coating (thickness = 750 nm)	
N-DOPING implant	JEOL e-beam patterning (high-current)	E-Beam : N-Doping
N-DOPING implant	Development in ZED-N50 developer followed by IPA rinse	
N-DOPING implant	Phos Implant ($1e^{13}$ @ 80 keV) on Eaton NV6200 implanter	
N-DOPING implant	Resist-Strip : Ash (O_2 plasma) followed by H_2SO_4 / H_2O_2 wet-strip	
RTA-2	15 seconds @ 1050°C in N_2 ambient	
Remove Initial-Oxide	Wet-Etch in [5:1] BOE	
PhC pattern	Dehydration-Bake followed by ZEP resist coating (thickness = 100 nm)	
PhC pattern	JEOL e-beam patterning (low-current)	E-Beam : PhC
PhC pattern	Development in ZED-N50 developer followed by IPA rinse	
PhC pattern	Dry-Etch (SF_6 / C_4F_8 plasma) on STS-ASE etcher	
PhC pattern	Resist-Strip : Ash (O_2 plasma) followed by H_2SO_4 / H_2O_2 wet-strip	
Clean	CMOS pre-deposition Clean (SPMCLEAN) : Hot DI / Ozone	
SOG	Spin-Coat Accuglass-211 and hot-plate bake	
SOG	Furnace-Cure @ 400°C in N_2 ambient	
Waveguide	PECVD deposition : 1 μm oxynitride	
Waveguide	Photolithography (Dehydration Bake / Resist spin-coating / Stepper Exposure / Development)	Reticle # 5 : WAVEGUIDE
Waveguide	Dry-Etch (C_4F_8 / CH_2F_2 plasma) on Trikon M0RI etcher	

Waveguide	Resist-Strip : Ash (O_2 plasma) followed by H_2SO_4 / H_2O_2 wet-strip	
Clean	CMOS pre-deposition Clean (SPMCLEAN) : Hot DI / Ozone	
Contact-Oxide	PECVD deposition : 1 μm SilOx	
Contact-Oxide	Photolithography (Dehydration Bake / Resist spin-coating / Stepper Exposure / Development)	Reticle # 6 : CONTACTS
Contact-Oxide	Dry-Etch (CF_4 / CHF_3 plasma) on Trikon M0RI etcher	
Contact-Oxide	Resist-Strip : Ash (O_2 plasma) followed by H_2SO_4 / H_2O_2 wet-strip	
Clean	[10:1] HF pre-metal Clean	
Metal	Sputter-Deposition : 500 nm Al-Si[1%]	
Metal	Photolithography (Dehydration Bake / Resist spin-coating / Stepper Exposure / Development)	Reticle # 7 : METAL
Metal	Dry-Etch (Cl_2 / BCl_3 plasma) on Trikon ICP etcher	
Metal	Resist-Strip : Ash (O_2 plasma) followed by EKC wet-strip	
Alloy	30 mins @ 400°C in forming-gas ambient	

The following tables list the implant doses and annealing conditions for the wafers used during the work presented in this thesis

Wafer ID	P-PLUS (Boron)	N-PLUS (Phos)	RTA-1 (N_2 ambient)	P-DOPING (Boron)	N-DOPING (Phos)	RTA-2 (N_2 ambient)
X-6072-1	6 e14 @ 30 keV	*3 e14*@80 keV	60 s / 1000°C	6 e12 @ 30 keV	1 e13@80 keV	15 s / 1050°C
X-6072-2	6 e14 @ 30 keV	*3 e14*@80 keV	60 s / 1000°C	6 e12 @ 30 keV	1 e13@80 keV	15 s / 1050°C
X-6072-3	6 e14 @ 30 keV	3 e14@80 keV	60 s / 1000°C	N/A	N/A	N/A
X-6072-4	6 e14 @ 30 keV	3 e14@80 keV	60 s / 1000°C	N/A	N/A	N/A
X-6072-5	6 e14 @ 30 keV	3 e14@80 keV	60 s / 1000°C	N/A	N/A	N/A
X-6106-3	6 e14 @ 30 keV	*3 e14*@80 keV	60 s / 1000°C	6 e12 @ 30 keV	1 e13@80 keV	15 s / 1050°C

X-6106-2	6 e14 @ 30 keV	3 e14@80 keV	60 s / 1000°C	6 e12 @ 30 keV	2 e13@80 keV	15 s / 1050°C
X-6255-1	6 e14 @ 30 keV	3 e14@80 keV	60 s / 1000°C	1.2 e13 @ 30 keV	1 e13@80 keV	15 s / 1050°C

List of Figures

List of Tables